ENABLING TECHNOLOGIES FOR MRI GUIDED INTERVENTIONAL PROCEDURES

by

Gregory Scott Fischer

A dissertation submitted to The Johns Hopkins University in conformity with the requirements for the degree of Doctor of Philosophy.

Baltimore, Maryland

July, 2008

Abstract

This dissertation addresses topics related to developing interventional assistant devices for Magnetic Resonance Imaging (MRI). MRI can provide high-quality 3D visualization of target anatomy and surrounding tissue, but the benefits can not be readily harnessed for interventional procedures due to difficulties associated with the use of high-field (1.5T or greater) MRI. Discussed are potential solutions to the inability to use conventional mechatronics and the confined physical space in the scanner bore.

This work describes the development of two apparently dissimilar systems that represent different approaches to the same surgical problem - coupling information and action to perform percutaneous (through the skin) needle placement with MR imaging. The first system addressed takes MR images and projects them along with a surgical plan directly on the interventional site, thus providing in-situ imaging. With anatomical images and a corresponding plan visible in the appropriate pose, the clinician can use this information to perform the surgical action.

My primary research effort has focused on a robotic assistant system that overcomes the difficulties inherent to MR-guided procedures, and promises safe and reliable intra-

prostatic needle placement inside closed high-field MRI scanners. The robot is a servo pneumatically operated automatic needle guide, and effectively guides needles under real-time MR imaging. This thesis describes development of the robotic system including requirements, workspace analysis, mechanism design and optimization, and evaluation of MR compatibility. Further, a generally applicable MR-compatible robot controller is developed, the pneumatic control system is implemented and evaluated, and the system is deployed in pre-clinical trials. The dissertation concludes with future work and lessons learned from this endeavor.

Primary Advisor: Gabor Fichtinger

Dissertation Reader: Allison M. Okamura

Dissertation Reader: Russell H. Taylor

Acknowledgements

This work would not have been possible without the help and support of my family, friends, colleagues, and advisors over the past six years.

I would first like to thank my advisor, Gabor Fichtinger, who has always supported me and my endeavors from the onset of my experience at Johns Hopkins. Gabor has provided so much assistance and guidance for me academically, professionally, and personally. This work would not have been possible without his help. I am also indebted to Russell Taylor who has mentored me and served as my Master's advisor. He has been an incredible teacher and is probably the primary reason that I have entered the field of medical robotics and computer-integrated surgery. Allison Okamura has always been my co-advisor and academic advisor throughout my studies and has also provided invaluable support along the way.

The Engineering Research Center for Computer Integrated Surgical Systems and Technology (ERC CISST) has been like a family for the past six years and I will be sad to be leaving here. All of the students and faculty that constitute the Center have provided incredible support, motivation, and friendship. I would like to expressly thank the ERC

students, Ankur Kapoor, Emad Boctor, Ameet Jain, Sheng Xu, Ming Li, Ofri Sadowski, Axel Krieger, Robert Webster, Lawton Verner, Xiaofeng Liu, Gouthami Chintalapani, Andy LaMora, Anand Viswanathan, Omar Ahmad, Marcin Balicki, Carol Riley, Henry Lin, Fran Wu, and Tian Xia. I would also like to thank the all of the ERC including Russell Taylor, Gabor Fichtinger, Allison Okamura, Louis Whitcomb, Peter Kazanzides, Jerry Prince, Greg Chirikjian, Greg Hager, and Ralph Etienne-Cummings. The ERC engineering staff has been absolutely essential for making this work possible. I would like to give a special thank you to Iulian Iordachita, Csaba Csoma, and Anton Deguet. And, of course much thanks go out to the past and present staff including, Elisa Ahmanson, Luwanna Spells, Jamie Meehan, Alison Morrow, Laura Libertini, Lynda Barker, Jen Trentowksi, Bob Blakely, and Mike Bernard.

Image Overlay: Thanks to Iulian Iordachita for assistance in manufacturing the overlay device, Csaba Csoma for software development, Eva Dyer for her significant contributions to the validation environment, Daniel Schlattman for help with shielding the LCD display for MR compatibility, Christina Wamsley for assistance in data collection, and Hugh Wall for help with operating the scanner. A special thanks goes out to our clinical collaborators, S. James Zinreich, Michelle DeOliviera, John Carrino, and Cliff Weiss. This work was supported by NSF Engineering Research Center EEC-97-31478 and Siemens Corporate Research.

MRI Robot: Thanks to Iulian Iordachita for assistance in manufacturing the robotic system, Csaba Csoma for software development, Louis Whitcomb for guidance with the me-

chanical system and controller, Noby Hata, Junichi Tokuda and Philip Mewes from the Brigham and Women's Hospital for the planning software interface, Clare Tempany for clinical guidance, and Hugh Wall for help with operating the scanner. This work was supported by CDMRP PCRP Fellowship W81XWH-07-1-0171, NIH BRP RO1-CA111288-01, and NSF EEC-97-31478.

And, of course, I could never have come this far without my family. The support and motivation from my parents, Malory and Jerry, has always been an important driving force in my life. I would like to thank my wife Laurie and her family for their encouragement. I would especially like to thank Laurie for her support and understanding of the long hours and sacrifices made to complete my Ph.D.

Dedication

This thesis is dedicated to my grandparents, Rita and Albert Haas and Shirley and Robert Fischer, my parents, Malory and Jerry, and my wife, Laurie.

Contents

List of Tables

List of Figures

Chapter 1

Introduction

Image-Guided Surgery (IGS) requires the effective coupling of *Information* and *Action*. This work describes the development of two apparently very different systems that represent different approaches to the same surgical problem – percutaneous (through the skin) needle placement with Magnetic Resonance (MR) imaging. The first system addressed takes MR images and projects them along with a surgical plan directly on the interventional site, thus providing *in-situ* imaging. This is known as the **MR Image Overlay**. The clinician can use anatomical images and a corresponding plan visible in the appropriate pose to perform the surgical action. The next step in the progression is to directly couple imaging and action – in this case, an automated system that directly uses real-time medical images guides the needle to the target. The **MR Robot** provides this intuitive coupling and allows precision needle placement within the bore of traditional diagnostic Magnetic Resonance Imaging (MRI) scanners.

1.1 Background and Motivation

The fields of Image-Guided Surgery and Medical Robotics in their present form have existed for approximately two decades, but the concept of stereotaxis in surgical guidance dates back a century [1]. However, their use with Magnetic Resonance (MR) imaging is just beginning to gain traction. With recent improvements in MRI image quality and acquisition speed, it is now possible to perform interventions under real-time MR image guidance. A typical procedure requires a clinician to look at preoperative medical images, formulate a plan, mentally register the plan to the patient, and then perform the intervention – usually without any imaging updates. Methods of presenting information in a timely manner, in an appropriate location, and assisting with interventions have been active areas of research. However, MR brings unique challenges to the implementation of interventional guidance systems.

1.1.1 Background on Computer-Integrated Surgery

1.1.1.1 Image-Guided Surgery

The Horsely-Clark stereotactic frame, shown in Fig. 1.1, is recognized as the introduction of image-guided interventions (IGI). It was developed as a way to incrementally align needles for neurological interventions in 1908 [2]. The field of image-guided surgery has grown significantly in recent years. IGS systems are becoming more widely accepted by medical professionals because they allow the surgeon to have more information available

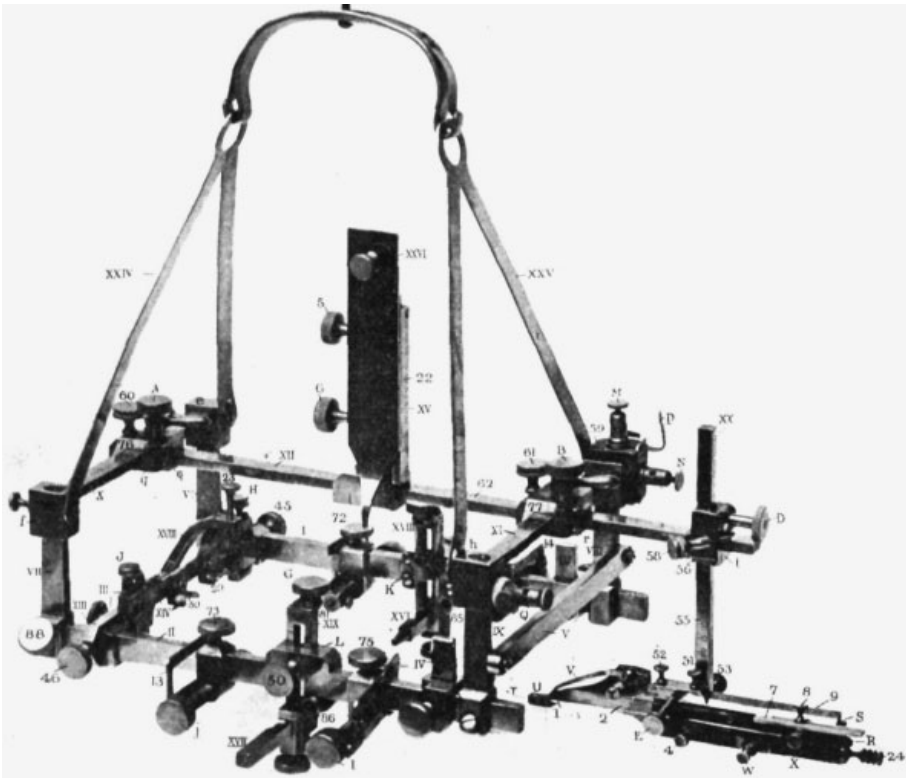

Figure 1.1: Stereotactic frame developed by Horsely and Clark in 1908 that aids in aligning needles for neurologic applications [2].

at the surgical site while performing a procedure. A thorough description of IGS systems to date is presented by Peters, *et al.* [1].

In general, these systems display 3D patient information, the surgical instrument, and a pre-operative plan. The 3D patient information can be a preoperative scan such as CT or MRI registered to the the patient during the procedure, or it can be a real-time imaging modality such as ultrasound or fluoroscopy. Such guidance is particularly crucial for minimally invasive surgery (MIS) in which the procedure is performed through small openings in the body. MIS techniques provide for reduced patient discomfort, faster healing time, decreased risk of complications, and better overall patient outcomes; however, the sensory

information available to the surgeon is greatly limited as compared with the open approach. It is especially crucial to have tracked surgical instruments that are presented in the proper position and orientation in the anatomical image on the display for the surgeon. Procedures in which such systems are particularly useful and have gained momentum are percutaneous therapy, neurosurgery, and ear, nose, and throat (ENT) surgery.

Knowing where the patient and the instrument are with respect to each other is critical; this is where tracking systems come into play. With the exception of systems that track the tools and the patient directly with real-time imaging, IGS systems are based on spatial tracking systems. Spatial tracking can typically take the form of optical tracking or electromagnetic tracking. Since the effectiveness of an IGS system is directly related to how accurately it can show the target anatomy with respect to the surgical instrument, spatial accuracy of the tracking system is paramount.

Typical IGS systems integrate: (1) imaging, (2) spatial tracking, (4) registration, and (3) visualization. Fig. 1.2 shows some examples of commercially available IGS systems. These commercially available IGS systems take pre-operative medical images and make them available during the procedure.

This work focusses on expanding upon this technology by integrating interactive real-time intra-operative imaging into the surgical navigation environment.

Figure 1.2: Examples of commercial image-guided surgery (IGS) systems: BrainLab Kolibri™(left), Medtronic StealthStation®(center), and GE InstaTrak®(right).

1.1.1.2 Medical Robotics

Computer Integrated Surgery (CIS) requires integration of two elements, *information* and *action*. The IGS systems described earlier provide information to the surgeon in a timely manner as the procedure is being performed. The next level of integration is to couple robotic action with that information to physically assist with the procedure at hand. The field of medical robotics was born in the late 1980's, with the first reported system by Kelly, *et al.* in 1986 [3], and shortly after by Benabid, *et al.* in 1987 [4] and Kwoh, *et al.* in 1988 [5], all for robotic neurosurgery.

Early medical robotic systems include the the RoboDoc for hip replacement by Taylor, *et al.* [6, 7], the Probot for prostate resection by Davies, *et al.* [8, 9], and the LARS robotic assistant for laparoscopic surgery by Taylor, *et al.* [10] and later adapted to x-ray fluoroscopy guided interventions [11].

Fig. 1.3 shows a cross-section of surgical robot types. The RoboDoc system in Fig.

1.3 (a) is a cooperatively controlled robot, as is the the JHU Steady Hand system [12]. In these cooperatively controlled robots, the surgeon grasps a handle attached to the robot through a six degree-of-freedom (DOF) force/torque sensor and the robot moves with an admittance control law in which the robot velocity is proportional to the applied force. The commercially available daVinci system (Intuitive Surgical, Inc., Sunnyvale, CA) is shown in Fig. 1.3 (b). In this tele-operated system, the surgeon sits at a remote site (across the room or potentially across the world) and controls the manipulator. The third type of robot shown represents the class of "point-and-click" needle placement robots. Fig. 1.3 (c) shows the remote center of motion (RCM) robot developed by Stoianovici, *et al.* adapted for stereotactic computed tomography (CT) guided needle placement [13].

The extensive recent development of robotics in medicine can be found in survey papers including Taylor, *et al.* [14], Cleary, *et al.* [15], Davies [16], Howe, *et al.* [17], and Dario, *et al.* [18].

Figure 1.3: Examples of surgical robots: cooperatively controlled Integrated Surgical Systems ROBODOC®(top), tele-operatively controlled Intuitive Surgical daVinci®(center), and CT image-guided RCM needle guide [13] (bottom).

1.1.2 Interventional MRI

Magnetic resonance imaging is an excellent imaging modality for the detection and characterization of many human diseases. Its outstanding soft tissue contrast allows for accurate delineation of the pathologic and surrounding normal structures. Thus MRI has an unmatched potential for guiding, monitoring and controlling therapy [19, 20]. In needle biopsies, the high sensitivity of MRI in detecting lesions allows excellent visualization of the pathology, and the high tissue contrast helps to avoid critical structures in the puncture route [19, 21]. Advances in magnet design and magnetic resonance (MR) system technology coupled with the development of fast pulse sequences have contributed to the increasing interest in interventional MRI.

There are a number of technical aspects and concerns to consider when putting an interventional magnet into operation. The most pertinent ones are: configuration and field strength of the magnet (which necessitates a compromise between access to the patient and signal-to-noise), safety and compatibility of the devices and instruments that will be used in or near the magnetic field, spatial accuracy of imaging for localization and targeting, optimal use of the imaging hardware and software (the dynamic range of gradients, limitation and availability of pulse sequences, radiofrequency coils) and level of integration with guidance methods for accomplishing the procedure.

There are three main magnet bore configurations that are currently used for interventional MR. The first type, "clam shell" configuration, has a horizontally opened gap and is basically an adaptation and slight modification to the routine open low field MR unit. The

Figure 1.4: Open MRI scanner configurations: “clam shell” configuration (top-left), “cylinder” configuration (top-right), and “double donut” configuration (bottom).

Philips Panorama 1.0T is shown in Fig. 1.4(a). The second type, “cylinder” configuration, is an adaptation of a high field (1.5T or 3.0T) MR unit. Some scanners of this type are made with a flared opening or wider bore to allow an operator to reach in but, in general does not allow for direct patient access for a majority of procedures without robotic or other mechanical assistance. Therefore imaging and intervention are “decoupled”. That is, manipulation of devices or surgical work is done outside the bore and then the patient must be moved into the magnet for imaging. The Siemens Magnetom Verio 3T shown in Fig.

1.4(b) has a $70cm$ diameter, $173cm$ long bore. The third type of configuration is a mid-field magnet specifically designed for intervention, which has two cylinders separated by a gap for access, referred to as the "double donut". The GE Signa SP 0.5T system is shown in Fig. 1.4(c), but is no longer offered as a commercial product.

A wide variety of procedures may be performed on open magnets but the trend is to use high-field closed magnets [22], mainly because of improved imaging quality and wider availability of pulse sequences. Although shorter bore high-field magnets are becoming more common, this does still not translate into easy access for surgery and intervention without assistance devices (*i.e.* robotics).

A thorough review review of interventional MR guidance techniques and trends is presented by Moche, *et al.* [23] and by Nour, *et al.* [24]. The higher the field, the higher the signal to noise ratio (SNR); the higher SNR can be used to improve spatial and temporal resolution and can make techniques like temperature or flow sensitive imaging, functional brain MRI, diffusion imaging or MR spectroscopy more useful. Considering these trends, it appears that the use of conventional high-field closed MRI scanners for guidance will allow more successful dissemination of MR-guided techniques.

1.1.3 Augmented Reality Surgical Assistant Techniques

Numerous surgical navigation systems (SNS) have been developed to aid the operator by tracking the surgical tool with respect to the patient and imaging device by dynamically referencing some fiducials (skin markers, bone screws, head-frame, etc.) attached to the

patient's body. Although SNS have been commercially available for over a decade, they were not applied in the scanner room except in a handful of limited trials with low-field open MRI [25, 26, 27, 28]. While the application of SNS on high-field closed MRI might seem obvious, this has not yet been achieved due to the inherent limitations of tracked SNS. In theory, the most appealing aspect of tracked SNS is multi-planar image guidance – when a needle trajectory is shown in three orthogonal images reformatted in real-time as the needle moves. This feature is excellent, as long as the reformatted images are of good quality, *i.e.* the image volume is large along all three dimensions and the voxel resolution is uniformly high. SNS also works well on open magnets [25] where the acquisition of MR slices follow the tool in real-time. This, however, is not the case with closed bore magnets where patients are moved in and out of the bore for needle manipulation. In these procedures, in the interest of time, we acquire only a few thin slices (often only a single image) instead of a thick and dense slab of data. This limitation has a decisive negative impact on the performance of SNS, because real-time image reformation is now impossible outside the principal plane of imaging (which is typically the transverse/axial plane). Therefore, the surgical tool (needle) is constrained to a thin image slab or single image; this deprives the SNS of its most beneficial feature. Further problems include optical trackers that require unobstructed line of sight, potentially resulting in a spatial arrangement disruptive to operating room traffic; and electromagnetic trackers are incompatible with the MRI room altogether. In short, tracked SNS are not well suited for assisting interventions in closed bore high-field MRI scanners.

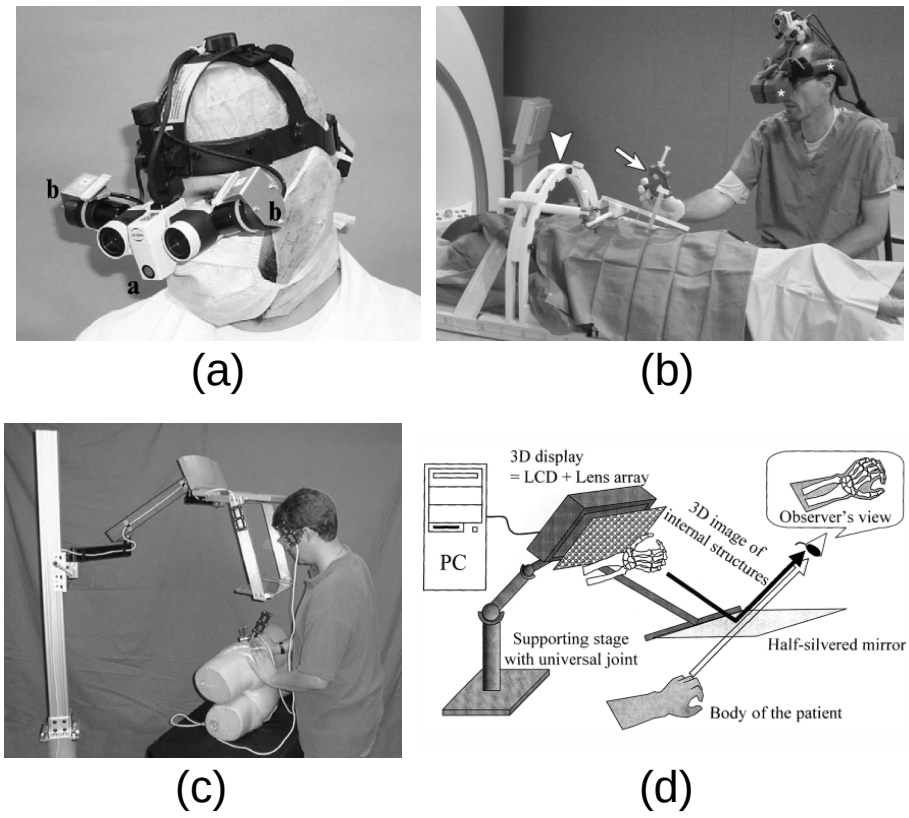

Figure 1.5: Augmented reality surgical navigation systems: Birkfellner, *et al.* [29] in (a), Sauer, *et al.* [30] in (b), DiGioia, *et al.* [31] in (c), and Iseki, *et al.* [32] in (d).

In an attempt to fuse imaging information with the operative field, several augmented reality and optical guidance techniques have been investigated. Birkfellner, *et al.* integrated computer graphics into the optical path of a head-mounted stereo binocular [29] (Fig. 1.5(a)). Sauer, *et al.* reported another variant of head-mounted display (HMD) technology [33, 30], in which two head-mounted cameras captured the real scene and a stereo HMD visualized the augmented scene (Fig. 1.5(b)). DiGioia, *et al.* developed a volumetric image overlay system by projecting 3D virtual image on a semitransparent mirror in which the physician simultaneously can observe the actual patient and computer- generated im-

ages [31] (Fig. 1.5(c)). A similar device using this concept is commercially available under the brand name of Dextroscope [34], which also involves elaborate preoperative calibration and requires real-time spatial tracking of all components, including the patient, physicians head, overlay display, mirror, and surgical tools. Grimson, *et al.* graphically overlaid segmented 3D preoperative images onto video images of the patient [35]. This approach presented largely the same calibration and tracking problems as DiGioia's system, and in addition, the projected image also had to be warped to conform to the surface of the patient. Iseki, *et al.* created a volumetric overlay display, and off-line registered to the patient in intracranial neurosurgery cases with the use of fiducials implanted into the skull [36, 32] (Fig. 1.5(d)).

There is little reported work on *in-situ* imaging under MRI. Of these systems, the HMD reported by Sauer, *et al.* in [30] has been demonstrated in preliminary studies for use in MRI. As with all of the other described systems, current volumetric augmented reality devices require painstaking calibration and real-time spatial tracking with the limitations described above, and most current systems depend on complex and expensive hardware.

1.1.4 MRI-Compatible Interventional Systems

Thorough reviews of MRI-compatible systems to date for image-guided interventions are presented by Tsekos, *et al.* [37] and by Elhawary, *et al.* [38]. Robotic assistance has been investigated for guiding instrument placement in MRI, beginning with neurosurgery [39] and later percutaneous interventions [40]. Chinzei, *et al.* developed a general-purpose

robotic assistant for open MRI [41,42]. Krieger, *et al.* presented a 3-DOF passive, manually actuated mechanical linkage to aim a needle guide [43]. Tsekos, *et al.* present a prototype robot for MR guided abdominal and thoracic interventions [44]. A high dexterity MRI-compatible system for neurosurgery, know as the neuroArm, is presented by Sutherland, *et al.* [45].

Developments in MRI-compatible motor technologies include Stoianovici, *et al.* who describe an MRI-compatible pneumatic stepper motor called PneuStep [46] and Elhawary, *et al.* who describe an air motor for limb localization [47]. Other recent developments in MRI-compatible mechanisms include pneumatic stepping motors on a light needle puncture robot by Taillant, *et al.* [48], the Innomotion commercial pneumatic robot for percutaneous interventions (Innomedic, Herxheim, Germany) [49], and haptic interfaces for fMRI by Gassert and Ganesh, *et al.* [50]. Development of MR-compatible force sensors have been investigated by Virtanen [51] who described interferometry based single axis sensors and by Tada and Kanade who present multi-axis fiber optic force sensors [52]. Ultrasonic Motor drive techniques that enhance MR compatibility are described by Suzuki, *et al.* [53]. The feasibility of using piezoceramic motors in MR is presented by Elhawary, *et al.* [54]. Dubowsky, *et al.* present the development of dielectric elastomer actuators (DEAs); in particular they present their use in a bistable, elastically averaging configuration in a prototype MR-compatible robot [55, 56].

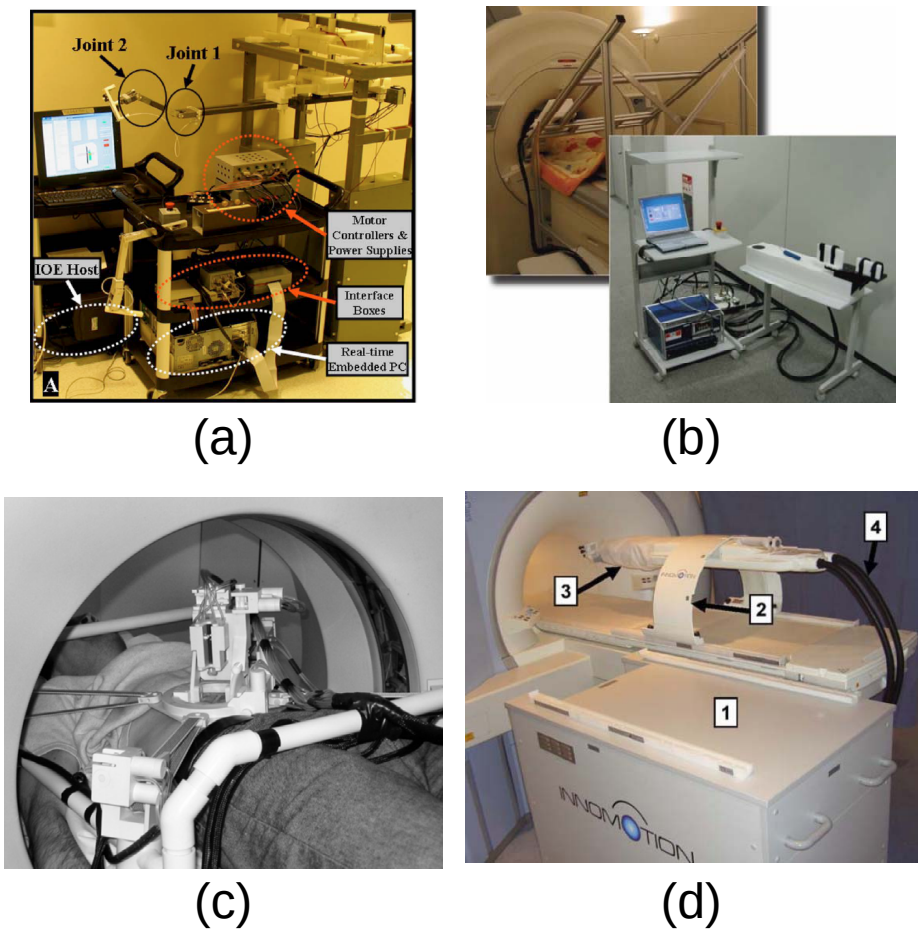

Figure 1.6: MRI-Compatible robotic systems: Tsekos, *et al.* [44] in (a), Gassert, *et al.* [50] in (b), Taillant, *et al.* [48] in (c), and Zangos, *et al.* [49] in (d).

1.1.5 Driving Clinical Applications

The techniques described in this work represent approaches generally applicable to MR-guided interventions. The following driving clinical applications demonstrated a clear and present need for surgical assistance under MR imaging and show maximal benefit from the technologies. MR Joint Arthrography, as described in Section 1.1.5.1, is logistically challenging due to the requirement for multi-modality imaging (Real-time CT/fluoroscopy

for needle insertion guidance and MR imaging for joint visualization). The Image Overlay enables needle insertion directly in MR, thus alleviating a time consuming step in the procedure. Prostate biopsy and brachytherapy, as described in Section 1.1.5.2, requires precision placement of needles in the prostate. Current techniques using ultrasound (US) guidance can not effectively monitor the seed location and traditional fluoroscopy can not effectively visualize prostate boundaries and features. MRI provides the ability to interactively monitor the needle insertion to ensure appropriate placement, and volumetric imaging to perform online dosimetry.

1.1.5.1 MRI-Guided Joint Arthrography

Adequately depicting internal derangements of joints has been a challenge for medical imaging. The state of the art uses MR arthrography (MRAr) [57, 58], in which MR contrast agent – typically a gadolinium based material – is used to visualize the joint space. MRAr may be accomplished by way of a percutaneously placed needle (referred to as direct MRAr) or with an intravenous injection of MR contrast agent (referred to as indirect MRAr). For any joint, the placement of intra-articular contrast (by direct or indirect means) can be utilized to assist the evaluation of ligaments, cartilage, synovial proliferation or loose intra-articular bodies. MRAr is most commonly used in the shoulder, hip and knee. However, there are also good indications for elbow, wrist and ankle MRAr.

Direct MRAr has become a well-established method of delineating various joint structures that otherwise show poor contrast with conventional MRI. Direct MRAr is well tol-

erated and has comparable diagnostic efficacy to joint arthroscopy, the gold standard in the evaluation of joints [59, 60]. The main advantages of direct MRAr are the reliable and consistent arthrographic effect and capsular distension produced. However, direct MRAr necessitates image guidance for joint injection, traditionally with fluoroscopy or sometimes under CT guidance [61]. Thus current direct MRAr comprises two distinct procedures: an initial radiologically-guided needle injection intervention that is promptly followed by a second diagnostic MRI session before the contrast becomes resorbed. Such a tightly sequenced double-procedure makes contemporary direct MRAr more expensive, resource intensive, and difficult to schedule. To address this problem, [62] and [63] reported the use of open MRI scanner configuration where needle insertion and contrast injection were performed directly inside scanner in the same setting. Petersilge, *et al.* [26], and later Kreitner, *et al.* [28] and Fahrig, *et al.* [27] reported the use of "open C-arm scanner" which consists of a vertically open "clam shell" MRI and optically co-registered C-arm fluoroscope. This approach also eliminates the double scheduling problem by bringing fluoroscopically guided contrast injection and MR-guided joint evaluation into the same room, but at the expense of a complex and expensive engineering entourage, which is neither practical nor generalizable.

Indirect MRAr has developed as an alternative to direct MR arthrography for imaging joints in part to obviate the intra-articular needle injection. The main advantage supporting the use of indirect MRAr is no necessity for a fluoroscopy suite. Indirect MRAr, however, can require a longer patient visit because of the time delay between injection and imaging

needed to provide suitable intra-articular enhancement. Interpretative error may result from the enhancement of extra-articular structures (such as vessels, tendon sheaths, and bursae), which may be confounded for extravasated contrast material from the joint [64, 65]. Another limitation of indirect MR arthrography is a lack of controlled joint distension compared with that of direct arthrography [64, 65]. Joint distension facilitates recognition of certain conditions such as capsular trauma or soft tissue injury concealed by a collapsed capsule. Indirect MRAr is often performed when direct arthrography is inconvenient or not logistically feasible.

Thus far only limited work has been done using MR imaging as guidance for the needle and contrast placement for MRAr. A cadaver based study showed an MR-guided technique in conjunction with the LCD screen and real-time MR imaging would be a practical alternative to conventional fluoroscopic guidance [66]. A case series involving human subjects showed the feasibility of MR-guided MRAr in the shoulder using an open configuration magnet with rapid or real-time imaging [62]. However, with low field magnets that have a vertically oriented main magnetic field, the traditional radiologic approach to the shoulder must be modified to provide adequate visualization of the needle [26]. MR-guided shoulder MRAr has also been performed on conventional high field closed bore magnet requiring several passes for joint cavity puncture [67]. An extension of this paradigm is to use a robust facile economical targeting system to facilitate joint cavity puncture.

The presented approach to direct MRAr eliminates the separate radiologically guided needle insertion and contrast injection task from the procedure by performing those tasks

directly on conventional high-field closed MRI scanner using the MR image overlay technique. The hypothesis is that the image overlay technique allows for accurate, safe, and fast needle placement and contrast injection. This promises to reduce the inconvenience for the patient and logistical difficulties associated with current direct MRAr, in a manner that is practical and affordable for any facilities that own conventional MRI scanners.

1.1.5.2 MRI-Guided Prostate Interventions

Each year approximately 1.5M core needle biopsies are performed, yielding about 220,000 new prostate cancer cases [68]. If the cancer is confined to the prostate, then low-dose-rate (LDR) permanent brachytherapy is a common treatment option; a large number (50-150) of radioactive pellets/seeds are implanted into the prostate using 15-$20cm$ long 18G needles [69]. A complex seed distribution pattern must be achieved with great accuracy in order to eradicate the cancer, while minimizing radiation toxicity to adjacent healthy tissues. Over 40,000 brachytherapies are performed in the U.S. each year and the number is steadily growing [70].

Transrectal Ultrasound (TRUS) is the current "gold standard" for guiding both biopsy and brachytherapy due to its real-time nature, low cost, and apparent ease of use [71]. However, TRUS-guided biopsy has a detection rate of only $20-30\%$ [72]. Furthermore, TRUS cannot effectively monitor the implant procedure as implanted seeds cannot be seen in the image. As a result, needle deflection and seed misplacement may go unnoticed leading to errors in the dosimetry distribution. Effects and detailed models of needle displacement in

prostate brachytherapy and biopsy are reported in [73, 74]. Fig. 1.7 shows the traditional template-based TRUS-guided approach to brachytherapy seed placement.

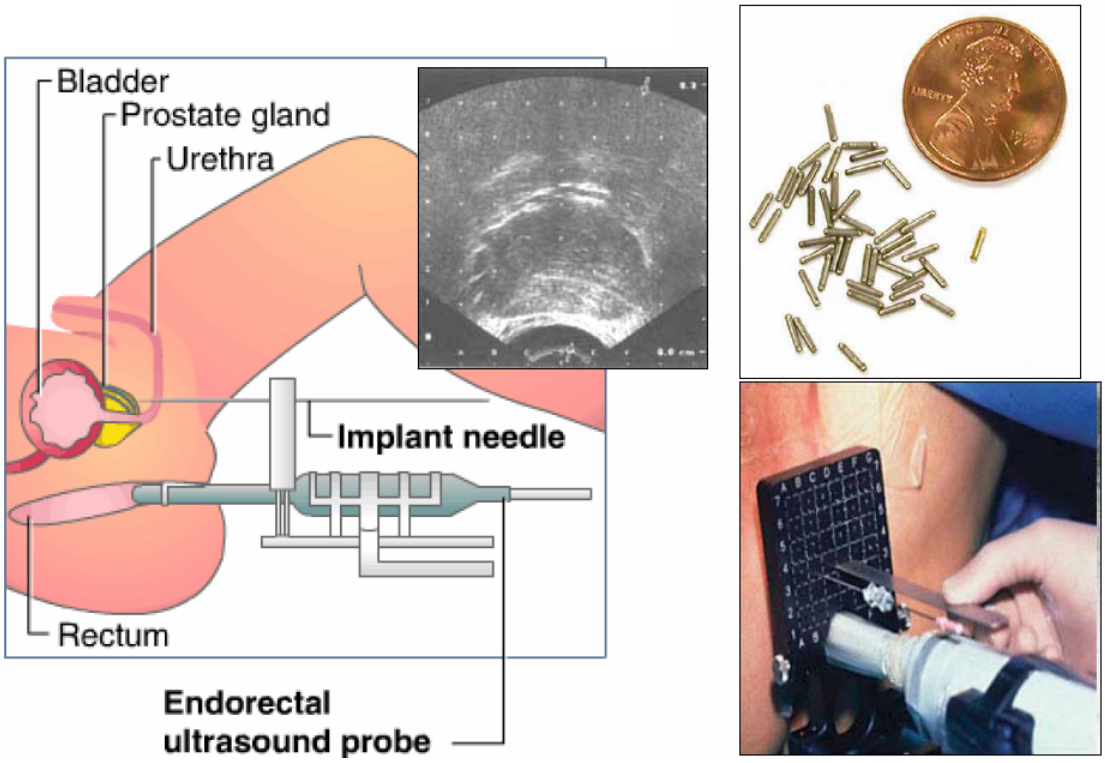

Figure 1.7: Traditional template-based TRUS-guided approach to prostate brachytherapy.

The first reported use of robotic assistance for prostate interventions was reported by Davies, *et al.* in 1989 [8]. This system, known as Probot, was developed for computer assisted transurethral prostatectomy (TURP) transurethral [9]. Other systems have since been developed for TRUS-guided brachytherapy and biopsy including: Fichtinger, *et al.* [75] shown in Fig. 1.8, Fenster, *et al.* [76], and Yu, *et al.* [77]. These systems demonstrate the efficacy of robot-assisted prostate interventions, but none are directly applicable to MRI-guided procedures.

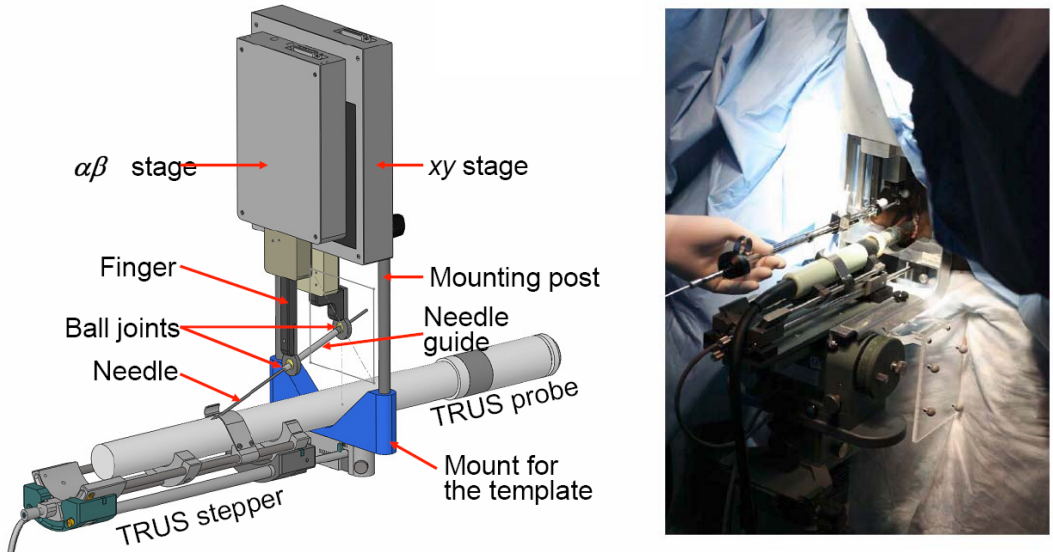

Figure 1.8: Robotic TRUS-guided approach to prostate brachytherapy [75].

MRI possesses many of the capabilities that TRUS is lacking with high sensitivity for detecting prostate tumors, high spatial resolution, excellent soft tissue contrast, and volumetric imaging capabilities. The role that MRI can play in diagnosis and treatment of prostate cancer is discussed in [78]. However, closed-bore high-field MRI has not been widely adopted for prostate interventions because strong magnetic fields and confined physical space present formidable challenges.

The clinical efficacy of MRI-guided prostate brachytherapy and biopsy was demonstrated by D'Amico *et al.* at the Brigham and Women's Hospital using a 0.5T open-MRI scanner [79]. MR images were used to plan and monitor transperineal needle placement. The needles were inserted manually using a guide comprising a grid of holes, with the patient in the lithotomy position, similarly to the TRUS-guided approach as shown in Fig.

1.9 (left). Cormack, *et al.* [80] describe real-time dosimetry during MR guided prostate brachytherapy seed placement. Similarly, Engelhard, *et al.* have evaluated MR-guided prostate biopsy in closed bore MRI using a manual alignment device developed by Invivo (Daum GmbH, Schwerin, Germany) [81]. The study showed that MR-guided prostate biopsy is effective at improving biopsy results, but was limited to lesions $\geq 10mm$.

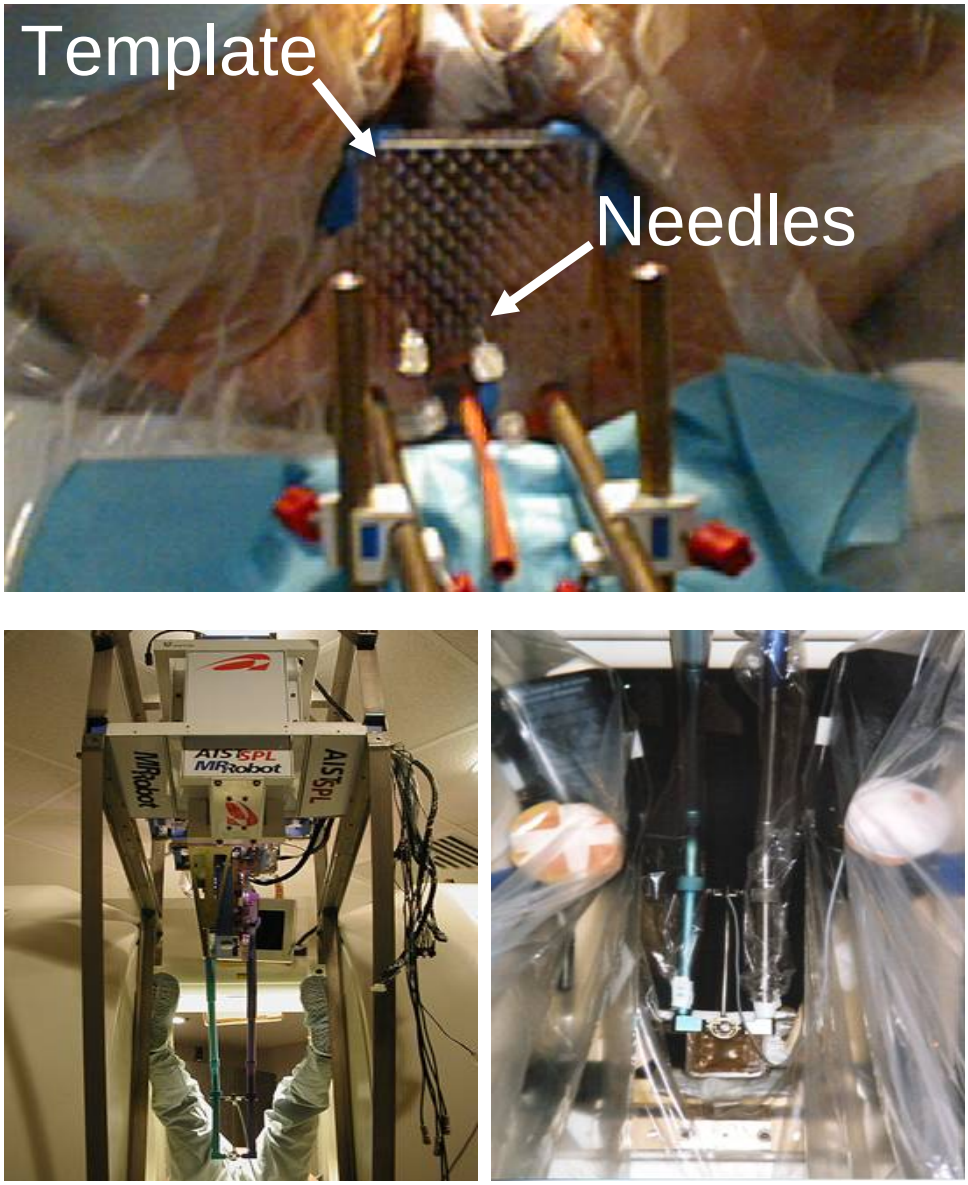

Figure 1.9: MRI-Guided approaches to prostate brachytherapy: manual with template in open scanner [79] (top) and robotic in open scanner [42](bottom).

Fig. 1.10 shows a collection of the MR-compatible assistants developed to date for prostate interventions. Chinzei, *et al.* developed a general-purpose robotic assistant for open MRI [42] that was subsequently adapted for transperineal intra-prostatic needle placement [82]. Susil, *et al.* described four cases of transperineal prostate biopsy in a closed-bore scanner, where the patient was moved out of the bore for needle insertions and then placed back into the bore to confirm satisfactory placement [83]. Krieger, *et al.* presented a 3-DOF passive, manually actuated mechanical linkage to aim a needle guide for transrectal prostate biopsy with MRI guidance [43, 84]. With the use of three active tracking coils that provide 6-DOF localization of the end effector, the device is visually servoed into position and then the patient is moved out of the scanner for needle insertion. Zangos, *et al.* [85] used a transgluteal approach with 0.2T MRI, but did not specifically target the tumor foci; they use the the Innomotion robot (Innomedic, Herxheim, Germany) to make a transgluteal approach to the prostate [49]. Beyersdorff, *et al.* [86] performed targeted transrectal biopsy in a 1.5T MRI unit with a passive articulated needle-guide and have reported 12 cases of biopsy to date. Elhawary, *et al.* [54] performed transrectal prostate biopsy. Tadakuma, *et al.* [56] used dielectric elastomer actuators (DEAs) in a prototype MR-compatible robot for transperineal needle placement in the prostate. Stoianovici, *et al.* [87] have applied their developments in MR-compatible pneumatic stepper motors and applied them to robotic brachytherapy seed placement. This system is a fully MR-compatible, fully automatic prostate brachytherapy seed placement system; the patient is in the decubitus position and seeds are placed in the prostate transperineally. The relatively high cost and complexity of

the system, in addition to the requirement to perform the procedure in a different pose than used for preoperative imaging are issues that we address through the contributions of this thesis.

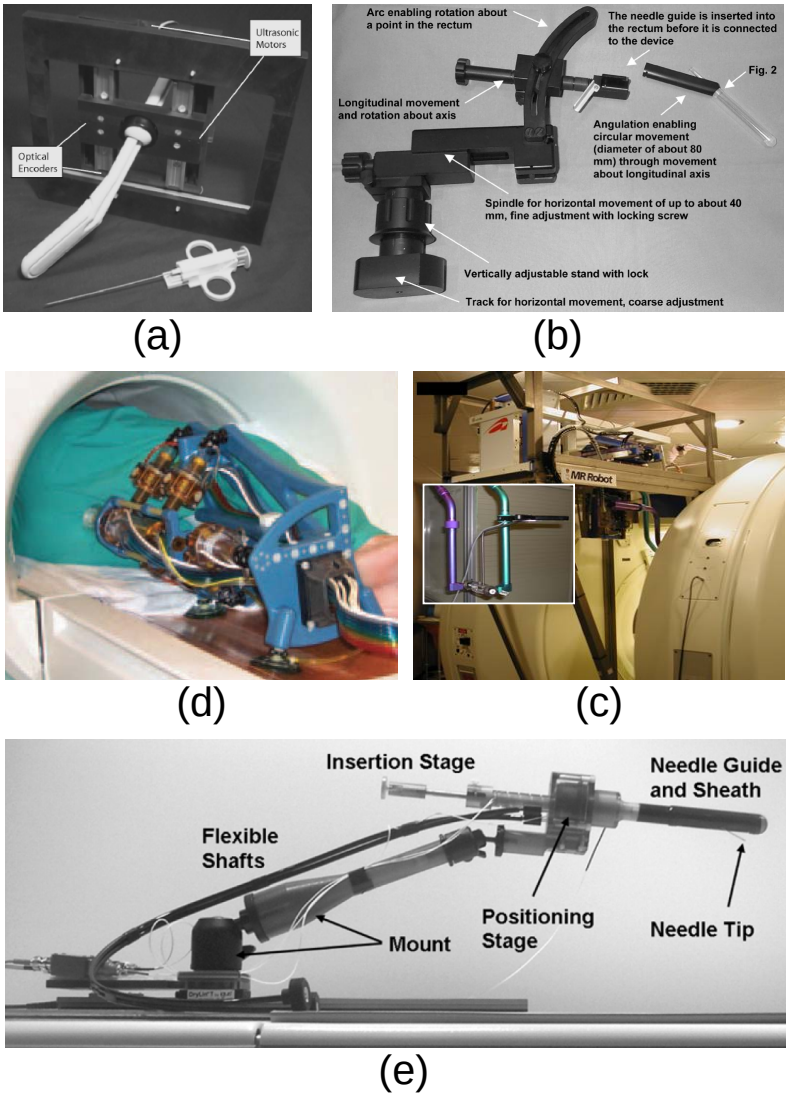

Figure 1.10: MRI guided robots and assistance device for prostate interventions: Elhawary, *et al.* [54] (a), Beyersdorff, *et al.* [86] (b), DiMaio, *et al.* [82] c), Stoianovici, *et al.* [87] (d), and Krieger, *et al.* [43] (e).

1.2 Enabling Technologies

This dissertation is focussed on developing and evaluating technologies necessary for implementing interventional systems in an MRI environment. This section provides a brief synopsis of the developments made in the field of interventional MRI.

1.2.1 MRI Visualization Technologies

The MR Image Overlay is the first reported clinally feasible system for providing *in-situ* imaging to help guide needle insertion procedures in the MRI scanner room. The development of the Image Overlay system includes:

1. Optimization of the design for optically stable image overlay.

2. Analysis of sources of error.

3. Implementation and evaluation of registration techniques.

4. Development and refinement of workflow.

5. System evaluation.

This work culminates in system accuracy evaluation and cadaver trials for joint arthrography, spine pain management, and pelvic interventions. The MRI Image Overlay system is now awaiting commencement of clinical trials. This work is presented in "MRI Image Overlay: Application to Arthrography Needle Insertion" that appeared in Journal of Computer Aided Surgery, January 2007 [88].

1.2.2 Percutaneous Therapy Technique Evaluation

When measuring needle placement accuracy directly in MRI, precise measurement is greatly limited by paramagnetic needle artifacts and lack of distinct small targets. Further, clinical equipment is prohibitively expensive and often inadequate for precise measurement. Therefore, in order to evaluate the efficacy of different needle insertion techniques and surgeon performance, a stand-alone system has been developed. The evaluation platform allows clinicians to perform needle insertions using several assisted and unassisted techniques while placement accuracy and trajectory is monitored by electromagnetically tracked needles. The work culminates in a study evaluating clinician needle insertion accuracy, learning curve, and other factors for each technique. This work is presented in "Validation System of MRI Image Overlay and Other Insertion Techniques" that appeared in Studies in Health Technology and Informatics, January 2007 [89].

1.2.3 MRI Mechatronic System

To date, there have been only a handful of attempts to develop MRI-compatible systems to assist in needle placement in closed bore scanners. Thus far, there has been no system that maintains the workflow of traditional procedures in a compact, reliable and convenient platform while enabling the use of intra-operative MRI.

The work presented here comprises the development and evaluation of an entire surgical robotic system for prostate needle insertion under MR imaging:

1. The workflow for the specific application is thoroughly evaluated and requirements defined.

2. Sensors and actuators are developed and evaluated.

3. The robotic device is designed, modeled, and analyzed.

4. The mechanism is constructed and evaluated.

5. The MR compatibility of the robot is assessed and confirmed.

The ultimate contribution is not the specific design presented, but the thorough evaluation and development of techniques for developing application-specific robotic systems for operation in MRI. The sensors, actuators, controller, and software developed and evaluated are all generally applicable to MRI-guided robotic interventions. The robotic system is presented in "MRI-Compatible Pneumatic Robot for Transperineal Prostate Needle Placement" that appeared in IEEE/ASME Transactions on Mechatronics MRI Special Issue, June 2008 [90]. MR compatibility is presented in "Robotic Assistant for Transperineal Prostate Interventions in 3T Closed MRI." that appeared in the proceedings of the International Conference of Medical Image Computing and Computer Assisted Interventions, October 2007 [91].

1.2.4 MRI Robot Controller

No commercially available systems exist for controlling a robotic system inside of an MRI scanner room. An MRI-compatible controller was designed, manufactured, and thoroughly evaluated for utility and compatibility. The primary components of this work include:

1. Construct MR-compatible controller hardware.

2. Develop low level interface software

3. Develop, model, and implement high precision sliding mode pneumatic servo controller.

4. Evaluate controller accuracy and stability

The controller developed here is not only suited for the current application, but is generally applicable to MR-guided robotic system including interventional systems, haptic devices, and precisely controlled phantoms. This work is described in "An Integrated MRI and Robot Control Software for an MRI-compatible Robot in Prostate Intervention" that appeared in the proceedings of the IEEE International Conference on Robotics and Automation, May 2008 [92].

1.2.5 MRI Robot System Architecture

This work culminated in develop of a complete system for MRI guided prostate brachytherapy. Thus far, no one has managed to develop a clinically feasible solution for transperineal needle placement in high-field diagnostic magnets with the patient in the traditional lithotomic position. This is the first fully integrated system that makes conventional diagnostic closed high-field MRI scanners available for guiding prostatic needle placement interventions.

The development of the integrated system includes:

1. Thorough analysis of the requirements.
2. Development of the mechatronic device
3. Development of the low level controller hardware and software
4. Implementation of communication and visualization software.
5. Assess and optimize the system workflow.
6. Evaluate MR compatibility, accuracy and clinical usability.

The proposed device is applicable to improving the over 1 million prostate biopsies and 40,000 brachytherapies performed in the US annually. The ability to accurately biopsy or implant seeds exactly as planned enables for the first time the ability to truly evaluate diagnosis and treatment paradigms. By enabling dexterous, high precision needle placement with online dosimetry will allow larger patient population to be treated and ultimately be

treated with better outcomes. The integrated system proposed here is directly extensible to other imaging configurations in MRI, other imaging modalities and other organ systems. This work is presented in "A System for MRI-guided Prostate Interventions" that appeared in the proceedings of IEEE International Conference on Biomedical Robotics and Biomechatronics, February 2006 [93].

1.3 Dissertation Contributions

As described previously, there has been limited development of such systems to date. To date, there have been no commercially successful robotic systems for MRI, nor are there even suitable sensors and actuators ready to use off-the-shelf. Further, there is very little common development as each research group operates independently; thus there is no common ground for comparison of systems.

This dissertation strives to take a systematic approach to development of MRI-compatible interventional systems and serve as a proof of feasibility and guide for design of such systems. As such, the major contributions of this dissertation as follows:

- We developed different methods of providing assistance to interventional procedures in the MRI scanner suite. The Image Overlay and the MRI Robot are developed and evaluated. The systems are compared and contrasted for suitability in specific applications.

- We quantitatively evaluated sensors, actuators, and display technologies for their

suitability in MRI. This serves as a common ground for comparing technologies and serves as a guide.

- We developed a robot controller specifically designed for MRI-compatible mechatronic systems. The controller software and hardware are of a modular architecture and are generally applicable to controlling and interfacing with devices in the MRI scanner.

- We developed a tool that will allow precise tissue biopsy based on real-time imaging, thus enabling new research into MR image-based prostate cancer diagnosis.

1.4 Dissertation Overview

This dissertation is composed of two main parts, corresponding to two different approaches to computer assisted MR-guided needle insertion.

The first approach, described in Chapter 2, provides *in-situ* imaging to help guide manual needle insertions. This takes the form of the MRI Image Overlay system, and projects anatomical images and guidance information in the correct position on the patient during imaging. This system is the first reported in-situ imaging device for guiding interventional procedures in the MRI scanner. The requirements for the system are discussed, the mechanical design is presented, the workflow is described, and the system is evaluated. Evaluation includes both direct phantom, animal, and cadaver experimentation, comparison with other techniques in both the MR scanner room and in laboratory trials, and development of an

independent accuracy validation system based on electromagnetic tracking.

The second approach described in Chapter 3 incorporates semi-automatic robotic action based upon real-time MR imaging to assist in needle insertions. The robotic assistant system is generally applicable to MR-guided interventions, with the target application being transperineal needle placement in the prostate for biopsy and brachytherapy seed placement. The system requirements are discussed, components are evaluated, the mechanical design and electrical system are described, the controller is presented, and the system is evaluated for MR compatibility, usability, and accuracy.

A discussion of the techniques presented in this dissertation, their applicability to MR-guided interventions, and an overview of future directions of this work are presented in Chapter 4.

Chapter 2

MRI Image Overlay

The MR Image Overlay described here is the first reported clinally feasible system for providing *in-situ* imaging to help guide needle insertion procedures in the MRI scanner room.[1] The Image Overlay overcomes the challenges of alternate means of surgical navigation in MR including MR Fluoroscopy and Head Monted Displays (HMDs). MR Fluoroscopy as described by [25] requires the use of low-field open MRI and images presented at a monitor requiring the physician to remove focus on the patient and to mentally register the images to the anatomy. HMDs, as described by Sauer, *et al.* [30] do allow for *in-situ* imaging in the scanner. However, they only provide the wearer of the display with an appropriate view, require auxiliary tracking of the patient and physician position, and require a complex engineering entourage to ensure functionality. The MR Image Overlay overcomes these problems by using a unique geometry and seamless workflow to enable

[1]This description is based primarily upon "MRI Image Overlay: Application to Arthrography Needle Insertion" that appeared in Journal of Computer Aided Surgery, January 2007 [88]. This work was performed in collaboration with Iulian Iordachita, Csaba Csoma, and Daniel Schlattman.

high precision needle placements through the use of additional information presented at the interventional site, without interfering with or slowing down the traditional procedure.

2.1 Introduction

Magnetic Resonance Imaging (MRI) provides great potential for planning, guiding, monitoring and controlling interventions. MR arthrography (MRAr) is the imaging gold standard to assess small ligament and fibrocartilage injury in joints. In contemporary practice, MRAr consists of two consecutive sessions:

1. An interventional session where a needle is driven to the joint space and MR contrast is injected under fluoroscopy or CT guidance.

2. A diagnostic MRI imaging session to visualize the distribution of contrast inside the joint space and evaluate the condition of the joint.

Our approach to MRAr is to eliminate the separate radiologically guided needle insertion and contrast injection procedure by performing those tasks on conventional high-field closed MRI scanners. We propose a 2D augmented reality image overlay device to guide needle insertion procedures. *This approach makes diagnostic high-field magnets available for interventions without a complex and expensive engineering entourage.* In preclinical trials, needle insertions have been performed in the joints of porcine and human cadavers using MR image overlay guidance; insertions successfully reached the joint space on the first attempt in all cases.

2.2 Requirements

The proposed approach uses 2D image overlay to guide the needle insertion in procedures in which real-time imaging update is not strictly necessary, so one can translate the patient out of the gantry between imaging and needle insertion. This approach can make diagnostic high-field magnets available for image-guided interventions without involving prohibitively complex and expensive engineering additions. Clinical applications highly suitable for this technique include musculoskeletal procedures such as joint arthrography, biopsy and spinal injections. MR-guided interventional procedures involving bone, soft tissue, intervertebral discs, and joints are feasible, safe and efficacious. In these applications, clinical success is directly linked to spatial accuracy. Faulty needle placement may also injure sensitive structures, thus exposing the patient to risk and pain. The ultimate effectiveness and adoption of these techniques will depend upon the availability of a simple and robust system. Perhaps the most attractive feature of the image overlay system is that the operator has optical guidance in executing the intervention without turning his/her attention away from the field of action, while performing the same actions as in conventional freehand procedures.

Limitations of conventional free-hand needle placement include the operator's ability to maintain the correct trajectory toward the target, thus causing increased number of needle passes (iterations). Typically, guidance images are displayed on the operator's 2D console, on which the operator plans the intervention. The operator mentally registers the images with the patient's anatomy and uses hand-eye coordination to execute the planned interven-

tion. Practitioners generally agree that, given enough time and opportunity for intermittent imaging and adjustments, the target usually can be reached with appropriate accuracy. The important question is, however, whether the same objective could be achieved with fewer insertion attempts, because each needle correction requires acquisition of extra images and reinsertion of the needle, thereby increasing the risk of complication, discomfort, and the length of the procedure. *Hence the prime objective of image overlay guidance is maximizing accuracy while minimizing faulty needle insertion attempts.*

The features of the the MR image overlay system that provide benefit over traditional techniques are:

1. Use planning images during intra-procedural guidance.
2. Render the physical patient, MR image, needle, and insertion plan in a single view.
3. Display optically stable images without auxiliary tracking instrumentation.
4. Require only simple intra-operative alignment.
5. Share the same view with multiple observers.
6. Maintain the traditional procedural workflow.
7. Ensure a low system cost and complexity.

2.3 Design

The system concept for the image overlay is shown in Fig. 2.1. A flat panel display is aligned with a semi-transparent mirror; this unit is mounted in the mouth of an imaging scanner that is able to produce 2D transverse (axial) slices. The patient is translated out of the bore with the encoded table to position the body under the overlay unit. The scanner, display, and mirror are co-aligned so that the reflection of a transverse image appearing in the mirror coincides with fiducials on the patient's body behind the mirror. The image appears to be floating inside the patient, as if the operator had "tomographic vision" by virtually slicing the body. A virtual needle guide is chosen along the specified trajectory, and this guide is superimposed on the overlaid anatomical image. The clinician then inserts the needle using the overlaid guide while simultaneously being able to see the anatomy and the patient. Focus never has to be taken off the patient during the procedure.

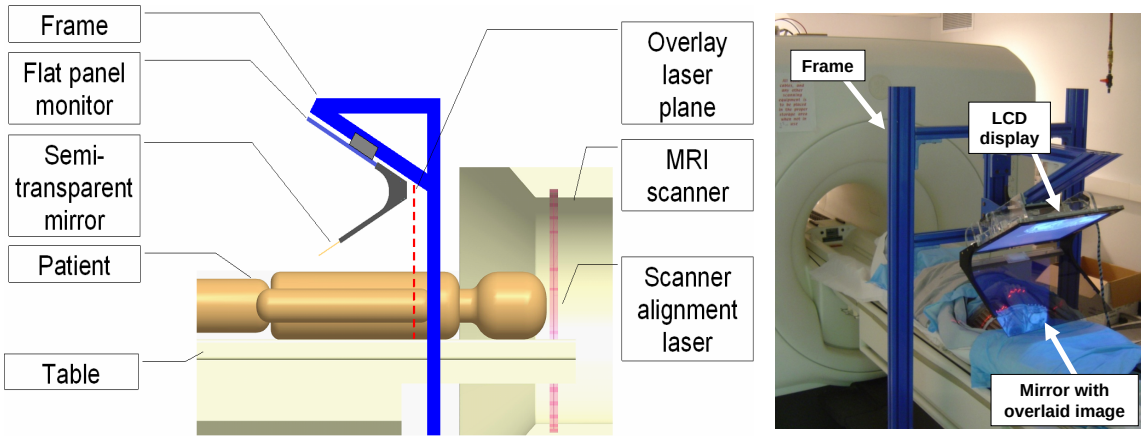

Figure 2.1: System concept of 2D image overlay device (left) and MR image overlay device in cadaver trial (right).

Further detail on development and evaluation of the MR image overlay is described

in [88]. Earlier work investigated CT-guided needle insertion with 2D image overlay, which is similar to the current MR design. A detailed description of the application and analysis of the 2D image overlay technique as applied to CT guidance is described in [94, 95] and shown in Fig. 2.2. Also, Stetten, *et al.* have shown a similar 2D overlay technique with applications to ultrasound [96].

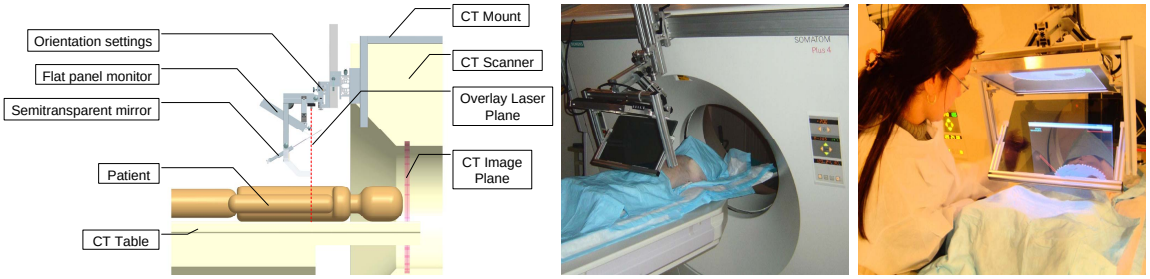

Figure 2.2: The predecessor CT image overlay device [94]. System concept (left), porcine trial configuration shown with tilted gantry (center), and view during insertion (right).

The image overlay system displays transverse MR images on an LCD display, which are reflected back to the physician from a semi-transparent mirror. Looking though this mirror, the MR image appears to be floating in the correct location in the body. The intersection of the mirror and display surface planes is marked with a transverse laser plane that is used for constraining the needle to the image plane as shown in Fig. 2.6. The MR overlay system is realized by fixing an MR-compatible LCD screen that is housed in an acrylic shell to a semi-transparent mirror at a precise angle of 60^o. The overlay unit is suspended from a modular extruded fiberglass frame as in Fig. 2.1 (right). The freestanding frame arches over the scanner table and allows for images to be displayed on a patient when the encoded couch is translated out of the bore by a known amount.

To maintain the goal of a very practical and low cost system, an off-the-shelf 19" LCD display was retrofitted to be MRI safe and electro-magnetically (EM) shielded as described in [89]. The display's steel housing and auxiliary components were removed, the electronics were arranged to optimize compatibility, power leads were added for the laser line generator, and aluminum shielding was added to enclose the monitor as shown in Fig. 2.3. The "homemade" MR display functions adequately up to $1m$ from the scanner bore on 1.5T and 3T scanners; this allows for sufficient access to the patient by translating the encoded table out as described later in Section 2.4.1.

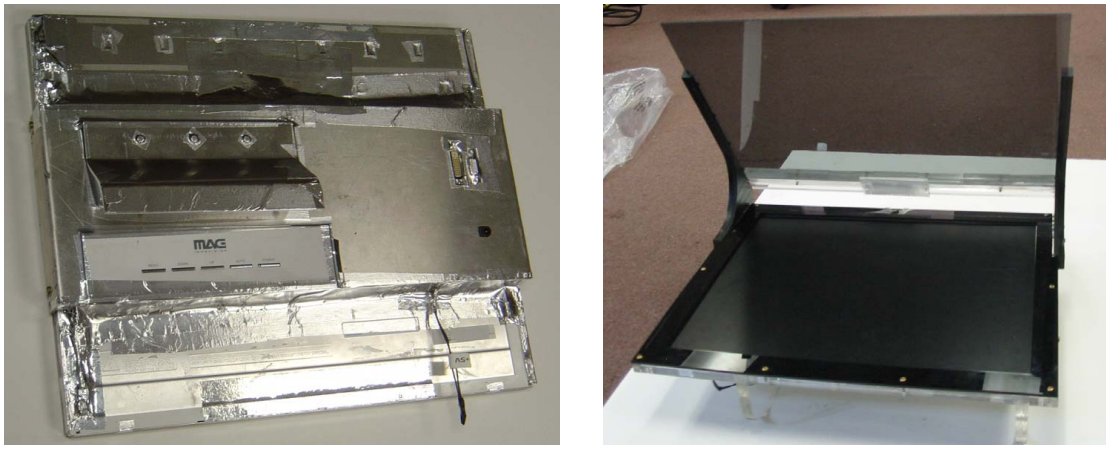

Figure 2.3: "Homemade" MRI-compatible LCD display used for MR image overlay system.

A close-up view of the overlay system during a procedure is shown in Fig. 2.4. In most needle placement procedures, after the entry point is selected with the use of skin fiducials, the operator must control three degrees-of-freedom (DOF) needle motion. In this case, the operator uses the overlay image to control the in-plane insertion angle (1st DOF), while holding the needle in the transverse plane marked by a laser light (2nd DOF). The insertion

depth (3rd DOF) may be marked with a clamp and/or zebra scale (circumferential marks) on the needle; the overlay display also provides a ruler and a depth gauge. The traditional unassisted procedure, to which operators are accustomed, is not altered; it rather increases the amount of visual information in the field of action. As the majority of needle placement procedures are executed "in-plane" (i.e. when the needle is completely contained in a single image slice), giving up full 3D rendering for engineering simplicity and low cost appears to be a most reasonable tradeoff. The overlay can also help detect target motion and allow for gating the needle insertion by the respiratory cycle. (The needle is advanced forward only when the fiducials on the patient and in the overlay image coincide at the peak of the respiratory cycle.)

2.3.1 Calibration

Calibration is accomplished in three stages:

Hardware Calibration: Align the virtual image such that it coincides with the plane of the overlay system's laser plane.

System Alignment: Align the overlay system such that it's laser plane is parallel to the scanner's transverse imaging plane.

Image Registration: Determine the in-plane transformation between the overlaid MR image and the view of the physical object in the mirror.

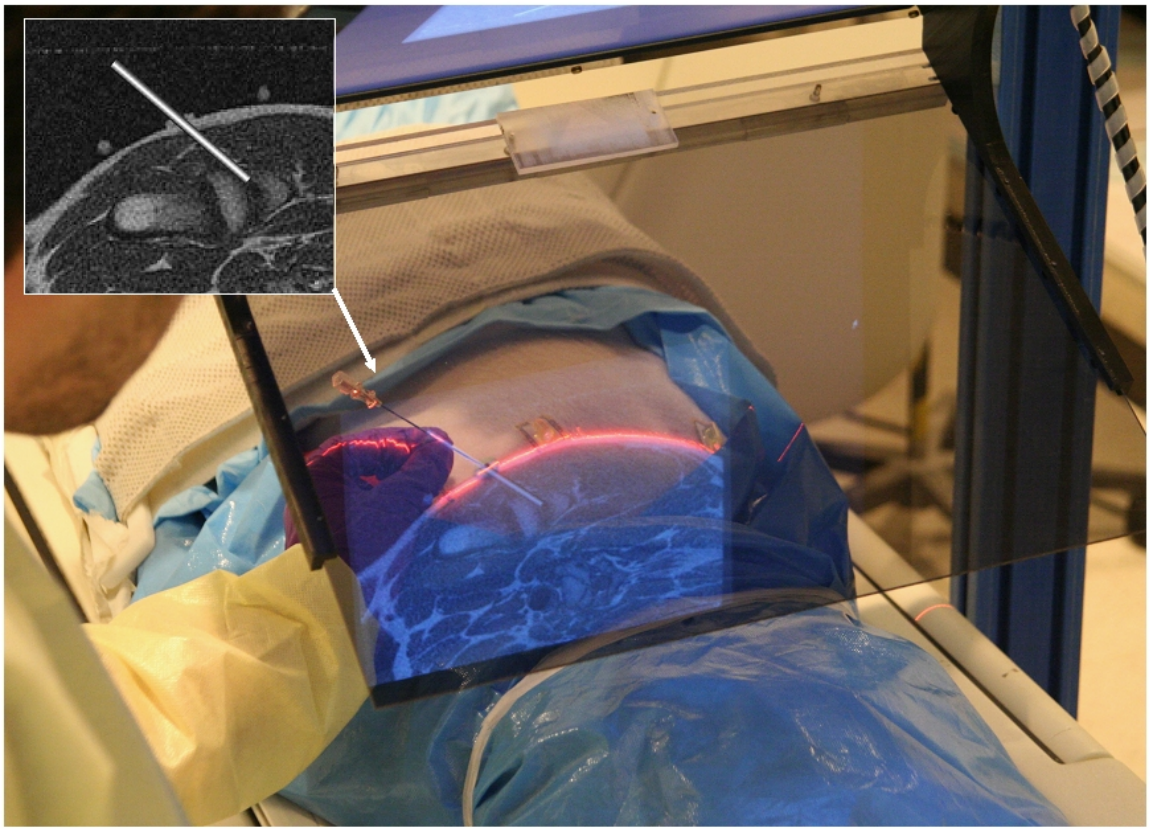

Figure 2.4: Close-up view of the MR image overlay system in a porcine trials for guiding needle insertions into the joint space of the shoulder. The plan on the targeting image is shown in the inlay.

As described in the requirements section, a primary goal is to maintain the simplicity of use. In that venture, multiple calibration and registration techniques have been evaluated. In an attempt to automate the calibration procedure, an automatic stereotactic calibration fixture was developed for the CT version of the Overlay as shown in Fig. 2.5. The calibration procedure, described fully in [94], is detailed below.

A set of Optotrak markers (Northern Digital, Waterloo, Canada) are attached to the overlay device to gain a static frame of reference denoted F_S. A set of points are rendered on the LCD screen, and F_D is determined by by touching these points with the pointer. It

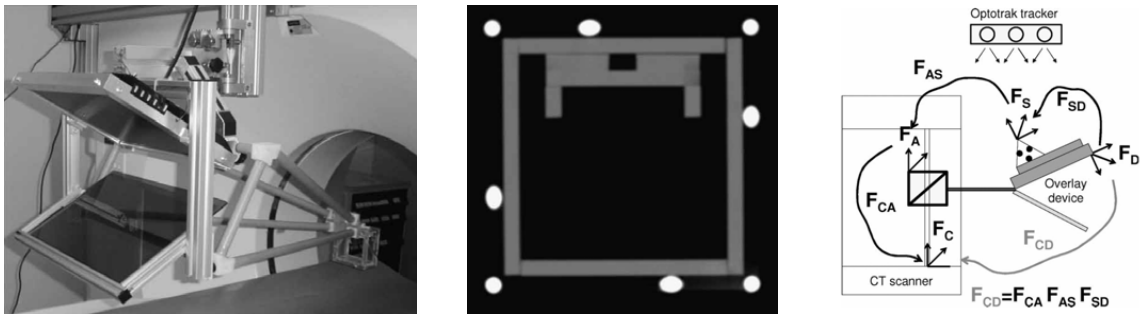

Figure 2.5: Automatic stereotactic calibration of the Image Overlay system. The CT Overlay system with the stereotactic calibration fiducial in the imaging plane (left), the corresponding CT image of the fiducial (center), and the corresponding frame transformations (right).

is then trivial to derive the frame transformation (F_{DS}), which leads from static frame (F_S) to display frame (F_D). Small dimples are precisely machined at both ends of the fiducial rods in the Optotrak pointer is pivoted. The two endpoints fully define the spatial location of a rod, and the rigid set of rods define the fiducial frame (F_A). It is trivial to derive the frame transformation (F_{SA}), which leads from adapter frame (F_A) to static frame (F_S). The reproducibility of the stereotactic adapters pose was evaluated by remounting it 17 times on the overlay device; the average error was found to be $0.16mm$ ($STD = 0.12mm$).

In the scanner room, the stereotactic fiducial frame is attached to the overlay device and a single axial slice is acquired. The rods are segmented and the 6-DOF pose of the frame F_{CA}, which leads from adapter frame (F_A) to scanner frame (F_C), is calculated using techniques similar to those described by Lee, *et al.* [20]. The concatenation of the aforementioned three frame transformations provides the frame transformation that leads from scanner coordinates system (i.e. patient coordinate system) to the display frame:

$$F_{CD} = F_{CA} \cdot F_{AS} \cdot F_{SD} \tag{2.1}$$

The transformation F_{CD} can be broken down into a series of homogeneous components, which are incorporated into either the *Image Registration* in the display software or *System Alignment* in the treatment room.

Although the preliminary results of this technique were encouraging, the increased complexity was deemed not inline with the goals of the work and a simpler calibration based on *in-situ* imaging of fiducials directly on the patient was adopted as described in the following section. However, a very similar registration technique is used for registering the phantom in the Validation System presented in Section 2.6.1.2 and for localizing the MR Robot as described in Section 3.6.2.2.

2.3.1.1 Hardware Calibration

The initial stage of calibration is concerned with adjustment of the physical overlay device hardware. This takes place when the device is initially assembled and can be repeated to ensure proper alignment as required. The task is to ensure that the angle between the laser plane and the mirror, θ_1, and the mirror and the LCD, θ_2, are the same. The laser is adjusted such that it passes though the line at the intersection of the plane at the LCD panel's surface and the plane through the top surface of the mirror, while maintaining the correct angle with respect to the mirror as shown in Fig. 2.6.

From the *Law of Reflection*, the angle of reflected light from a surface is equal to the angle of incidence upon that surface as measured from the surface normal. Thus, from the viewpoints shown in Fig. 2.6, $\alpha_i = \alpha_r$ and $\beta_i = \beta_r$. The image remains stable because the

incident light from the display reflects back to the viewer along the same path as the light from the corresponding point on the patient transmitted through the mirror. Thus, from any viewpoint, an optically stable virtual image is always visible through the mirror.

This alignment is performed during initial manufacturing, and may be confirmed and adjusted as required. In the current iteration of the system, $\theta_1 = \theta_2 = 60^o$. This angle proves to be optimal for the procedures at hand; decreasing θ limits clearance for the patient, while increasing θ limits the depth of visibility from usable viewpoints and requires unacceptably long mirrors that would impede the workflow.

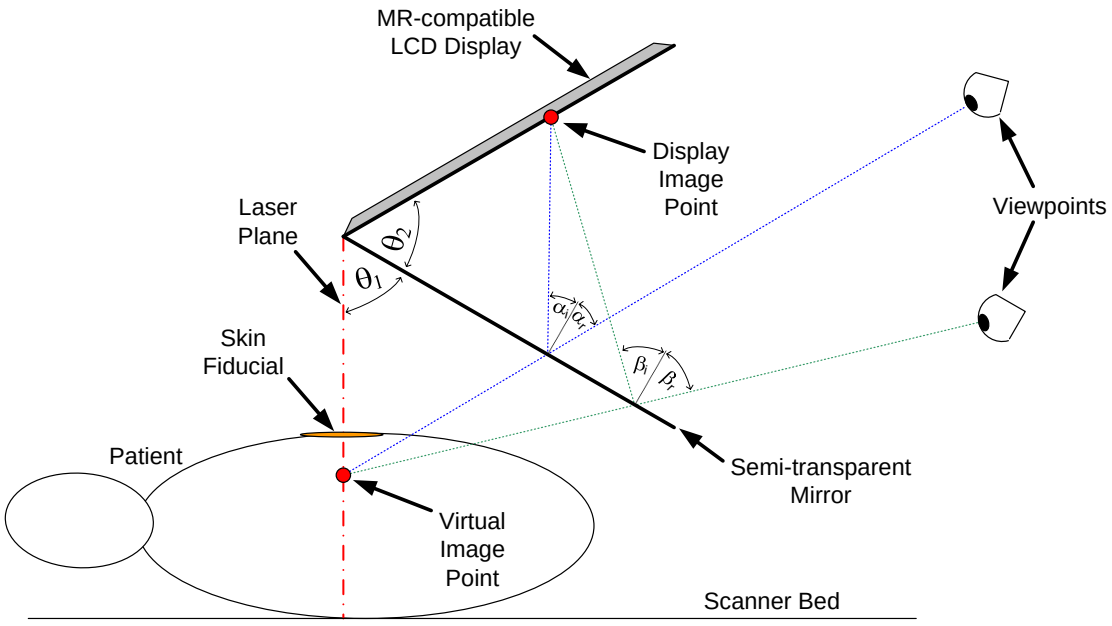

Figure 2.6: Image overlay hardware configuration. An optically stable virtual image that coincides with the scan plane from all viewpoints is produced when $\theta_1 = \theta_2$.

2.3.1.2 System Alignment

The second stage is performed when the overlay system is brought into the scanner room. To ensure parallelism of the scanner's image plane and overlaid image, a calibration phantom is manually adjusted on the MR table until the scanner's transverse laser plane sweeps it's vertical face; the scanner bed is then translated out and the overlay is positioned such that it's onboard laser line generator does the same. This stage is based on the assumption that the scanner's laser line generator sweeps a plane parallel to it's transverse/axial images. Although there is evidence that this is not always the case, our experiences have show this to be a suitable assumption. A description of laser alignment and table positioning accuracy for CT is presented by Court, *et al.* [97].

2.3.1.3 Image Registration

The first step of the in-plane registration process is image scaling. The overlay image must appear in correct size in the mirror, but there is variable linear scaling between the CT image and displayed image. Let $\begin{bmatrix} u_c \\ v_c \end{bmatrix}$ and $\begin{bmatrix} u_d \\ v_d \end{bmatrix}$ be a vector in the MR image and display image, respectively, in pixel units. Also, let $(p_{cx}, p_{cy}$ and $(p_{dx}, p_{dy}$ be the pixel size in the MR image and display image, respectively, in millimeters/pixel unit, in x and y directions. The pixel size of the display is constant and is known from the manufacturers specification or by direct measurement. The pixel size of the MR image is calculated as the ratio between the field of view (in millimeters) and image size (in pixels), both are known from the scanning protocol that is encoded in the header of the DICOM image. Then, the scale factors in

x and y directions are calculated as $s_x = p_{cx}/p_{dx}$ and $s_y = p_{cx}/p_{dx}$, respectively. The in-plane scaling between the MR and display image vectors is described in Equation 2.2.

$$\begin{bmatrix} u_d \\ v_d \end{bmatrix} = \begin{bmatrix} s_x & 0 \\ 0 & s_y \end{bmatrix} * \begin{bmatrix} u_c \\ v_c \end{bmatrix} \tag{2.2}$$

Having dealt with scaling, the second step of in-plane registration is to determine a 3-DOF $\in SE(2)$ rigid body transformation. An MR image of either a calibration phantom or of the patient with fiducials placed on the skin is acquired, and the image is rendered on the overlay display as seen in Fig. 2.9. The in-plane rotation $\in SO(2)$ and translation $\in \mathbb{R}^1$ of the overlaid image is adjusted until each fiducial marker coincides with its mark in the image. This calibration process is similar to that of the CT Image Overlay which is described in depth in [94, 95].

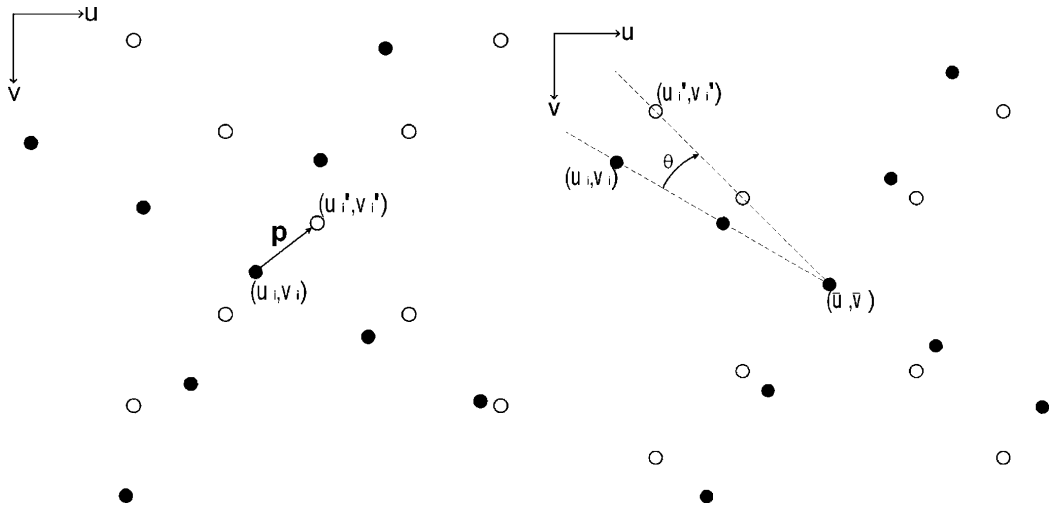

Figure 2.7: Image overlay 3-DOF in-plane registration. Rigid 2-DOF translation (a) and 1-DOF rotation (b).

The in-plane translation is used to align a specific point as shown in Fig. 2.7(a). This point is then selected as the center of rotation, and the in-plane rotation about this point is performed as shown in Fig. 2.7(b). The 3-DOF transformation is applied to the rendered images using the following workflow:

1. Choose a point in the MR image, and then choose the corresponding point as seen through the mirror (typically a fiducial marker).

2. Calculate the required translation $\vec{p}$ to align the selected point.

3. Translate all image points, $\left[\begin{smallmatrix} u_i \\ v_i \end{smallmatrix}\right]$, using:

$$\begin{bmatrix} u_i' \\ v_i' \end{bmatrix} = \begin{bmatrix} p_x \\ p_y \end{bmatrix} + \begin{bmatrix} u_i \\ v_i \end{bmatrix} \tag{2.3}$$

.

4. Determine the rotation angle θ about the selected point to best aligns the remainder of the image points.

5. Rotate all image points, $\left[\begin{smallmatrix} u_i \\ v_i \end{smallmatrix}\right]$, about the chosen center of rotation, $\left[\begin{smallmatrix} \bar{u} \\ \bar{v} \end{smallmatrix}\right]$, using:

$$\begin{bmatrix} u_i' \\ v_i' \end{bmatrix} = \begin{bmatrix} \cos\theta & \sin\theta \\ -\sin\theta & \cos\theta \end{bmatrix} * \begin{bmatrix} u_i - \bar{u} \\ v_i - \bar{v} \end{bmatrix} + \begin{bmatrix} \bar{u} \\ \bar{v} \end{bmatrix} \tag{2.4}$$

.

6. Display the adjusted image. (Note that the pixels in the adjusted image are interpolated, as it is always the case in rotated images.)

7. Make a visual assessment of the alignment. Iterate the process as necessary to achieve adequate registration.

The primary sources of error include the mechanical alignment and image registration. Due to the precision of the mechanical alignment, the primary contributor is the intra-operative alignment of the overlaid image to the patient anatomy. This error is typically based upon the user's ability to align the fiducial marks in the virtual image with the physical markers. However, due to the properties of the overlay's mirror, there is an induced error due to parallax. This error is fully described in [95], and is visually depicted in Fig. 2.8.

The combined effects of human and optical errors on synthetic data was analyzed, with the objective to determine the optimal number, distribution, and selection order of registration points. Two sets of points (i.e. the fiducials and their respective image coordinates) were artificially misaligned by applying a known transformation on each pair and adding noise to each data point, as explained in Fig. 2.8 (a).

Let Q and R be the corresponding points to register in CT and real space. To simulate the error induced by the user and the physical property of the semi-transparent glass, "noise" was added to the position of R, obtaining point P. P was registered to Q resulting in rigid-body transformation T_{reg}. Using this transformation, R was transformed to obtain S. Therefore, the system error was the distance between points S and Q. Human error was simulated by adding a random value (± 2 pixels) to the position of the point to be registered.

Parallax error from the mirror may induce a significantly large error. The error increases

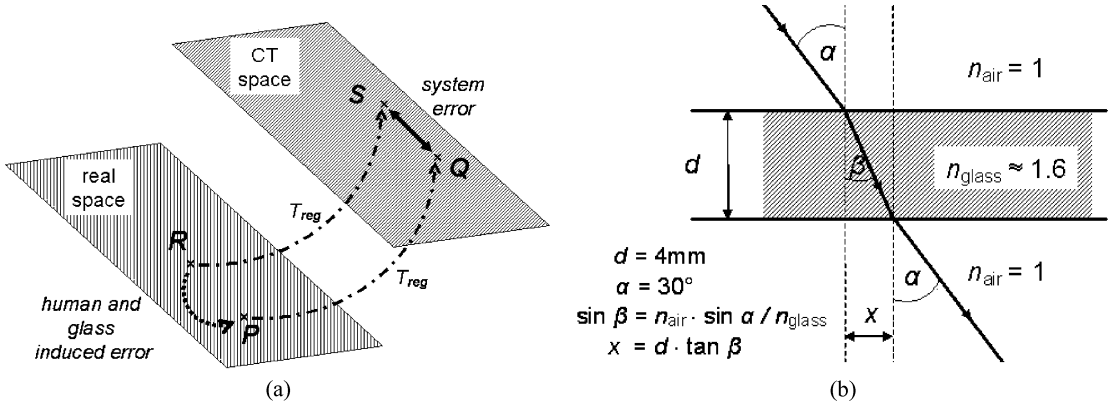

Figure 2.8: Sources of error due to parallax in overlay registration. Registration error definition (a) and calculation of parallax error (b).

with thickness of the mirror; unfortunately, error increases with thickness but so deflection of the mirror surface and also the likelihood of breakage. Therefore, the optimal thickness was determined to be $4mm$. At $d = 4mm$ thickness and $\alpha = 30^o$ view angle and using the formulas derived in Fig. 2.8 (b), the parallax error was $x = 1.28mm$, the effect of which fortunately can be substantially reduced by altering the view points during the calibration process. It is particularly important to compensate for the parallax error by altering the viewpoint. The registration error, using four pairs of registration points and assuming ± 2 pixels human error was $1.23mm$ ($STD = 0.31mm$) at $\alpha = 30^o$ view angle and $0.74mm$ ($STD = 0.21mm$) at perpendicular view ($\alpha = 0^o$). This performance appears to be adequate for most MR-guided needle placement procedures.

2.4 System Integration

To use the system, a small stack of transverse images are acquired near the region of interest where skin fiducials have been placed on the patient. One image from this set is selected as the guidance image and transferred to the planning workstation. The software flips the image as required, adjusts its in-plane orientation and magnification, superimposes additional guidance information (e.g. virtual needle guide, ruler and labels), and renders the modified image on the flat panel display.

2.4.1 Clinical Workflow

In order to increase patient safety and reliability in data reporting, the calibration and system setup may be verified before each experiment and especially before treating each individual patient. Assuming a pre-procedurally aligned system, the intra-procedure workflow is as follows:

1. Place the patient on the table and place imaging coil over the target site.

2. Prepare the site of intervention and place sterile skin fiducial (TargoGrid from Invivo Corp., Orlando, FL) with the parallel bars orthogonal to the approximate slice direction.

3. Translate the patient into the scanner and acquire a thin slab of MRI images with appropriate slice thickness for lesion conspicuity.

4. Transfer the image directly in DICOM format to the planning and control software implemented on a stand-alone PC.

5. Select the target of interest and the percutaneous puncture point as shown in Fig. 2.9(a).

6. Display a visual guide along the trajectory of insertion and render the image on the overlay device.

7. Translate out the table with the patient such that the selected entry point is under gantry's laser plane and mark where the laser plane interests the fiducials; continue to translate out the table such that the mark intersects the overlay's laser plane.

8. Verify the alignment of the overlay image to the patient, and if necessary, update the in-plane alignment as described in Section 2.3.1.3.

9. Place a depth marker on the needle based on displayed depth guide.

10. Take the needle in hand, reach behind the mirror, touch down on the selected entry point, and rotate the needle to match with the virtual guide while keeping it in the laser plane as shown in Fig. 2.9(b).

11. Verify that the respective fiducials on the patient and in image coincide; the skin fiducials can be used to gate or synchronize the needle insertion to the respiratory cycle.

12. Insert the needle to the predefined depth while maintaining in plane and out of plane alignment.

13. Translate the patient back into the scanner and acquire a confirmation image (Fig. 2.9(c)); if the needle position is satisfactory, perform the rest of the intervention (contrast injection, harvest tissue sample, etc.)

Figure 2.9: MR image overlay guided direct MR arthrography in cadaver trials. Planning software with targeting image and overlaid guide (a), needle insertion using overlay guidance (b), and confirmation image with overlaid targeting plan (c).

2.5 Evaluation

2.5.1 Cadaver Trials

The MR overlay system as shown in Fig. 2.1 (right) has been successfully tested in 1.5T and 3T scanners for MR compatibility. Joint arthrography needle insertions have been performed under MR image overlay guidance on porcine and human cadavers in a 1.5T GE Signa and a 3T Siemens Magnetom Trio scanner using the workflow described in Section 2.4.1.

In the porcine cadaver trials, twelve separate insertions were performed in the joint space of the shoulder of three fresh (within one hour of euthanasia in unrelated studies) porcine cadavers. Insertions were performed using 18G, $10cm$ MR-compatible non-ferromagnetic stainless steel needles (EZ-EM Inc., Lake Success, NY) with insertion depths ranging from 26-$43mm$. In the human cadaver trials, ten separate insertions were performed in the joint space of the hip of two cadavers. Again, insertions were performed using the 18G, $10cm$ MR-compatible needles; insertion depths ranged from 30-$54mm$. Planning and confirmation images from both sets of trials were examined by two board certified radiologists to determine whether the tip of the needle landed in the joint space. The needles were successfully inserted into the joint on the first attempt in all cases. Fig. 2.10 shows the results from ten needle insertions into the hip of a human cadaver. Quantitative accuracy analysis was not possible due to the relatively large paramagnetic needle artifact in the MR images and the lack of distinct target points, and contrast injection was

not reliable due to abnormal distribution in the cadaver tissue.

To demonstrate the ability for guiding percutaneous spinal access, needle insertions have been performed with the MR image overlay on an interventional abdominal phantom (CIRS Inc., Norfolk, VA). Successful access of all anatomical targets was verified in MRI visually; needle artifact and lack of distinct targets again did not allow for precise error measurement. To further verify image overlay capabilities, successful insertions with depths of up to $100mm$ have been performed in porcine cadavers. Functionally similar earlier trials with a CT image overlay (where exact target verification and accuracy assessment is possible) have proven the technique reliable for guiding percutaneous access on human and porcine cadavers [94, 95].

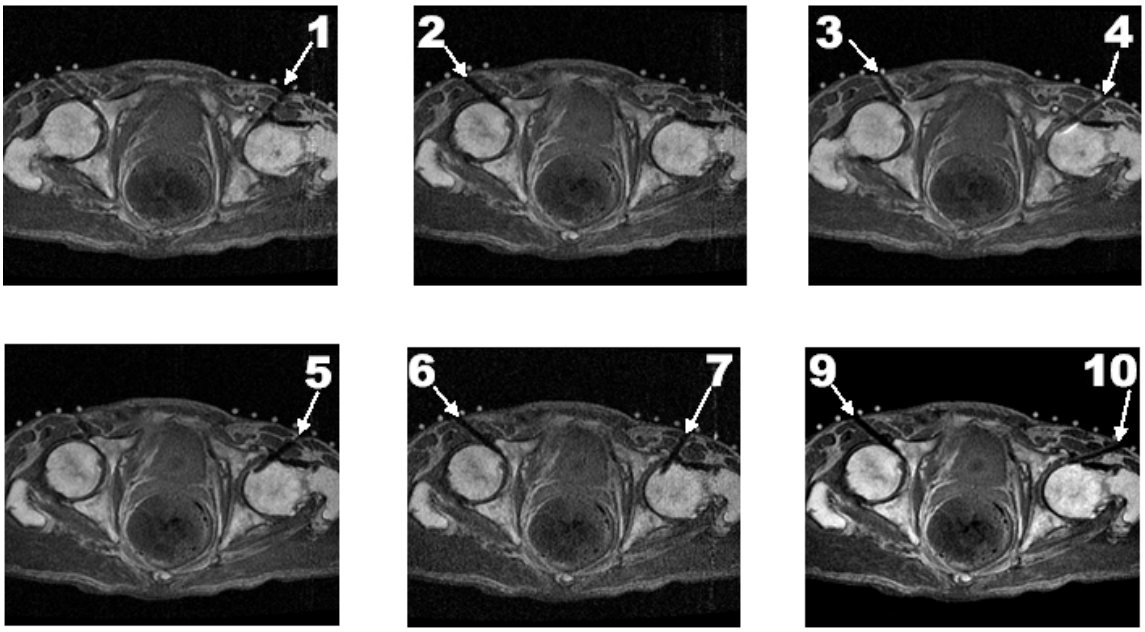

Figure 2.10: Results from ten needle insertions into the joint space of the hip on human cadavers under MR image overlay guidance. The needle tip entered the joint space on the first insertion attempt in all cases.

2.5.2 Comparison of Techniques

To further validate the efficacy and accuracy of MR image overlay guidance, four manual needle insertion techniques were compared[2] :

- **Image overlay** as described above (Fig. 2.12(a)).
- **Biplane laser** that marks the insertion path with the intersection of two calibrated laser planes as described in [99] (Fig. 2.11 and Fig. 2.12(b)).
- **Handheld protractor** with pre-angled guide sleeve (Fig. 2.12(c)).
- **Conventional freehand** needle insertion.

All techniques feature translating patient out of the scanner for insertion, skin fiducials to determine puncture point, and manual needle placement in laser-marked transverse plane. All four are equivalent in controlling out-of-plane angle and depth; therefore, these aspects were not evaluated. Three series of experiments were conducted with 1.5T GE Signa scanner and 18G MR-compatible beveled needles.

The first trial used the CIRS abdominal phantom with TargoGrid fiducials as shown in Fig. 2.12 (a - c); four needle insertions were performed for each technique. In this test, the procedure was performed on the MRI scanner and MRI-based validation was used. All insertions were visually successful, but as expected, needle artifact and lack of distinct targets rendered quantitative measurement inconclusive.

[2]This comparison is based primarily upon work described in "MRI Guided Needle Insertion - Comparison of Four Techniques" that appeared in the proceedings of the Society for Interventional Radiology 31st Annual Scientific Meeting, March 2006 [98].

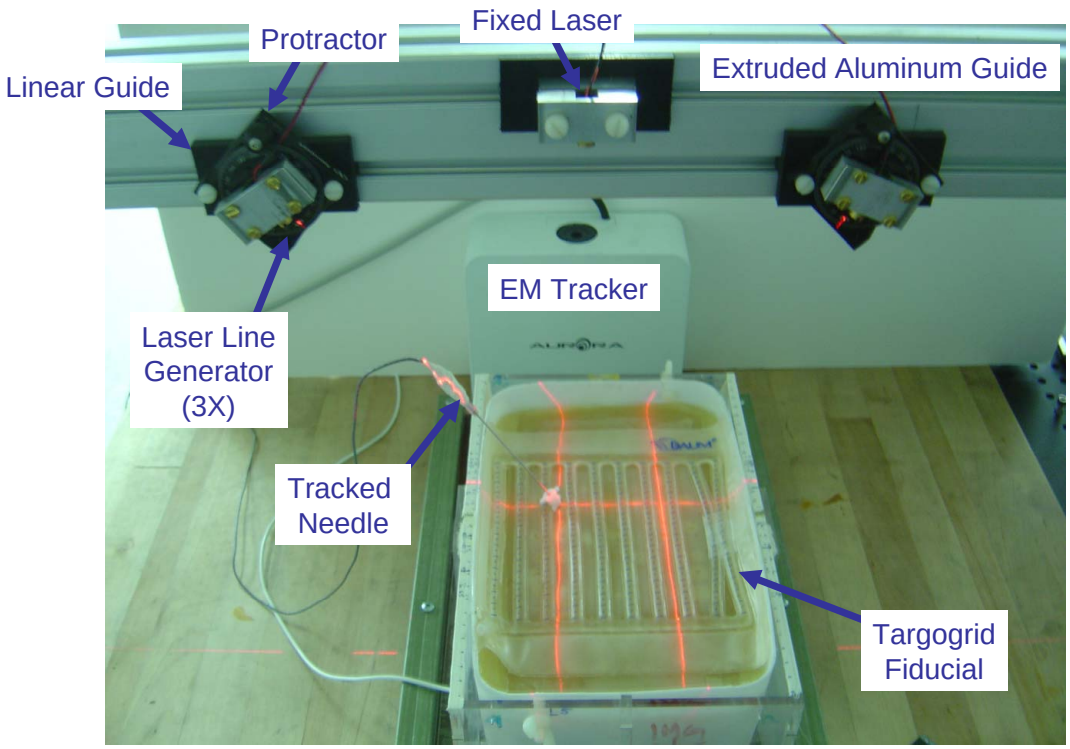

Figure 2.11: Bi-plane laser guide shown in the laboratory configuration. The intersection of the laser planes delineates the needle axis.

A follow-up trial was performed similarly, but four separate needle insertion phantoms were used (one for each technique); these phantoms are of the same type as the last experiment. In this experiment, the same three needle insertions were performed with each technique in the MR scanner, and accuracy measurements were made independently off-line using fluoroscopy as shown in Fig. 2.13. Although the results are not statistically significant due to the small sample size, the average error between the needle and the target was less than $1mm$ for the image overlay; the other techniques ranged in accuracy from $2mm$ to $7mm$ (for freehand). These first two experiments serve as a proof-of-concept for all four techniques in the MR environment.

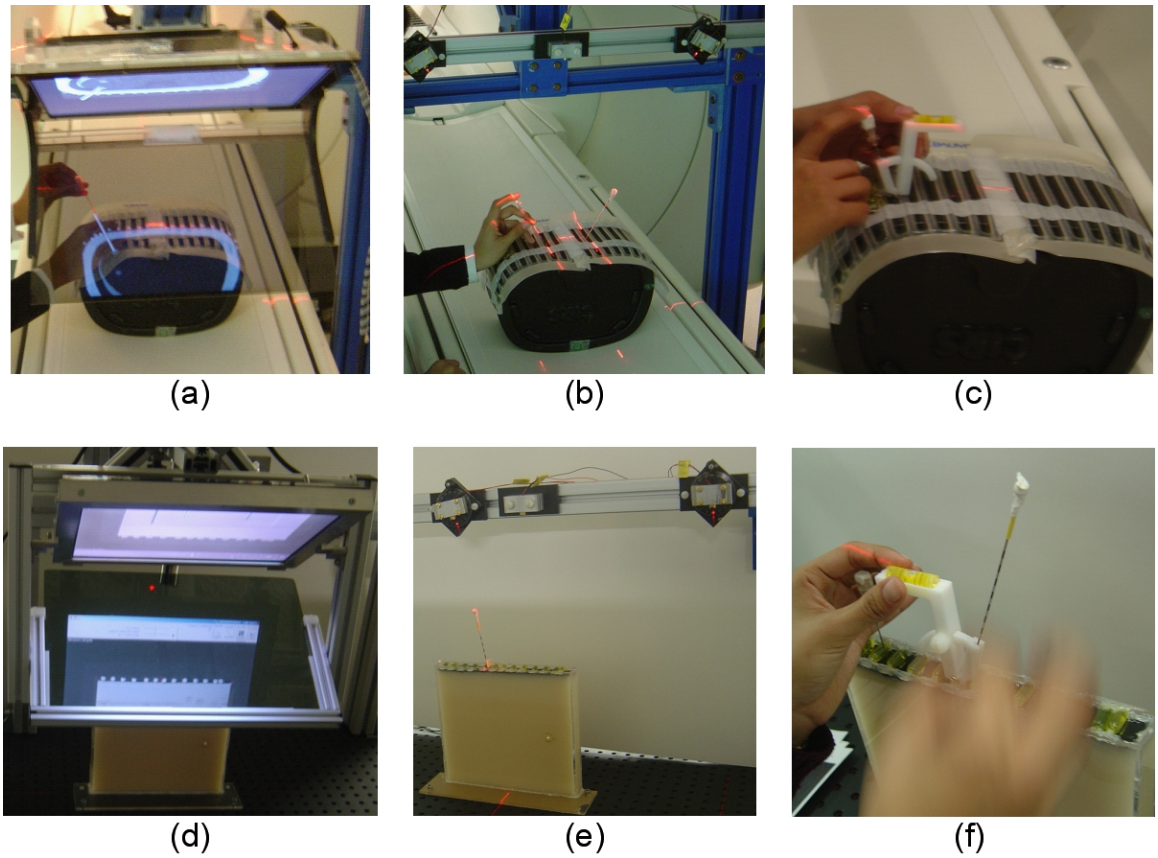

Figure 2.12: Comparison studies between MR image overlay (a,d), bi-plane laser guide (b,e), handheld protractor guide (c,f), and traditional freehand. Initial studies were performed under MR imaging (a–c) and follow up quantitative comparisons were performed the laboratory with a functionally equivalent system configuration (d–f).

The third experiment used a phantom filled with two different stiffness layers of tissue-equivalent gel and five embedded $4mm$ plastic targets, and covered with neoprene skin. This test was performed based on MR images, but conducted on a functionally equivalent configuration of the devices in a laboratory setting as shown in Fig. 2.12(d - f). A total of $n = 30$ insertions were performed with each technique; C-arm fluoroscopy was used to determine in-plane tip position error and needle axis orientation error. This experiment serves as a quantitative comparison in the laboratory of the four techniques. Results from

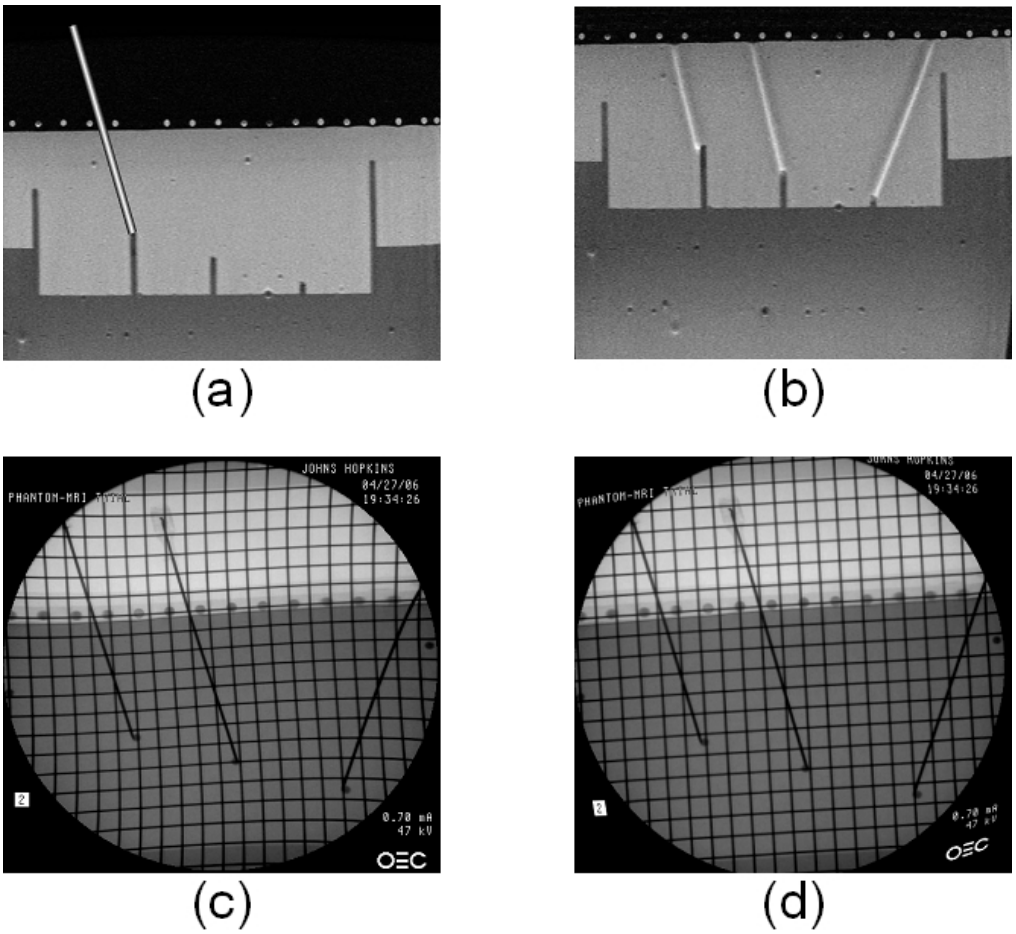

Figure 2.13: Needle insertion validation procedure for MR image overlay phantom trials using fluoroscopy. A plan is generated and overlaid (a), the needle is inserted and a confirmation MR image is acquired (b), the phantom is imaged in a c-arm fluoroscope (c), and measurements are made on a dewarped version of the fluoroscopic image (d).

this trial are shown in Table 2.1. Technique made a significant difference in tip position error ($p = 0.015$) and angle error ($p = 0.053$). With a 75% confidence interval, biplane laser and image overlay provide for better tip placement accuracy than the other techniques. With an 80% confidence interval, biplane laser and image overlay have better angular accuracy than the other techniques. In terms of angular and positional accuracies, no significant difference was found between the laser guide and image overlay in these preliminary stud-

ies. The primary advantage of the overlay is the ability to show anatomical information in addition to guidance based on the plan; as a result, the image overlay would be expected to outperform the laser guide in real applications.

From the comparison studies, enhanced needle insertion techniques appear to provide substantial benefit over conventional needle insertion. In the relatively straightforward phantom experiment, biplane laser and image overlay guidance performed similarly. For cases where it is unnecessary to see the target anatomy, the biplane laser appears adequate. However, when visualization of the target anatomy is preferred, such as when performing needle placement in the joints or other musculoskeletal targets, the image overlay provides significant benefits over other techniques.

Table 2.1: Needle Insertion Results of Quantitative Comparison Between Techniques

Technique	Avg. Position Error (mm)	Std. Dev. Position Err.	Avg. Orientation Error (deg)	Std. Dev. Orientation Err.
Freehand	5.3	5.6	4.1	4.1
Protractor	5.4	7.4	3.4	3.3
Laser	2.9	2.6	2.0	2.2
Overlay	2.0	1.7	2.4	2.3

2.6 Needle Placement Validation System

In order to develop accurate and effective augmented reality (AR) systems used in MR- and CT-guided needle placement procedures, a comparative validation environment is necessary.[3] Clinical equipment is prohibitively expensive and often inadequate for precise measurement. Particularly for measuring needle placement accuracy directly in MRI, precise measurement is greatly limited by paramagnetic needle artifact and lack of distinct small targets. Fig. 2.14 shows an extreme example obtained when inserting an stainless steel needle (not specifically MR-compatible) into a phantom.

Liu, *et al.* [100]quantitatively describe needle artifact in MR imaging , and DiMaio, *et al.* [101] describes the variable location of the needle artifact. Nour, *et al.* [24] describe ways of improving needle artifact visualization through optimizing scan parameters, but there is still a clear variability in visibility and localization of the needle tip. Further, scanner time cost can exceed $500/hour making statistically significant trials impractical. George, *et al.* [102] describe an augmented reality training system for MRI-guided needle biopsy, but still require external optical tracking and is not well suited for the task at hand.

Therefore, a laboratory validation system for measuring operator performance using different assistance techniques was developed. The validation system can be applied to varying methods of assistance ranging from augmented reality guidance methods to tracked navigation systems and autonomous robots. Electromagnetically (EM) tracked needles are

[3]This section is based primarily upon "Validation System of MRI Image Overlay and Other Insertion Techniques" that appeared in Studies in Health Technology and Informatics, January 2007 [89]. This work was performed in collaboration with Eva Dyer.

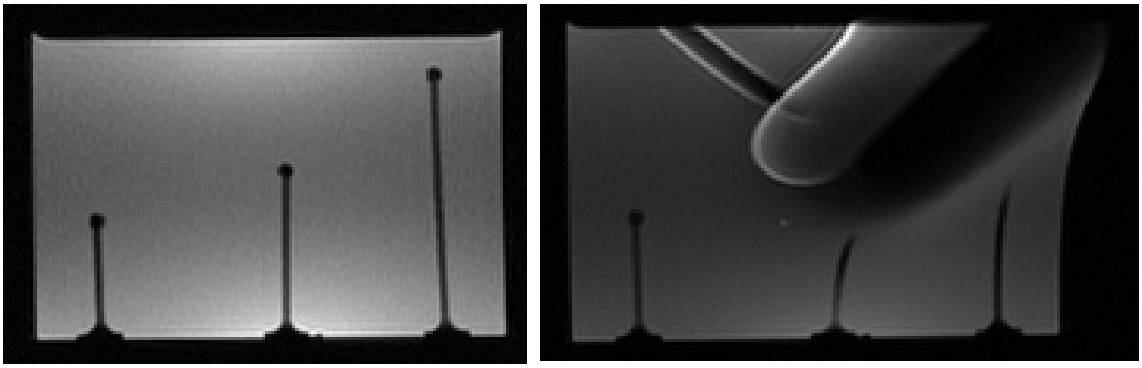

Figure 2.14: Example of MR image distortion. A non MR-compatible stainless steel needle is inserted into a phantom causing significant signal distortion and signal loss. Both the before (left) and after insertion (right) images are shown at the same window level.

registered with the preoperative plan to measure placement accuracy and the insertion path. The validation system provides an independent measure of accuracy that can be applied to varying methods of assistance ranging from augmented reality guidance methods to tracked navigation systems and autonomous robots. In preliminary studies, this validation system is used to evaluate the performance of the image overlay, bi-plane laser guide, and traditional freehand techniques.

Preliminary assessment of the accuracy of the MR image overlay system has been performed as described in Section 2.5.2, but the excessive cost of scanner time has thwarted a large-scale study of the accuracy of this system. The off-line validation system has been created in order to study needle placement accuracy; of particular interest is the accuracy of the image overlay as compared to that of other insertion guidance methods. This system will also provide a means to study the trajectory and gestures during the insertion procedure in addition to the endpoint accuracy. The study of hand gestures for each of these methods will provide useful information that can be used to help minimize the number of

re-insertion attempts needed, as each re-insertion causes discomfort to the patient. This system ensures a less resource exhaustive and more accurate means by which to validate needle insertion procedures.

The Overlay is shown with the phantom (as described in Section 2.6.1.1) used with the validation system in both MR trials and laboratory experiments in Fig. 2.15(a,c). The bi-plane laser guide uses intersecting transverse and adjustable para-sagittal laser planes to mark the trajectory of insertion [99], and is shown in MR trials and laboratory experiments in Fig. 2.15(b,d).

2.6.1 Electromagnetic Tracker Validation System

Electromagnetic tracking with the NDI Aurora system (Northern Digital Inc., Waterloo, Ontario) is utilized to provide the position of the tip and orientation of the shaft of an instrumented needle (MagTrax Needle, Traxtal Inc., Toronto, Ontario) as described by Wood, *et al.* [103]. All necessary components must be registered with one another in order to track the needle with respect to the preoperative plan generated on the MR/CT images. The components of the system include: the Aurora EM Tracker, a tracked needle, the tracked phantom, the MR/CT images used for pre-operative planning and the AR guidance system. The system is shown in Fig. 2.16.

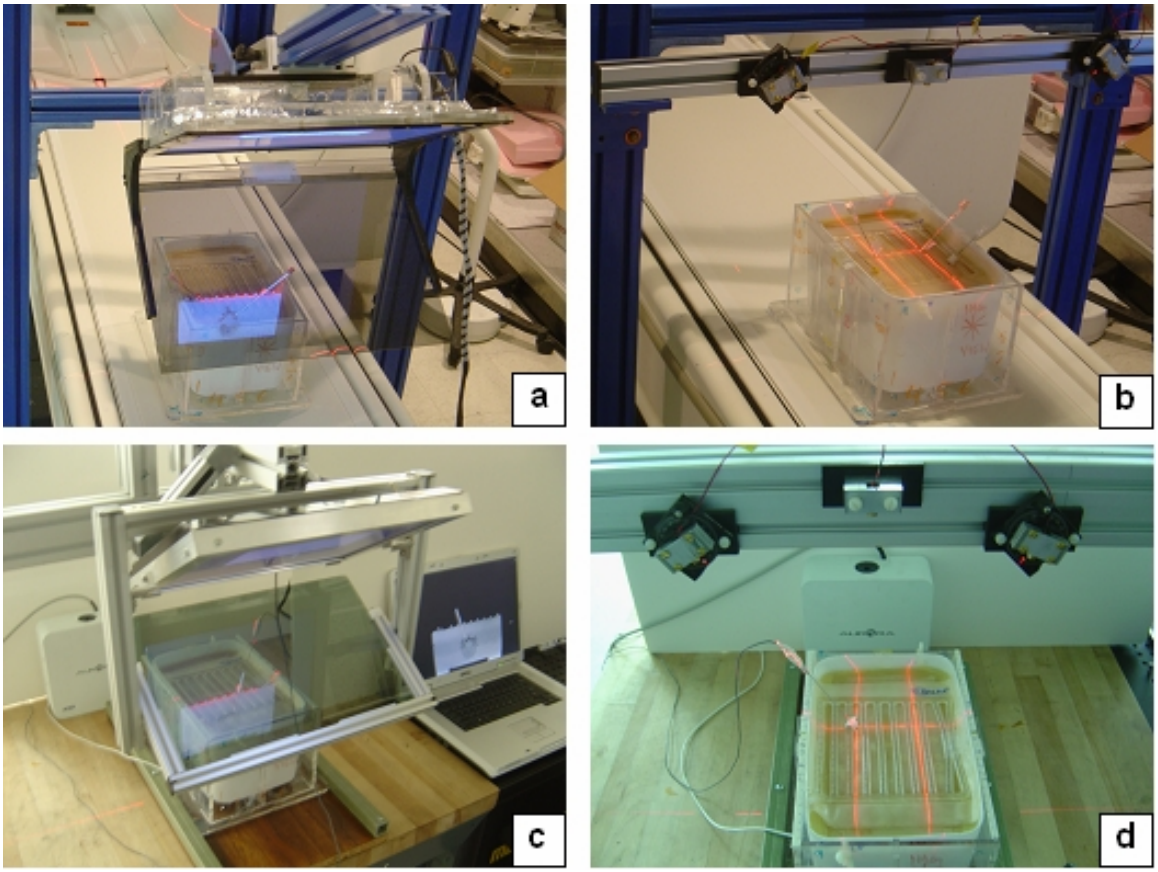

Figure 2.15: Image overlay (a,c) and bi-plane laser guide (b,d) AR needle placement systems with spine phantom. MR scanner feasibility trials (a,b) and laboratory validation system with tracked needle (c,d).

2.6.1.1 Phantom Design

A human cadaver lumbar spine phantom was designed to mimic the anatomy of a patient and aid in the process of registration. Lumbar vertebrae in proper alignment with simulated intravertebral discs is embedded into layered tissue mimicking gel (SimTest, Corbin, White City, OR) of two different densities emulating fat and muscle tissue. The gel phantom with lumbar spine is placed into an acrylic enclosure which was accurately laser-cut with 24 different pivot points spread over four sides for rigid-body registration.

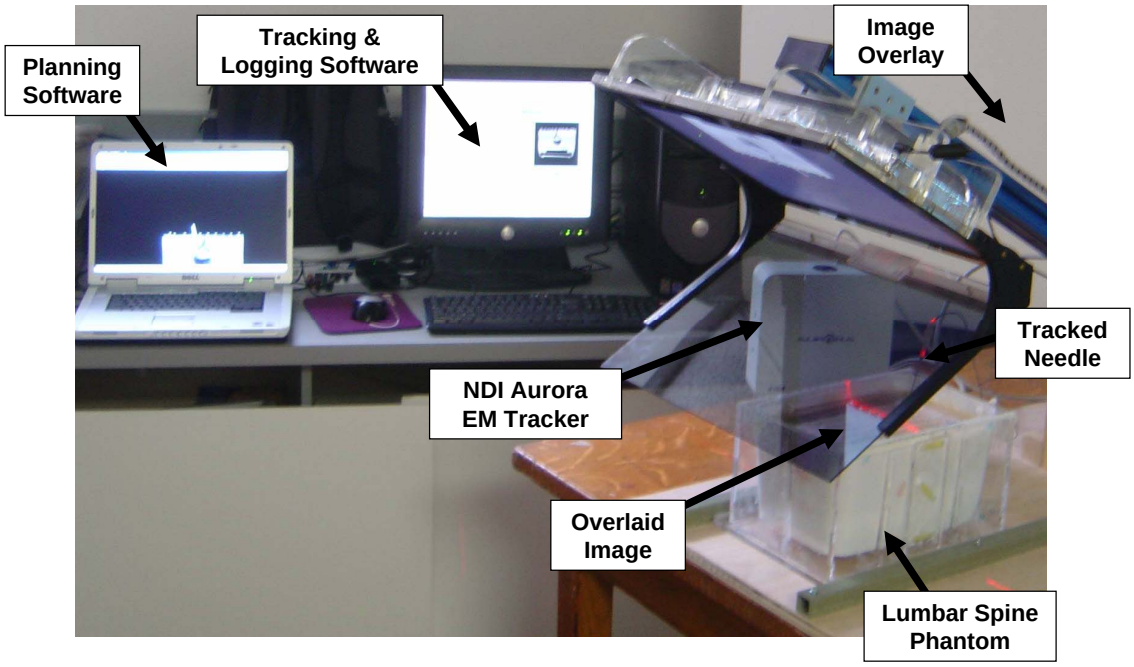

Figure 2.16: The EM tracker validation environment shown with the image overlay system.

Stereotactic fiducial markers (MR-Spots, Beekley Corp., Bristoll, CT) were placed on the phantom in precisely positioned laser-cut slots. The markers were placed in a '**Z**' shape pattern on three sides allowing for automatic registration between anatomical images and the phantom. The acrylic enclosure was designed such that different phantoms can be placed inside it for studying other procedures.

2.6.1.2 MR Image Registration

In order to register preoperatively obtained MR or CT images (and their respective preoperative plans) to their corresponding physical space, techniques similar to those described in [104, 105] were used. The Z-frame registration uses three stereotactic fiducial

markers in the shape of a 'Z' on each of the left, right, and bottom faces of the phantom (Fig. 2.18) in a design very similar to the Brown-Roberts-Wells (BRW) computerized tomography stereotaxic guidance system [106]. Axial images are taken near the center of the phantom; the locations of other images of the phantom are known with respect to this reference. The central image is used for registration, where the nine fiducial markers are segmented by applying an adaptive threshold and then applying morphological operations to the image. The centroid of each marker was then found and the position of each marker with respect to the DICOM image was recorded into a set of nine points. After the nine distinct points were identified, the transformation from the scanner's image space to the phantom's coordinate system was computed. More detail on z-frame registration can be found in Section as the techniques is applied to registration of the robotic system to the scanner. The root-mean-square (RMS) error incurred in the image-to-phantom registration for a typical MR image was $1.26mm$.

2.6.1.3 Electromagnetic Tracker Registration

The NDI Aurora EM tracking system is used to localize an instrumented needle with respect to the phantom in 5-DOF (needle axis orientation and tip location). A 6-DOF reference tool is fixed to the phantom and a calibrated pointer tool is used for rigid-body registration of the phantom to the tracker. Data was obtained by pivoting about the 24 pre-defined divot points with the pointer. These points were used for registration between phantom coordinate system and that of the EM tracker by finding the transformation which

Figure 2.17: Phantom design showing human cadaver spine partially embedded in tissue equivalent gel. Fiducial markers are shown both on the phantom and the corresponding MR image.

aligns the known point locations obtained from the mechanical design specifications with the collected data points using Arun's method [107]. The RMS error incurred in the rigid-body registration was $0.93mm$. Fig. 2.17 shows how the needle is localized in the image coordinates where the planned trajectory was made.

This registration process requires only 5-10 minutes and is necessary only when the 6-DOF reference body tool is repositioned on the phantom. The rest of the registration process is automatic. Once both steps in registration are complete, an instrumented needle may be tracked as it maneuvers along a planned path within the phantom. To maximize the system's accuracy, future efforts will include distortion mapping and error compensation as described in [108].

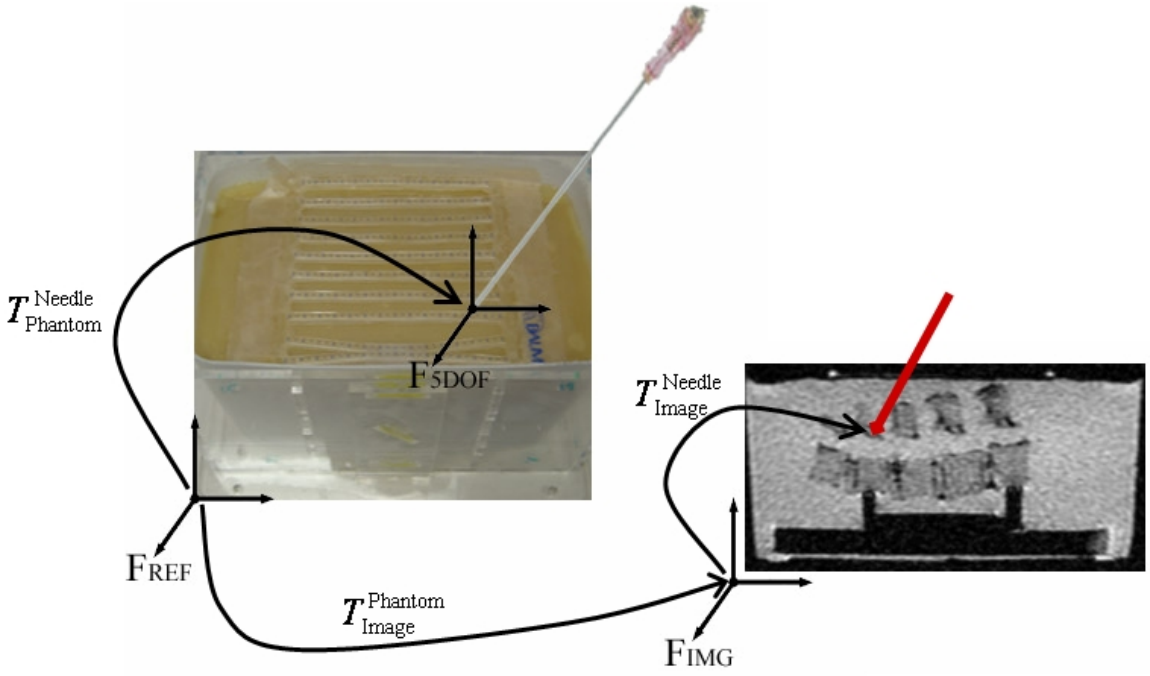

Figure 2.18: Frame transformations for the registration process shown on the spine phantom and its corresponding MR images. The tracked needle is represented in the original image space where the preoperative plan was made.

2.6.2 Experimental Methods

Prior to beginning trials, numerous randomly selected paths in random MR slices were created in the graphical user interface planning software described in [88]. The software stores the insertion and target points for each planned path as well as the angle of insertion needed to accurately reach the desired target.

For each of the three needle insertion methods evaluated (image overlay, bi-plane laser guide and freehand interventions), subjects were randomly assigned three different paths in three different axial MR slices. The entire insertion attempt was recorded with the tracking software. The software then provides insertion and target point error, both in and out of the

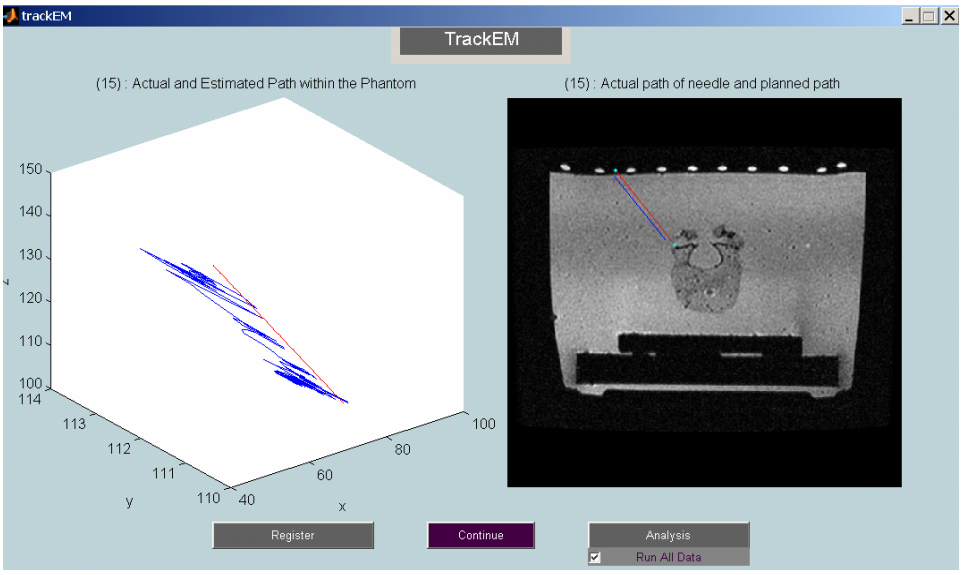

Figure 2.19: Software interface for the EM tracked validation environment. The planned and actual needle axis are displayed as well as the tip trajectory over time.

image plane as shown in Fig. 2.19. Needle axis orientation error is also computed. Simple forms of gesture tracking are now provided, including distances from the trajectory during insertion and the number of re-insertion attempts. Fig. 2.20 shows the workflow and view when using the validation environment.

2.6.3 Results

The number of re-insertion attempts and gesture tracking information provided by the tracking software is useful in evaluating the image overlay and bi-plane laser AR guidance systems. In typical needle placement procedures, the interventionalist will often probe the patient's anatomy until the desired target is reached. This probing action results in great discomfort to the patient as well as bruising to the area. Reduction of the number of

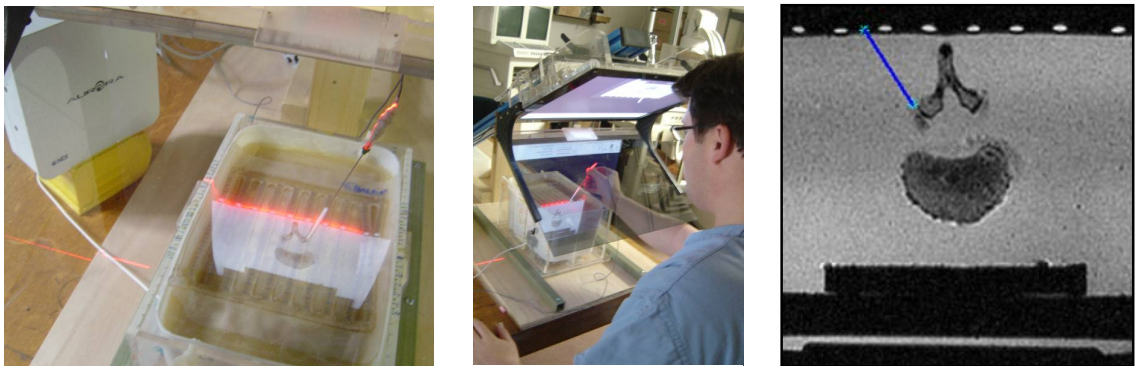

Figure 2.20: The validation system workflow. View of the anatomy and needle guide overlaid on phantom (left), needle insertion with needle tracking (center) and validation with respect the plan (right).

re-insertion attempts results in the effectiveness of the guidance method. If this analysis information was provided to the interventionalist in training, more accurate results may be obtained. Further, real-time feedback may be provided to the user during the intervention so they may be aware of their current position with respect to the anatomical images. This may also reduce the discomfort to the patient and increase target accuracy.

To demonstrate workflow, four needle insertions were performed with each technique in the clinical MRI environment. As expected, accuracy could not be assessed due to large artifacts as shown in Fig. 2.22(a). In the validation testbed, the measured needle trajectories were graphically overlaid on the plan and targeting MR image as shown in Fig. 2.22(b).

Twenty insertions were performed with each technique. Position and orientation errors were measured. Initial analysis showed that the results correlate with direct validation performed using fluoroscopy described in Section 2.5.2. The Image Overlay's mean error in the image plane was $1.4mm$ and 2.5^o with standard deviations of $0.5mm$ and 1.9^o respec-

tively. The Laser Guide's average error was $1.8mm$ and 2.0^o ($1.2mm$ and 1.8^o standard deviation), and Freehand produced average errors of $2.0mm$ and 5.2^o ($1.4mm$ and 2.3^o standard deviation).

To evaluate the clinical effectiveness of the training and validation environment, three interventional radiologists performed needle insertions using image overlay guidance while monitoring insertion trajectory. The results include 57 total insertion attempts from the three users. The insertions are about evenly split between left and right handed. The average depth for the trials was $39.5mm$ and the average angle from the vertical was 25.9^o. The average targeting error is $4.7mm$ with an average in-plane error of $4.2mm$ and an average out of plane error of $1.7mm$. The average angular error is 2.5^o. When left handed and right-handed insertions are compared, right-handed appears to be slightly better in accuracy and consistency. Table 2.2 shows the results from 60 insertions using overlay guidance from one of the radiologists with experience using the system.

Table 2.2: Needle Insertion Accuracy for a Radiologist Using Image Overlay (N=60)

	Avg. Position Error (mm)	Std. Dev. Position Err.	Avg. Orientation Error (deg)	Std. Dev. Orientation Err.
In Plane	3.5	2.0	2.1	1.2
Out of Plane	1.5	1.1	N/A	N/A

2.7 Discussion

2.7.1 Overlay System

Initial cadaver and phantom experiments support the hypothesis that the MR image overlay can provide accurate needle placement while significantly simplifying the arthrography procedure by eliminating separate radiographically guided contrast injection. The system also appears to be useful in spinal needle placement, however, independent measurement of accuracy will have to support this claim in later trials. In our studies, by visualizing target anatomy and providing a visual guide, the MR image overlay allowed for accurate needle placement on the first attempt consistently.

There were many lessons learned and hurdles overcome in the development of this system. The first hurdle was transition from the CT-compatible system to MRI, which required ensuring MR compatibility of the flat panel display. The current display is standard LCD display that had the steel casing removed and replaced with aluminum EM shielding. The current display can function adequately up to 1m from the scanner bore before saturation of the ferrite core inductors; we are investigating options that will allows the overlay unit to be moved in closer proximity to the scanner.

Another issue that arises with 2D image overlay in general is parallax as described in [95]; the key is to optimize the parallax error by decreasing the thickness of the mirror, while maintaining rigidity of the mirror to eliminate sagging. We have settled on $4mm$ thick smoked acrylic sheets as the semi-transparent mirror material. Visibility of the over-

laid image on the mirror is dependent on the room lighting; dimming the lights enhances the overlaid image, but in turn decreases the visibility of the patient and the needle behind the mirror. Typically the lights behind the clinician are dimmed while maintaining illumination on the opposite side; the optimal configuration appears to be based on user preference.

Calibration of the device is an aspect that has evolved significantly from early attempts with the 2D CT Image Overlay. The original belief was that a full calibration of the in plane alignment was necessary during set up of the system. The procedure has since evolved into simply aligning the image in the overlay with the skin fiducials on the patient; this is faster by eliminating a step, simpler to perform, and safer since in guarantees alignment of the guide with the patient at the time of insertion. Further, this eliminates the need for a special calibration phantom for alignment with the patient as described in Section 2.3.1.

During the experiments, it was revealed that holding the needle in the plane of insertion can be difficult, especially for non-expert users. In an attempt to ease this problem, a mechanical needle guide - a horizontal bar was attached to the display-mirror unit - was implement as shown in Fig. 2.21(a). The bar is made of acrylic and its height is adjustable. The operator places the needle at the skin entry point and presses the needle gently against the bar while inserting the needle. A stronger constraint can be provided by adding a sliding-rotating needle guide with a quick release mechanism shown in Fig. 2.21(b). Although mechanical constraints are redundant in addition to optical guidance, they appear to be very useful for increasing the level of comfort and confidence of *some*

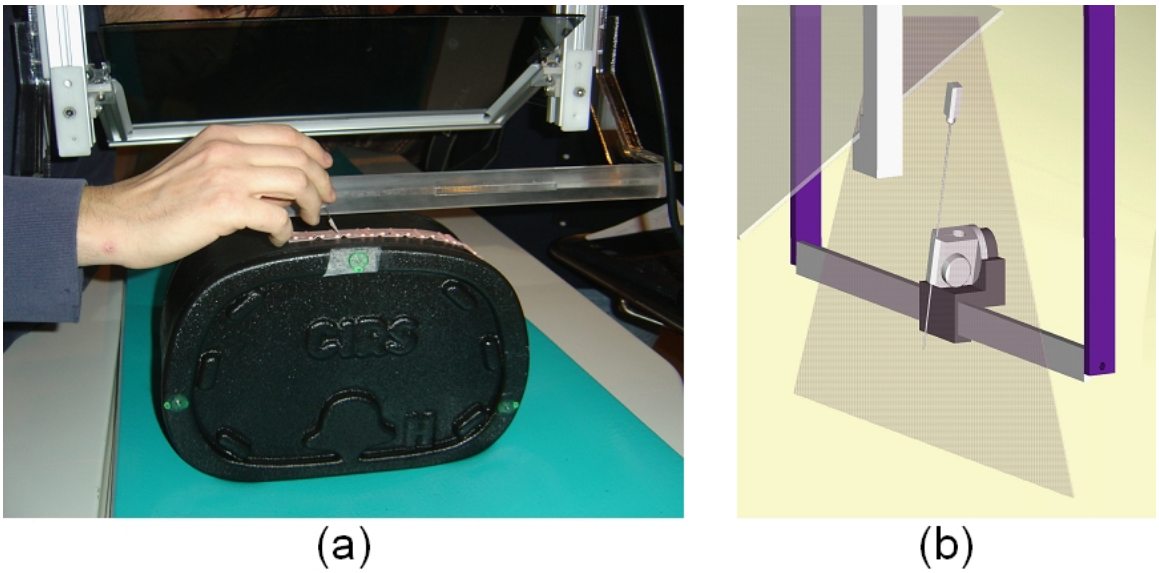

Figure 2.21: Mechanical needle guide for maintaining the needle orientation in the image plane (a) and design of an adjustable angle needle guide to maintain both in plane and out of plane orientation (b).

operators. Preliminary results suggested that as the user becomes more accustomed to the image overlay device, the benefits of mechanical constraints are reduced and can in fact become a hindrance.

2.7.2 Technique Comparison

Initial assessments of the image overlay, laser guide, and freehand needle insertions were performed with the system. Experiments with experienced radiologists are currently underway. Future experiments will provide independent, large scale accuracy assessment of needle insertion procedures using commercial surgical navigation systems, image overlay, laser guidance, and traditional techniques. The goal is to quantitatively compare placement accuracy, consistency, and other important characteristics such as the needle trajecto-

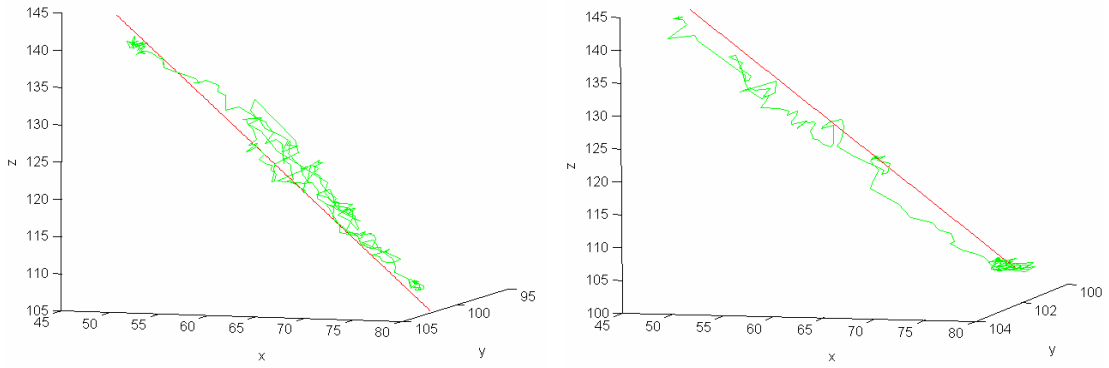

Figure 2.22: Needle insertion trajectories: path with multiple corrections (left) and a direct path (right).

ries throughout the entire placement procedure.

In typical needle placement procedures, the interventionalist will often probe the patient's anatomy until the desired target is reached. This probing action can result in a great deal of discomfort to the patient as well as significant bruising to the area. Analysis of the needle trajectory can provide information about the number of insertion and repositioning attempts that were made during an intervention. Fig. 2.22 (left) shows a path that resulted from repeated reinsertions and Fig. 2.22(right) shows a typical result from a good insertion on the first attempt. This information enables researchers to study the systems' ability to minimize discomfort to the patient during the procedure. The next stage is to incorporate gesture tracking techniques similar to those described by Lin, *et al.* [109].

2.7.3 Future Work

Presently, institutional review board (IRB) approval is being sought to commence clinical trials for MR image overlay guided joint arthrography. The current overlay system is limited to the transverse plane. Concurrently, a "dynamic" overlay system is in development. This will be smaller in size and moved over the body to allow for needle insertion in arbitrary tilted planes, thereby significantly increasing the flexibility and user friendliness of the system. as shown in Fig. 2.23.

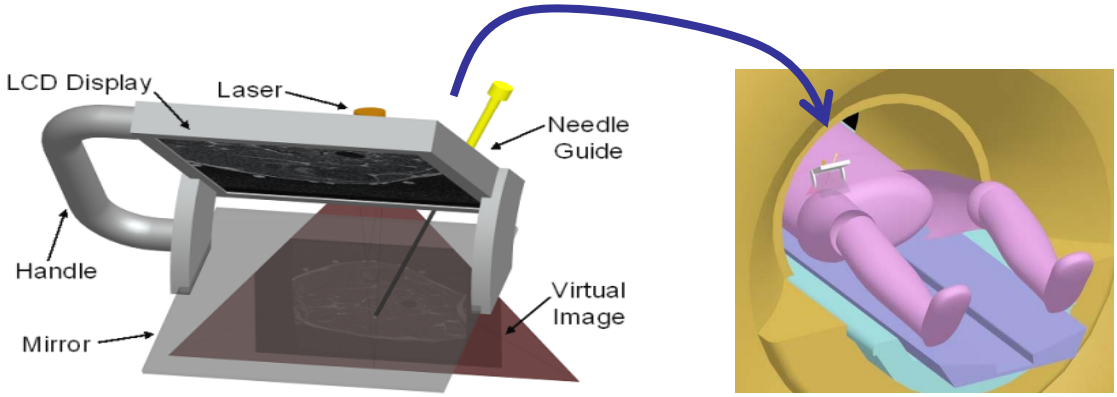

Figure 2.23: Conceptual design of a compact, mobile overlay device.

A further goal is implementing the tracking system in clinical trials within a CT scanner, while utilizing the gesture tracking information given by the system for planning interventions. Future applications of this system may also include providing realtime accuracy and position feedback to a user in vivo, and evaluating new clinicians in the accuracy of their needle placement procedures in clinical training settings. Applications of the validation system may also be extended further into autonomous robotic systems and other

augmented reality systems.

2.8 Conclusion

The Image Overlay system provides a method for presenting medical images in the appropriate pose on the patient in the operative field during an intervention. This is the first reported clinally feasible system for providing *in-situ* imaging to help guide needle insertion procedures in the MRI scanner room. The MR Image Overlay uses a unique geometry and seamless workflow to enable high precision needle placements through the use of additional information presented at the interventional site, without interfering with or slowing down the traditional procedure.

In the human cadaver trials, ten separate insertions were performed in the joint space of the hip of two cadavers. Again, insertions were performed using the 18G, $10cm$ MR-compatible needles; insertion depths ranged from 30-$54mm$. Planning and confirmation images from both sets of trials were examined by two board certified radiologists to determine whether the tip of the needle landed in the joint space. The needles were successfully inserted into the joint on the first attempt in all cases.

To further validate the efficacy and accuracy of MR image overlay guidance, four manual needle insertion techniques were compared. A total of 30 insertions were performed with each technique; C-arm fluoroscopy was used to determine in-plane tip position error and needle axis orientation error. Technique made a significant difference in tip position er-

ror ($p = 0.015$) and angle error ($p = 0.053$). With a 75% confidence interval, biplane laser and image overlay provide for better tip placement accuracy than the other techniques. The primary advantage of the overlay is the ability to show anatomical information in addition to guidance based on the plan; as a result, the image overlay outperforms the laser guide in real applications.

In order to develop accurate and effective augmented reality (AR) systems used in MR- and CT-guided needle placement procedures, a comparative validation environment was developed. The validation system can be applied to varying methods of assistance ranging from augmented reality guidance methods to tracked navigation systems and autonomous robots. Electromagnetically (EM) tracked needles are registered with the preoperative plan to measure placement accuracy and the insertion path. In preliminary studies, this validation system is used to evaluate the performance of the image overlay, bi-plane laser guide, and traditional freehand techniques. Twenty insertions were performed with each technique. The Image Overlay's mean error in the image plane was $1.4mm$ and 2.5^o with standard deviations of $0.5mm$ and 1.9^o respectively. The Laser Guide's average error was $1.8mm$ and 2.0^o ($1.2mm$ and 1.8^o standard deviation), and Freehand produced average errors of $2.0mm$ and 5.2^o ($1.4mm$ and 2.3^o standard deviation).

Initial cadaver and phantom experiments support the hypothesis that the MR image overlay can provide accurate needle placement while significantly simplifying the arthrography procedure by eliminating separate radiographically guided contrast injection. In typical needle placement procedures, the interventionalist will often probe the patient's

anatomy until the desired target is reached. This probing action can result in a great deal of discomfort to the patient as well as significant bruising to the area. Analysis of the needle trajectory can provide information about the number of insertion and repositioning attempts that were made during an intervention. This information enables researchers to study the systems' ability to minimize discomfort to the patient during the procedure.

Chapter 3

MRI-Compatible Robotic System

The MRI Robot system provides a method for performing image-guided interventions using real-time MRI images from traditional diagnostic, long-bore, high-field magnets to guide and needle insertion procedures.[1] This is in stark contrast to much of the prior work in MRI-guided interventions, such as manual attempts by Lewin, *et al.* [25] and robotic attempts by Chinzei, *et al.* [42] that are based upon the use of a low-field, open, specialized interventional magnet as described in Section 1.1.2. These magnets are often very specialized, expensive, hard to come by, and of lower image quality than a high-field ($\geq$1.5T) system. *Thus, the overriding goal of this work is to make high-field MRI available and practical for interventional procedures.*

[1] This description is based primarily upon "MRI-Compatible Pneumatic Robot for Transperineal Prostate Needle Placement" that appeared in IEEE/ASME Transactions on Mechatronics MRI Special Issue, June 2008 [90]. This work was performed in collaboration with Iulian Iordachita and Csaba Csoma at Johns Hopkins and Noby Hata, Clare Tempany, Junichi Tokuda and Philip Mewes at the Brigham and Women's Hospital.

3.1 Motivation and Goals

To date, there have been only a handful of attempts to develop MRI-compatible systems to assist in needle placement in closed bore scanners. These systems range from encoded, manually actuated devices such as that presented by Krieger, *et al.* [43, 84] for prostate biopsy, to fully automatic systems such as that presented by Stoianovici, *et al.* [87] for brachytherapy implantation. Thus far, there has been no system that maintains the workflow of traditional procedures in a compact, reliable and convenient platform while enabling the use of intra-operative MRI. The robotic system presented here has several significant advantages over the present state-of-the-art systems, which are described more fully in Section 1.1.5.2.

The system developed as part of this work has many advantages over the existing state of the art. With regards to clinical viability, the MRI robotic system maintains the patient position in the semi-lithotomy pose and uses the transperineal access route for needle insertion. This allows for accurate registration or pre-operative and pre-procedural planning images (typically acquired in that pose). Further, this allows the robot to act as an "Automated Template", mimicking the functionality of the conventional brachytherapy template. However, the robotic system enhances the transperineal needle placement procedure by increasing the precision well beyond the $5mm$ grid spacing and allowing for needle angulation and a larger workspace. Further, the needle tip can deflect within the prostate by as much as $3.2mm$ to $8.7mm$ from the template axis as measured in MRI [73]. Real-time monitoring of tip and target locations should help improve insertion accuracy. The

mechanical aspects of the robotic system are unique in that the mechanism is specifically designed for, and thus optimized to perform, prostate interventions. The work envelope, workspace, and accuracy are all tuned for the application at hand. The ultimate contribution is not the specific design presented, but the development and evaluation of techniques for designing application-specific robotic systems for operation in MRI. The sensors, actuators, controller, and software developed and evaluated are all generally applicable to MRI-guided robotic interventions.

3.2 System Architecture

The mechanism is capable of positioning the needle for treatment by ejecting radioactive seeds or diagnosis by harvesting tissue samples inside the magnet bore, under remote control of the physician without moving the patient out of the imaging space. This enables the use of real-time imaging for precise placement of needles in soft tissues. In addition to structural images, protocols for diffusion imaging and MR spectroscopy are available intraoperatively, promising enhanced visualization and targeting of pathologies. Accurate and robust needle placement devices, navigated based on such image guidance, are becoming valuable clinical tools and have clear applications in several other organ systems.

A comprehensive computer-integrated needle placement system has been designed in order to accurately target planned tissue sites by minimizing misplacement effects. The complete system incorporates a standard commercial high-field diagnostic MRI scanner

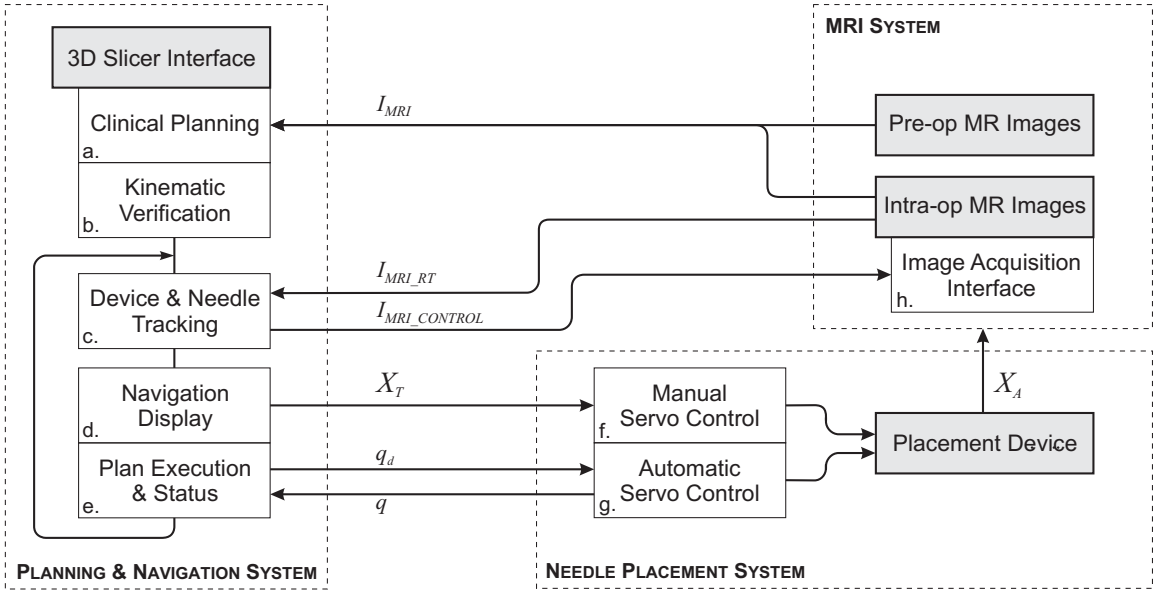

Figure 3.1: System architecture for robotic prostate interventions using the developed system.

and two major modules: (1) a visualization, planning and navigation engine and (2) a needle placement robot and controller.

The architecture of this system was first described in [93], and is presented in Fig. 3.1. Blocks **a** and **b** represent target planning on images I_{MRI}, which may include visual inspection of multi-parametric fused image datasets and applying statistical atlases, as described by Haker, *et al.* [110, 111]. The needle trajectories required to reach these desired targets are evaluated here, subject to anatomical constraints, as well as constraints of the needle placement mechanism.

Device and needle navigation are shown in blocks **c**, **d** and **e**, which are enclosed in a loop that represents device/needle positioning and sensing/localization that can iterate until the needle trajectory leads to placement, q, at the desired target, q_d. Device and needle

tracking may be image-based, as illustrated by block **c** and it's connection with block **h**. The needle and target can be tracked in real-time MR images I_{MRI_RT}, which are at positioned such that they produce images intersecting the reported needle axis, X_A.

Physical positioning including inverse kinematics and low level control occur in **f** and **g**. The manipulators kinematics are determined here, and the joint positions corresponding to the specified needle trajectory, q_d are determined based upon the 6-DOF pose of the tracking fiducial attached to the robot base, X_T.

A closed image-based servo loop that can provide the ability to compensate for the needle and tissue deflection effects described in Section 3.6. The robotic system provides remote operation of the needle while the patient is positioned within the magnet bore.

3.3 Requirements

3.3.1 Workspace Considerations

The system's principal function is accurate transperineal needle placement in the prostate for diagnosis and treatment, primarily in the form of biopsy and brachytherapy seed placement, respectively. The patient is positioned in the supine position with the legs spread and raised as shown in Fig. 3.2 (left). The patient is in a similar configuration to that of TRUS-guided brachytherapy, but the typical MRI bore's constraint ($\leq 60cm$ diameter) necessitates reducing the spread of the legs and lowering the knees into a semi-lithotomy

position. The robot operates in the confined space between the patient's legs without interference with the patient, MRI scanner components, anesthesia equipment, and auxiliary equipment present as shown in the cross-section shown in Fig. 3.2 (right).

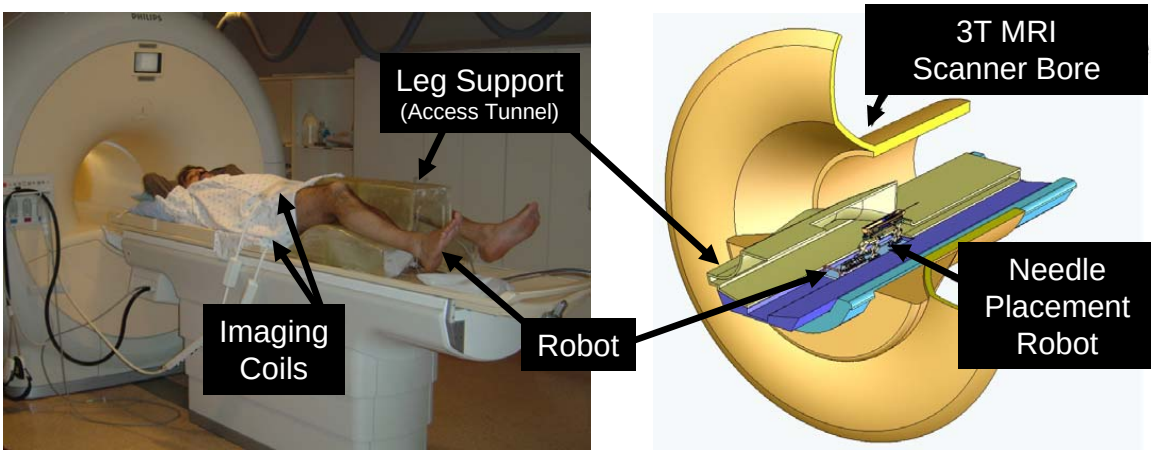

Figure 3.2: Patient positioned in the semi-lithotomy position on the leg support (left). The robot accesses the prostate through the perineal wall which rests against the superior surface of the tunnel within the leg rest (right).

The average size of the prostate is $50mm$ in the lateral direction by $35mm$ in the anterior-posterior direction by $40mm$ in length. The average prostate volume is about $35cc$; by the end of a procedure, this volume enlarge by as much as 25% due to swelling [112]. For our system, the standard $60mm \times 60mm$ perineal window of TRUS-guided brachytherapy was increased to $100mm \times 100mm$, in order to accommodate patient variability and lateral asymmetries in patient setup. In depth, the workspace extends to $150mm$ superior of the perineal surface. Direct access to all clinically relevant locations in the prostate is not always possible with a needle inserted purely along apex-base direction due to pubic arch interference (PAI) [113, 114] as shown in Fig 3.3. If more than 25% of

the prostate diameter is blocked (typically in prostates larger than $55cc$), then the patient is usually declined for implantation [112]. optimal alignment of patient and needle angle can help to mitigate PAI [115]. Needle angulation in the sagittal and coronal planes will enable procedure to be performed on many of these patients where brachytherapy is typically contraindicated due to PAI as described by Fu, *et al.* [116].

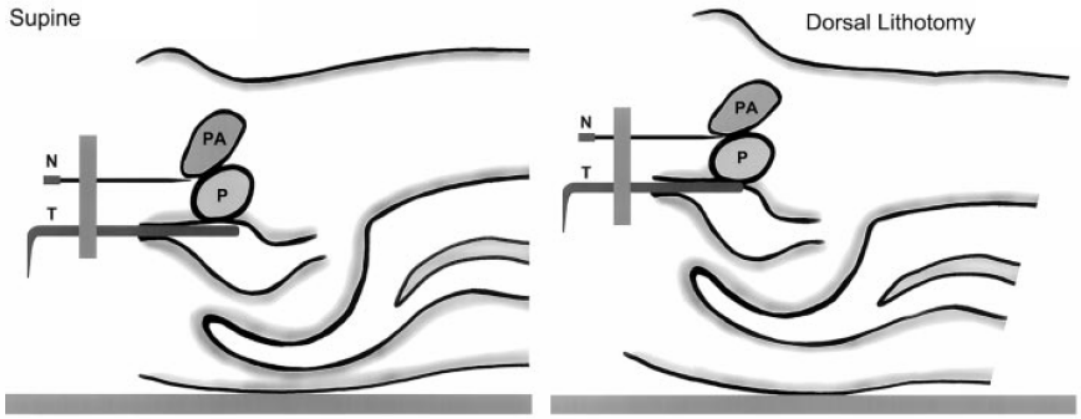

Figure 3.3: Example of pubic arch interference (PAI) from [114]. The left image shows the potential for PAI in supine position, as the legs are lifted to the lithotomy position this may be alleviated in some patients (right). Due to constraints of the MRI scanner bore, the patient will only be able to reach a semi-lithotomy position with the presented device.

3.3.2 System Requirements

The kinematic requirements for the robot are derived from the constraints describe din Section 3.3.1. A kinematic diagram of the proposed system is shown in Fig. 3.4. The robot is situated upon a manual linear slide that repeatably positions the robot in the access tunnel and allows fast removal for reloading brachytherapy needles or collecting harvested biopsy tissue. The primary actuated motions of the robot include *two prismatic motions* which

replicate the DOF of a traditional template-base approach, and *two rotational motions* for aligning the needle axis to help avoid PAI and critical structures. In addition to these base motions, application-specific motions are also required; these include needle insertion, canula retraction or biopsy gun actuation, and needle rotation.

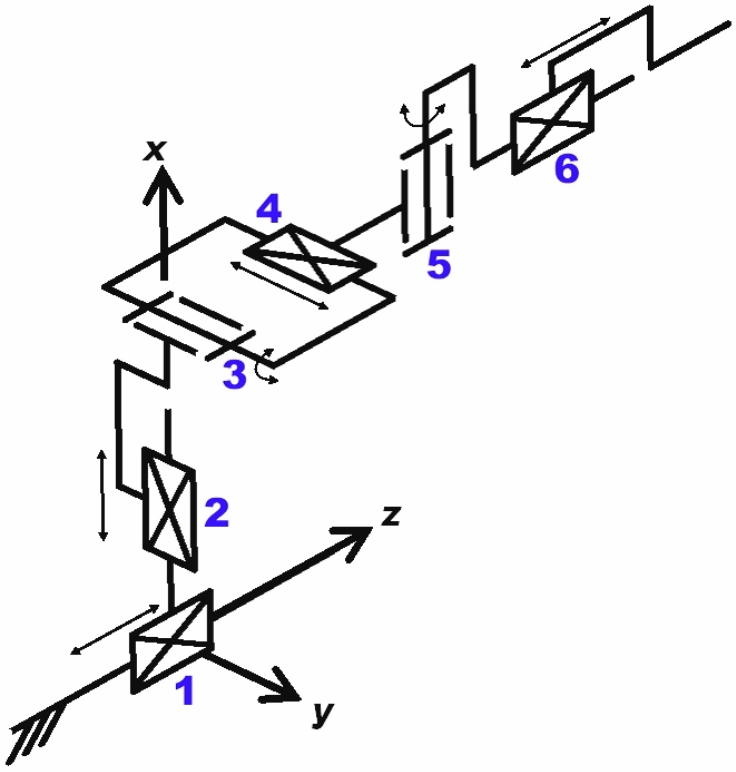

Figure 3.4: The equivalent kinematic diagram of the robot; up to six degrees of freedom are required for needle insertion procedures with this manipulator. Additional application-specific end effectors may be added to provide additional DOF.

The accuracy of the individual servo-controlled joints is targeted to be $0.1mm$, and the needle placement accuracy of the robotic system itself is targeted to be better than $1.0mm$. This target accuracy approximates the voxel size of the MR images used which represents the finest possible targeting precision. The overall system accuracy, however, is expected

Table 3.1: Kinematic Specifications for Robot

	Degree of Freedom	**Motion**	**Requirements**
1)	*Gross Axial Position*	$1m$	Manual with repeatable stop
2)	*Vertical Motion*	0 – $100mm$	Precise servo control
3)	*Elevation Angle*	$+15°$, $-0°$	Precise servo control
4)	*Horizontal Motion*	$\pm 50mm$	Precise servo control
5)	*Azimuth Angle*	$\pm 15°$	Precise servo control
6)	*Needle Insertion*	$150mm$	Manual or Automated
7)	*Cannula Retraction or Biopsy Gun Firing*	$60mm$	Manual or Automated
8)	*Needle Rotation*	$360°$	Manual or Automated

to be somewhat less when effects such as imaging resolution, needle deflection, and tissue deformation are taken into account. The MR image resolution is typically $1mm$ and the clinically significant target is typically $5mm$ in size (the precision of a traditional TRUS template).

The specifications for the requirements of each motion are shown in Table 3.1. The numbered motions in the table correspond to the labeled joints in the equivalent kinematic diagram shown in Fig. 3.4. $DOF\#1$ - 6 represent the primary robot motions and $DOF\#7$ & $\#8$ represent application-specific motions. These specifications represent a flexible system that can accommodate a large variety of patients due to the increased range or motion

and dexterity over template-based approaches. The proof-of-concept system presented here is designed to replicate the DOF of traditional TRUS-guided procedures with needle insertion only along the apex-base direction, and thus does not include angulation ($DOF\#3$ & $\#5$).

3.3.3 MRI Compatibility Requirements

Significant complexity is introduced when designing a system operating inside the bore of high-field 1.5 – $3T$ MRI scanners since traditional mechatronics materials, sensors and actuators cannot be employed. This section addresses the additional system requirements arising from compatibility with the MRI scanner.

A thorough description of the issues relating to MR Safety is described by Shellock [117]. The following definitions are according to the ASTM Standard F2052 [118]:

> **MR-Safe:** The device, when used in the MR environment, has been demonstrated to present no additional risk to the patient or other individual, but may affect the quality of the diagnostic information. The MR conditions in which the device was tested should be specified in conjunction with the term MR safe since a device that is safe under one set of conditions may not be found to be so under more extreme MR conditions.
>
> **MR-Compatible:** A device is considered MR-compatible if it is MR safe and if it, when used in the MR environment, has been demonstrated to neither significantly affect the quality of the diagnostic information nor have its operations affected by the MR device. The MR conditions in which the device was tested should be specified in conjunction with the term MR-compatible since a device that is safe under one set of conditions may not be found to be so under more extreme MR conditions.

The requirements for MR compatibility of robotic systems, as described by Chinzei [41], include:

1. MR safety

2. Maintained image quality

3. Ability to operate unaffected by the scanner's electric and magnetic fields

Ferromagnetic materials must be avoided entirely because they cause image artifacts and distortion due to field inhomogeneities, and can pose a dangerous projectile risk. Non-ferrous metals such as aluminum, brass, and titanium or high strength plastic and composite materials are therefore permissible. However, the use of any conductive materials in the vicinity of the scanner's isocenter must be limited because of the potential for induced eddy currents to disrupt the magnetic field homogeneity. To prevent or limit local heating in the proximity of the patient's body, the materials and structures used must be either non-conductive or free of loops and of carefully chosen lengths to avoid eddy currents and resonance. In this robot, all electrical and metallic components are isolated from the patient's body. The following section details material and component selection, with the consideration of MRI compatibility issues.

3.3.4 Actuator Selection

The development of MRI-compatible intervention devices is complicated by several factors: the high magnetic fields of the scanners, the requirement that such devices should not degrade the quality of the MR images, and by the confined physical space of the scanners. We first investigated commercially available actuation options. An experimental evaluation of the following three different MRI-compatible actuators was performed: the Shinsei ultrasonic motor, the Nanomotion ultrasonic motor and a pneumatic cylinder actuator.[2] We compare the effect of these actuators on the signal-to-noise ratio (SNR) of MRI images under a variety of experimental conditions. Evaluation was performed with the controller inside and outside the scanner room and with both 1.5T and 3T MR scanners. A comparison of the motors' compatibility in the different configurations is described using four popular MRI sequences for diagnostic, real-time and functional imaging.

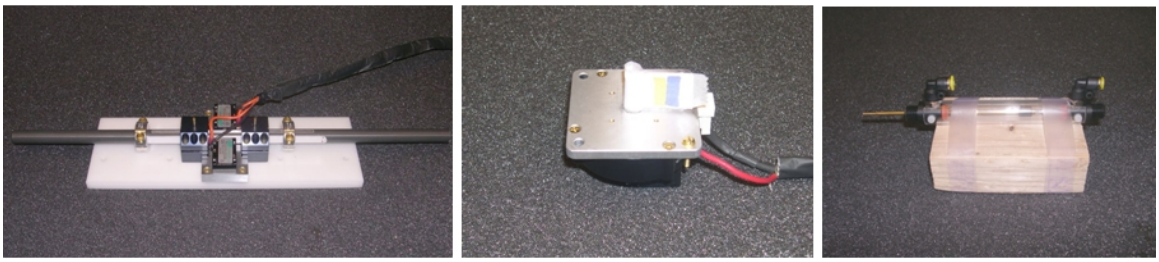

Figure 3.5: The three actuators employed in this compatibility study: Nanomotion motor (left), Shinsei motor (center), and Pneumatic cylinder (right).

[2]This section is based upon "MRI Compatibility of Robot Actuation Techniques - A Comparative Study" appearing at MICCAI, September 2008 [119]. This work was performed in collaboration with Axel Krieger, Iulian Iordachita, Louis Whitcomb, and Gabor Fichtinger

3.3.4.1 Methods

Experimental Setup

Actuation techniques employed in MR-compatible devices to date include linear piezoelectric motors, rotary piezoelectric motors, pneumatics, and hydraulics. The motors selected for our experiments were: 1) Nanomotion linear piezoelectric non-magnetic motors HR2-1-N-10 (Nanomotion Ltd., Yokneam, Israel), 2) Shinsei rotary ultrasonic non-magnetic motor USR60-E3N (Shinsei Corporation, Tokyo, Japan) and 3) Customized Airpel pneumatic cylinders (Airpot, Norwalk, CT, USA).

The *Nanomotion motor* represents the class of linear piezoelectric motors including the PI PILine (Physik Instrumente, Karlsruhe, Germany) and Piezomotor Piezoleg (Piezomotor AB, Uppsala, Sweden). Since the motors cannot be used in a stand-alone configuration, an opposing pair (maximum force $14N$) is mounted to a linear guide consisting of a $16mm$ diameter aluminum shaft supported with two DryLin R Adjustable Pillow Blocks (Igus GmbH, Koeln, Germany), as shown in Fig. 3.5 (left). During the experiments, the motors were commanded to repeatedly translate for a displacement of $5cm$ at a speed of $5cm/sec$. The *Shinsei motor* is a high torque ($0.5Nm$), rotary ultrasonic motor that has been previously employed in MR-compatible systems [41, 53]. During the experiments, the motor was configured as shown in Fig. 3.5 (center). The motor was commanded to rotate at its minimum speed of $17RPM$. The *pneumatic cylinder* employed in this study is specially designed for MR compatibility with a brass rod, graphite piston and glass cylinder as shown in Fig. 3.5 (right). The cylinders were repeatedly actuated with a pressure of $0.3bar$ and a

speed of $8cm/sec$.

Figure 3.6: General experimental setup for compatibility test in 1.5T MR scanner with Shinsei motor (left), Nanomotion motor (center) and Pneumatic cylinder (right).

The motors are controlled with the robot controller hardware described in Section 3.5.1.1. Inside an EMI shielded enclosure is an embedded Linux computer with analog and digital I/O as well as pneumatic valves and the respective amplifiers for the Nanomotion and Shinsei motors. Communication with a computer external to the scanner room is through a fiber optic Ethernet link. The robot controller configured for this experiment is shown in Fig. 3.7.

Compatibility was evaluated on a 3T Achieva scanner (Philips Medical Systems) and 1.5T Signa scanner (GE Healthcare). An $11cm$ homogeneous spherical MR calibration phantom is placed in the isocenter on top of a plastic bridge $17.5cm$ above the table surface. The motors are placed such that their center is at a horizontal distance of $30cm$ from the center of the phantom. The general experimental setup, with Shinsei motor in place, is shown in Fig. 3.6 (left). For the other actuators, the setup is shown in Fig. 3.6 (center) and (right). The distances were selected to avoid local susceptibility imaging artifact and mimic realistic actuator placement for robotic manipulators.

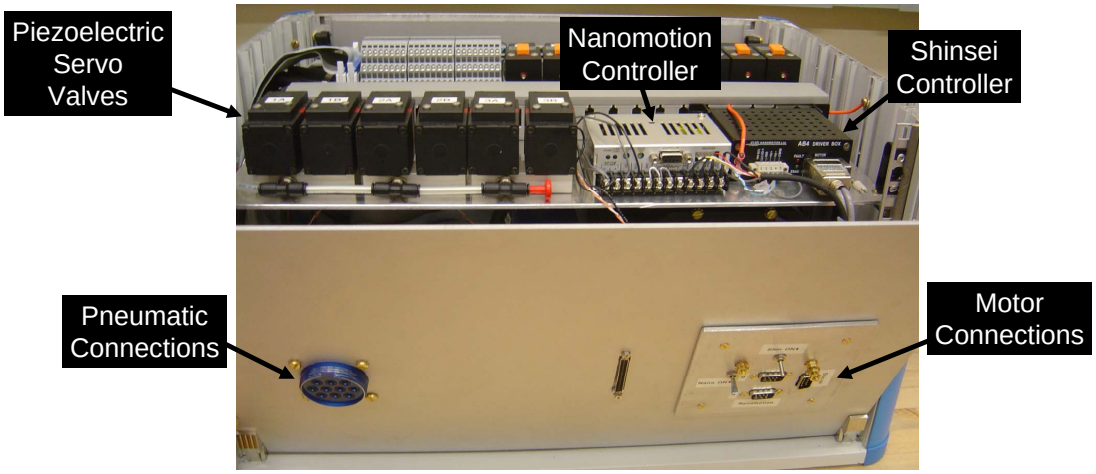

Figure 3.7: Robot controller configured for motor comparison trials. Pneumatic valves, Nanomotion amplifier, and Shinsei amplifier can be powered and controlled independently.

A typical MR suite consists of a shielded MR room, containing the MR scanner, and a control room from where the imaging is controlled. A penetration panel between the MR room and the control room allows access to the earth-grounded shield and contains wave-guides for passing cables into the MR room. In most cases the penetration panel also contains D-sub connectors with integrated low-pass filters for signal and power lines.

Two sets of experiments were performed in each of the two scanners for all three actuators. For the first set of experiments, the controller was placed *inside the scanner room*, using the fiber optic communication link through a wave-guide from the control room. The only electrical connection to the controller is a filtered DC power supply through the penetration panel. For the second set of experiments the controller was placed *inside of the control room* and the motor cables and air hoses were passed through the wave-guide. Attempts failed to run both the Nanomotion motor and the Shinsei motor by connecting

through D-sub connectors in the penetration panel, since the panel's integrated low-pass filters prevented the motors from functioning. For both motors, all cabling was enclosed in an additional shield with integrated ground strap. In the latter set, the strap was connected to ground at the penetration panel.

Each set of experiments consisted of the phantom being imaged alone (baseline) and consequently imaged in the presence of each actuator in power off configuration, power on configuration, and moving configuration.

Table 3.2: Scan Parameters for Motor Compatibility Trial

Protocol	Slice Thickness	FOV	# of Slices	TE	TR	Flip Angle	NEX	Pixel Bandwidth
1.5T GE Signa								
T1 FGE	5mm	240mm	10	2.2ms	225ms	75^o	1	977 Hz/pixel
T2 FSE	5mm	240mm	10	88ms	3000ms	90^o	1	244 Hz/pixel
FSPGR	5mm	240mm	10	4.2ms	26ms	70^o	1	244 Hz/pixel
SE EPI	5mm	240mm	10	45ms	187ms	90^o	1	1953 Hz/pixel
3T Philips Achieva								
T1 FFE	5mm	240mm	3	2.3ms	225ms	75^o	1	1075 Hz/pixel
T2 TSE	5mm	240mm	3	90ms	3000ms	90^o	1	1036 Hz/pixel
TFE/FGRE	5mm	240mm	3	10ms	26ms	70^o	1	1754 Hz/pixel
SE EPI	5mm	240mm	3	45ms	188ms	90^o	1	656 Hz/pixel

Imaging Configuration:

Four common MR sequences for diagnostic, real-time and functional imaging were selected to test the compatibility of the actuators (Table 3.2): T1 weighted fast gradient echo (T1 FGE/FFE) and T2 weighted fast spin echo (T2 FSE/TSE) sequences for diagnostic imaging, fast gradient echo (FSPGR/FGRE) sequence representing real-time imaging and spin echo-planar imaging (SE EPI) used for functional imaging.

Scanner gains, such as transmit gains, and analog and digital receiver gains, are typically set automatically during pre-scans before each image series. These gains have a significant impact on imaging. For a comparative study the gains need to be held constant for a particular imaging sequence during an experiment. The 1.5T GE scanner allows for manual setting of the gains to the consistent values, thus ensuring comparability. The 3T Philips scanner did not easily allow for manual gain setting; image series were therefore set up as a single dynamic series, with identical gains for all images within the same image sequence.

The receiving imaging coils used for the experiments were two channel medium size flex coil for the 3T scanner and four channel cardiac coil for the 1.5T scanner. Both coils consist of two panels. One panel was placed underneath the spherical phantom, the other one on top (Fig. 3.6).

Compatibility Analysis:

The MR compatibility was evaluated based upon changes in signal-to-noise ratio (SNR) as described in more detail in the MR compatibility evaluation of the robotic system in

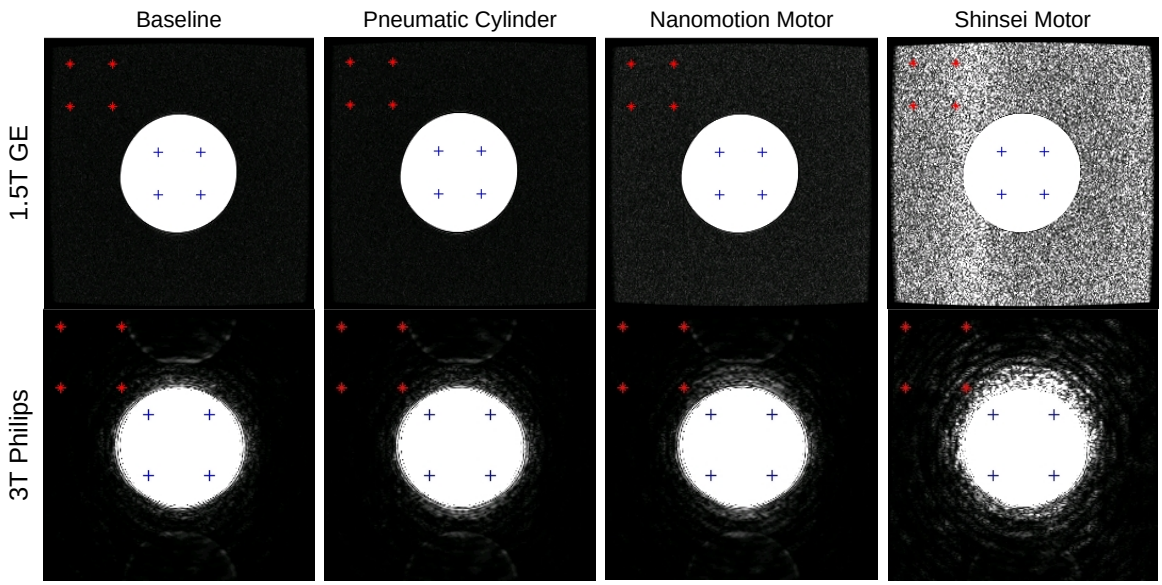

Figure 3.8: Representative FGRE images for each motor type while moving under both 1.5T and 3T imaging. The ROI used in SNR calculations is represented by '+' and the noise ROI is represented by '∗'. Window levels are identical for each row but different for the columns - thus the perceived difference in image quality.

Section 3.7.1. SNR is described by the signal intensity in the center of the homogeneous phantom divided by the noise intensity in the periphery. Signal intensity is defined as the mean pixel intensity in the region of interest (ROI). Noise intensity is defined as the root mean square (RMS) signal intensity in an ROI outside of the phantom. Although a more standard method for defining noise is to use the standard deviation, the standard deviation does not accurately represent signal degradation in noise-saturated images such as that shown in Fig. 3.8 (top, right). SNR was evaluated at three slices for 3T imaging and ten slices for 1.5T imaging for each of the four imaging sequences under each configuration.

Representative FGRE images of the phantom, acquired with actuators moving are displayed in Fig. 3.8. The top row displays images of the 1.5T scanner, the bottom row shows

images obtained with the 3T scanner. Window levels of the displayed images are identical for each row but differ for the two columns - thus the perceived difference in image quality between 1.5T and 3T. The signal ROI used in SNR calculations is denoted by '+' and the noise ROI is denoted by '*'. The location of the noise ROI has a significant impact on calculated SNR; the selected ROI in the top-left corner minimizes variance between image slices and is outside of ghosting artifacts as described by Firbank, *et al.* [120].

3.3.4.2 Results

Fig. 3.9 shows the normalized SNR results for all sequences for the 1.5T scanner, and Fig. 3.10 for the 3T scanner. Each point in the graphs represents the mean SNR over all image slices, normalized to the mean baseline SNR. The top rows show normalized SNR for the three actuators with the controller inside the scan room, the bottom rows for the controller outside the scan room.

The following are the most significant observations regarding scanner and controller configuration:

- All four imaging sequences showed very similar SNR behavior for both scanners.
- The SNR reduction due to the presence of actuators and controllers was greater on the 1.5T scanner compared to the 3T scanner.
- The control strategy of placing the controller inside the scanner room resulted in a reduction of SNR reduction compared to having the controller outside.

The following are observed results for the actuators:

- The pneumatic cylinder and controller showed no negative impact on SNR.
- The Nanomotion motor reduced SNR only moderately under 3T, especially with the controller placed in the scan room. Under 1.5T, the reduction in SNR was significant. Faster actuator speeds did not significantly change the SNR.
- The Shinsei motor caused large reduction in SNR in all "Moving" configurations. The noise increase nearly saturated the entire image with noise under 1.5T and caused significant noise ripples under 3T for the FGRE sequence (Fig. 3.8). The "Power On" configuration reduced the SNR drastically.

Off-the-shelf D-sub capacitive and ferrite filters (DGFC9MF and DGF9MF respectively from L-Com, North Andover, MA) were evaluated on the control line for both the Nanomotion and Shinsei motors with the "Controller Inside" configuration under 1.5T imaging. The filters had minimal effect on Nanomotion, but the capacitive filter did provide significant SNR recovery for the Shinsei motor (from 90% SNR reduction to 40% SNR reduction with respect to the baseline). The full results for all three motors under 3T imaging can be seen in Fig. 3.11. These results were used to determine the appropriate parameters to evaluate. In particular, note that speed and the filters evaluated in this study had minimal effect on SNR. In addition, the power state of the controller itself has minimal effect, and was this not included in the trial. This was not necessarily the case for the motor amplifiers that were switched on independent of the controller as shown in Fig. 3.7

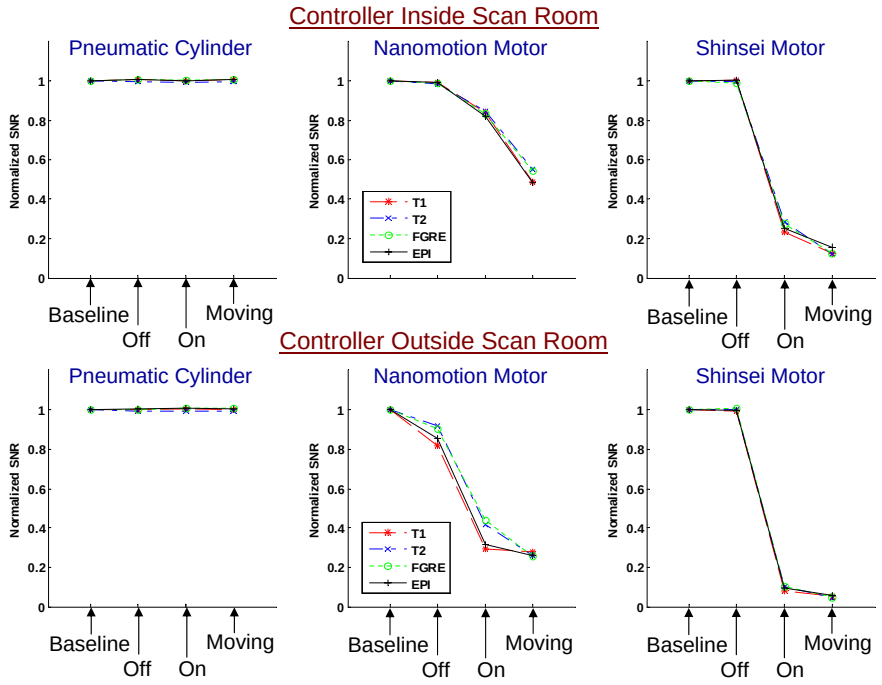

Figure 3.9: SNR results under **1.5T** imaging for each actuator in various configurations shown with the controller inside of the scanner room (top) and outside (bottom).

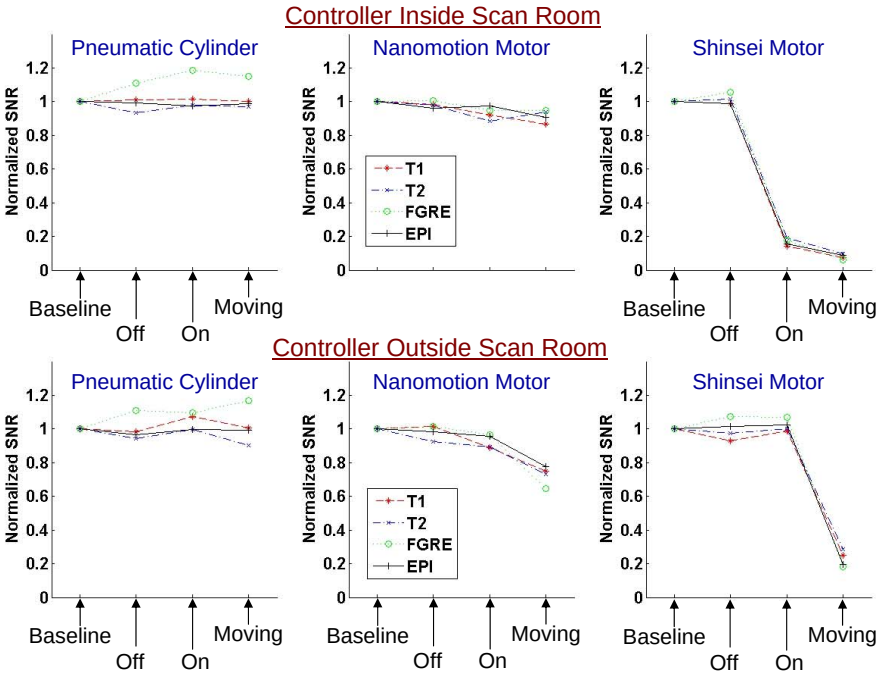

Figure 3.10: SNR results under **3T** imaging for each actuator in various configurations shown with the controller inside of the scanner room (top) and outside (bottom).

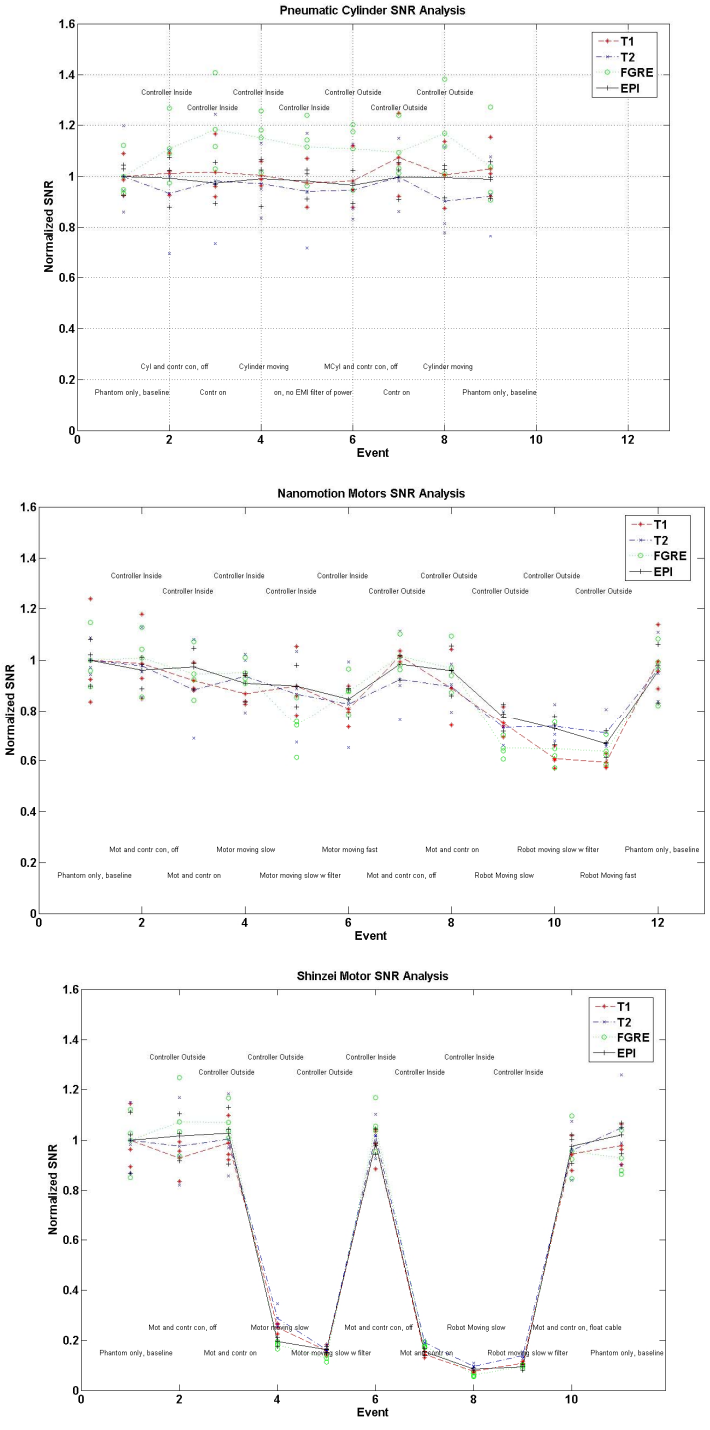

Figure 3.11: Detailed SNR results from motor comparison under 3T imaging. Motors shown in various configurations. Points represent individual image normalized SNR and corresponding lines are the average for each configuration under each scan protocol.

3.3.4.3 Discussion

The difference of SNR behavior for the two scanners cannot be attributed solely to the difference in field strength and frequency of the processing proton spins, used for imaging. There are many other factors impacting SNR loss due to mechatronic equipment. The 1.5T scanner is an older model scanner, while the 3T scanner is newly installed. Improved shielding of the scan room, better integration of the wave-guides into the penetration panel, and reduction of the size of the fringe field were implemented on the newer scanner, thus potentially reducing the noise of the actuators independent of the field strength. Moreover, the different scanners had different imaging coil availability, which strongly impacts image quality. The differences in results between scanners demonstrate the necessity for testing mechatronic equipment in each scanner used.

Due to the significant decrease in SNR, it is clear that the Shinsei motors are less suitable for providing actuation during real-time imaging. If SNR is not a critical factor, the Nanomotion motors appear to be suitable for many applications; this is especially true if extra scan time (resulting in increased SNR) is a suitable compromise for image quality. For functional and other noise-critical imaging protocols, remote actuation such as pneumatics are preferred.

The results obtained here were not specifically optimized for one scanner or configuration. It was important to show the general applicability of each actuation method in a scanner-independent manner. Further, the filters were not optimized; it has been shown by Gassert, *et al.* [121] and Curiel, *et al.* [122] that it is possible to obtain significant SNR re-

covery with the use of specially designed filters. In order to ensure scanner-independence, it is not possible to rely on the penetration panel due to variations in the built-in filtering and connector availability. Experiences demonstrate the advantages for placing the controller inside the scanner room and communication through a fiber optic medium.

In summary, the MR compatibility of Shinsei, Nanomotion and pneumatic actuators under 1.5T and 3T imaging with controllers placed both inside and outside of the scanner room was evaluated. All techniques demonstrate compatibility in the "off" configuration allowing the use of interleaved imaging and motion. The Shinsei motor did not allow for use during imaging; the Nanomotion performed with moderate SNR loss. Pneumatic actuation induced no significant degradation of image quality. SNR loss is reduced by placing an MR-compatible controller inside the scanner room. Ultimately, it is essential to evaluate the requirements (mechanical and imaging) before making an actuator selection.

3.4 Mechanical Design

3.4.1 Overview

The first embodiment of the system for initial proof-of-concept system and Phase-1 clinical trials provides the two prismatic motions in the axial (transverse) plane over the perineum ($DOF\#2$ and $DOF\#4$) and an encoded manual needle guide ($DOF\#6$) as shown in Fig. 3.4. This represents an automated high-resolution needle guide, functionally

similar to the template used in conventional brachytherapy. Two angulation DOFs have been incorporated into the design, but not yet implemented; the next version will have a 4-DOF robot base. The prototype system is shown in Fig. 3.12.

The base of the manipulator has a modular platform that allows for different end effectors to be mounted on it. The two initial end effectors will accommodate biopsy and brachytherapy needles. Both require an insertion phase; the former requires activating a single-acting button to engage the device and a safety lock, while the latter requires an additional controlled linear motion to accommodate the cannula retraction to release the brachytherapy seeds ($DOF\#7$). Rotation of the needle about its axis may be implemented to "drill" the needle in to limit deflection as described by Masamune, *et al.* [13] and Wan, *et al.* [123]. Or, it may be used to steer the needle using bevel steering techniques such as those described by Webster, *et al.* [124] or needle base manipulation as described by DiMaio, *et al.* [125].

Sterility has been taken into consideration for the design of the end effectors. In particular, the portions of the manipulator and leg rest that come in direct contact with the patient or needle will be removable and made of materials that are suitable for sterilization. The remainder of the robot will be draped. An alternative solution is to enclose the entire leg rest with the robot in a sterile drape, thus completely isolating the robot from the patient except for the needle.

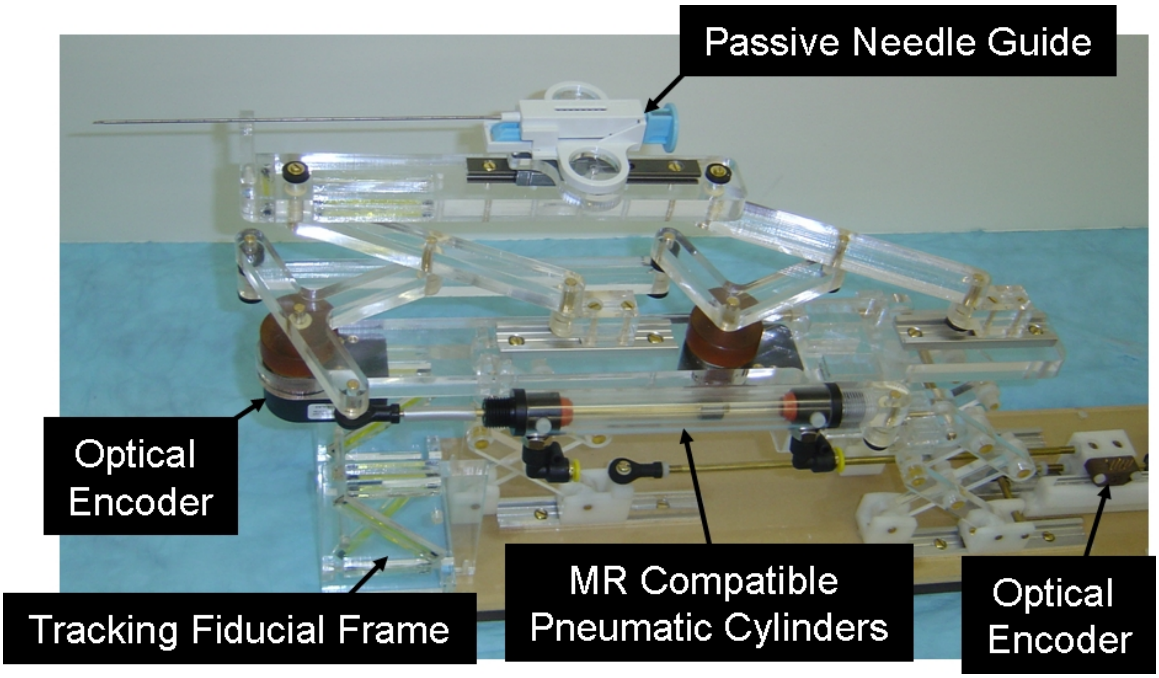

Figure 3.12: The robotic needle placement mechanism with two active DOF and passive, encoded needle insertion. Dynamic global registration is achieved with the attached stereotactic tracking fiducial frame.

3.4.2 Mechanism Design

The mechanism design is particulary important due to the very confined spaces and the lack of traditional metallic linkages. The design was developed such that the kinematics are simplified, control made less complex, motions are decoupled, actuators are appropriately aligned, and system rigidity is increased.

Based upon analysis of the workspace and the application, the following additional design requirements have been adopted:

1. Prismatic base motions should be able to be decoupled from angulation since the majority of procedures will not require the two rotational DOFs.

2. Actuator motion should be in the axial direction (aligned with the scanner's axis, B_0) to maintain a compact profile.

3. Extension in both the vertical and horizontal planes should be telescopic to minimize the working envelope.

The primary base degrees of freedom ($DOF\#2$ - $\#5$ in Table 3.1) are broken into two decoupled planar motions. Motion in the vertical plane includes $100mm$ of vertical travel, and optionally up to 15° of elevation angle. This is achieved with a modified scissor lift mechanism. By coupling two such mechanisms, as shown in Fig. 3.13, 2-DOF motion can be achieved. Stability is increased by using a pair of such mechanisms in the rear. For purely prismatic, both slides move in unison; angulation (θ) is generated by relative motions. To aid in decoupling, the actuator for the rear slide can be fixed to the carriage of the primary motion linear drive, thus allowing one actuator to be locked when angulation is unnecessary. As shown in Fig. 3.13, the push rods for the front and rear motions are coupled together to maintain only translational motion in the current prototype.

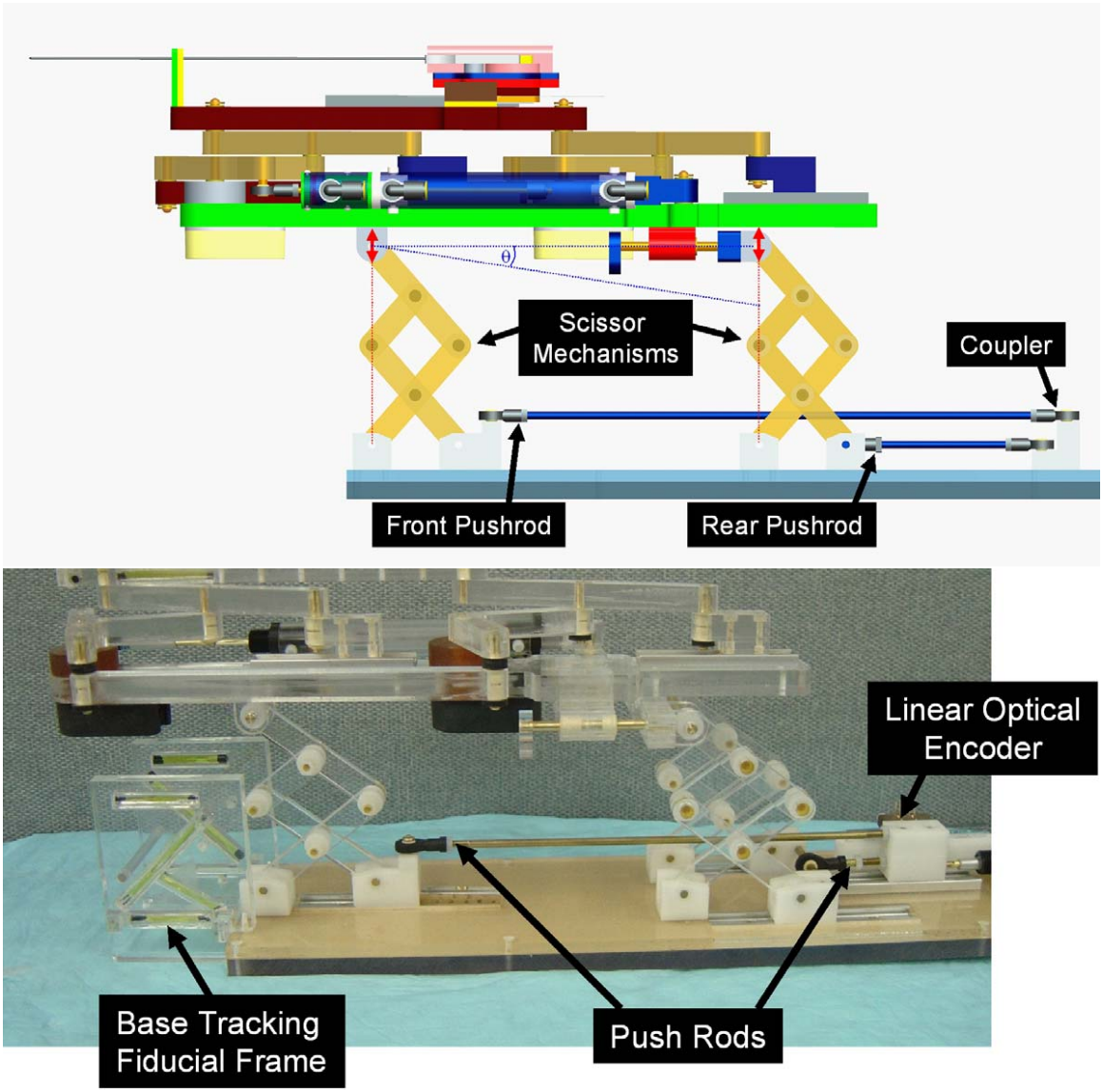

Figure 3.13: This mechanism provides for motion in the vertical plane. Coupling the forward and rear motion provides for vertical travel, independently moving the rear provides for elevation angle (θ) adjustment.

Motion in the horizontal plane is accomplished with a second planar bar mechanism. This motion is achieved by coupling two straight line motion mechanisms as shown in Fig. 3.14, generally referred to as Scott-Russell mechanisms [126]. By combining two such straight-line motions, both linear and rotational motions can be realized in the horizontal plane. The choice of this design over the use of the previously described scissor-type mechanism is that this allows for bilateral motion with respect to the nominal center position. Fig. 3.14 shows the mechanism where only translation is available; this is accomplished by linking the front and rear mechanisms with a connecting bar. A benefit of this design is that it is straightforward to add the rotational motion for future designs by replacing the rigid connecting bar (L_C) with another actuator. Due to the relative ease of manufacturing, the current iteration of the system is made primarily out of acrylic. In future design iterations, the links will be made out of high strength, dimensionally stable, highly electrically insulating and sterilizable plastic (*e.g.* Ultem or PEEK).

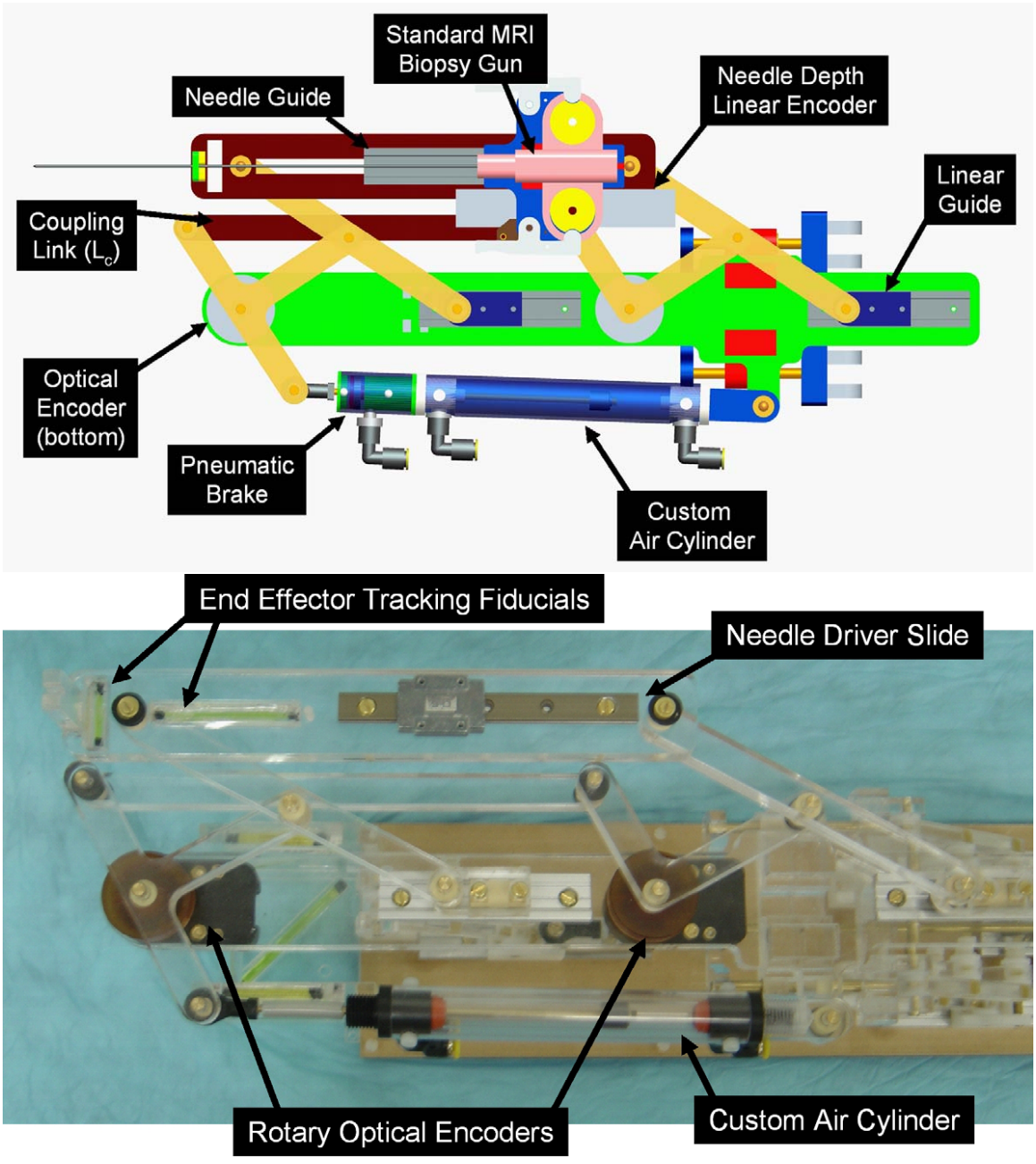

Figure 3.14: This mechanism provides for motion in the horizontal plane. The design shown provides prismatic motion only; rotation can be enabled by actuating rear motion independently by replacing coupling link (L_C) with a second actuator. The modular, encoded needle guide senses the depth during manual needle insertion and can be replaced with different end effectors for other procedures.

3.4.3 Actuator Design

The MRI environment places severe restrictions on the choice of sensors and actuators. Many mechatronic systems use electro-dynamic actuation, however, the nature of typical electric motor precludes its use in high-field magnetic environments. Therefore, it is necessary to either use actuators that are compatible with the MR environment, or to use a transmission to mechanically couple the manipulator in close proximity to the scanner to standard actuators situated outside the high field.

MR-compatible actuators such as piezoceramic motors have been evaluated by [54], [41] and [53]; however, these are prone to introducing noise into MR imaging when active and therefore negatively impacting image quality as shown in Section 3.3.4. Dielectric elastomer actuators (DEAs) have been investigated, but the lack of stiffness, precision, and manufacturability limit their use at this point [55]. Mechanical coupling can take the form of flexible driveshafts [43], push-pull cables, or hydraulic (or pneumatic) couplings [50].

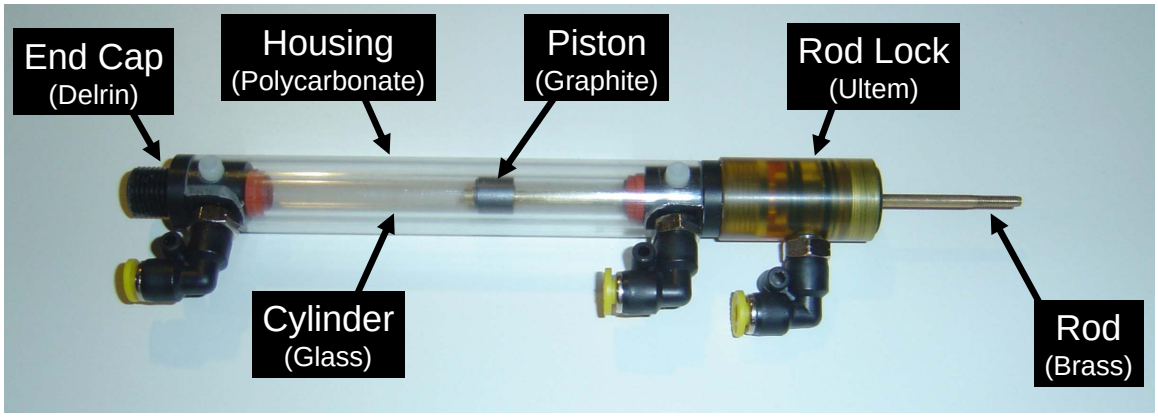

Figure 3.15: Custom MR-compatible, low friction pneumatic cylinder with developed compact rod lock brake mechanism.

From the evaluation presented in Section 3.3.4, pneumatic cylinders are the actuator of choice for this robot. Accurate servo control of pneumatic actuators using sliding mode control (SMC) with submillimeter tracking accuracy and $0.01mm$ steady-state error (SSE) has been reported by Ning, *at al.* [127]. Although pneumatic actuation seems ideal for MRI, most standard pneumatic cylinders are not suitable for use in MRI. Custom MR-compatible pneumatic cylinders have been developed for use with this robot (Fig. 3.15). The cylinders are based upon Airpel $9.3mm$ bore cylinders (E9 Anti-stiction Air Cylinder, Airpot Corp., Norwalk, CT). These cylinders were chosen because the cylinder bore is made of glass and the piston and seals are made of graphite. This design has two main benefits; the primary components are suitable for MRI and they inherently have very low friction (as low as $0.01N$). The cylinders were developed in collaboration with the manufacturer, and are entirely nonmetallic except for the brass shaft. The cylinders can handle up to $100psi$ ($6.9bar$) and therefore can apply forces up to $46.8N$.

In addition to moving the robot, it is important to be able to lock it in position to provide a stable needle insertion platform. Pneumatically operated, MR-compatible brakes have been developed for this purpose and are shown attached to the cylinder in Fig. 3.15. The brakes are compact units that attach to the ends of the previously described cylinders as shown in Fig. 3.14 (top) and clamp down on the rod. The design is such that the fail-safe state is locked and applied air pressure releases a spring-loaded collet to enable motion. The brakes are disabled when the axis is aligned and applied when the needle is to be inserted or an emergency situation arises.

Proportional pressure regulators were the valve of choice for this robot because they allow for direct control of air pressure, thus the force applied by the pneumatic cylinder. This is an advantage because it aids in controller design and also has the inherent safety of being able to limit applied pressure to a prescribed amount. Most pneumatic valves are operated by a solenoid coil; unfortunately, as with electric motors, the very nature of a solenoid coil is a contraindication for its use in an MR environment.

With pneumatic control, it is essential to limit the distance from the valve to the cylinder on the robot; thus it is important to use valves that are safe and effective in the MR environment. By placing the controller in the scanner room near the foot of the bed, air tubing lengths are reduced to $5m$. The robot controller uses piezoelectrically actuated proportional pressure (PRE-U Piezo Valve, Hoerbiger-Origa GmbH, Filderstadt, Germany), thus permitting their use near MRI. A pair of these valves provide a differential pressure of $\pm 100psi$ on the cylinder piston for each actuated axis. The valves can seen in the controller in Fig. 3.24.

A further benefit of piezoelectrically actuated valves is the rapid response time ($4ms$). Thus, by using piezoelectric valves the robot's bandwidth can be increase significantly by limiting tubing lengths and increasing controller update rate. Fig. 3.16 shows the response and rise time as a function of hose length. The dynamic response for the valve can be seen in Fig. 3.17, where pressure sensors are placed at the valve exit and the pneumatic cylinder input. Note the time delay from zero pressure and the overshoot in pressure as measured at the robot at the end of a $15ft$ long, $\varnothing 4mm$ air supply hose.

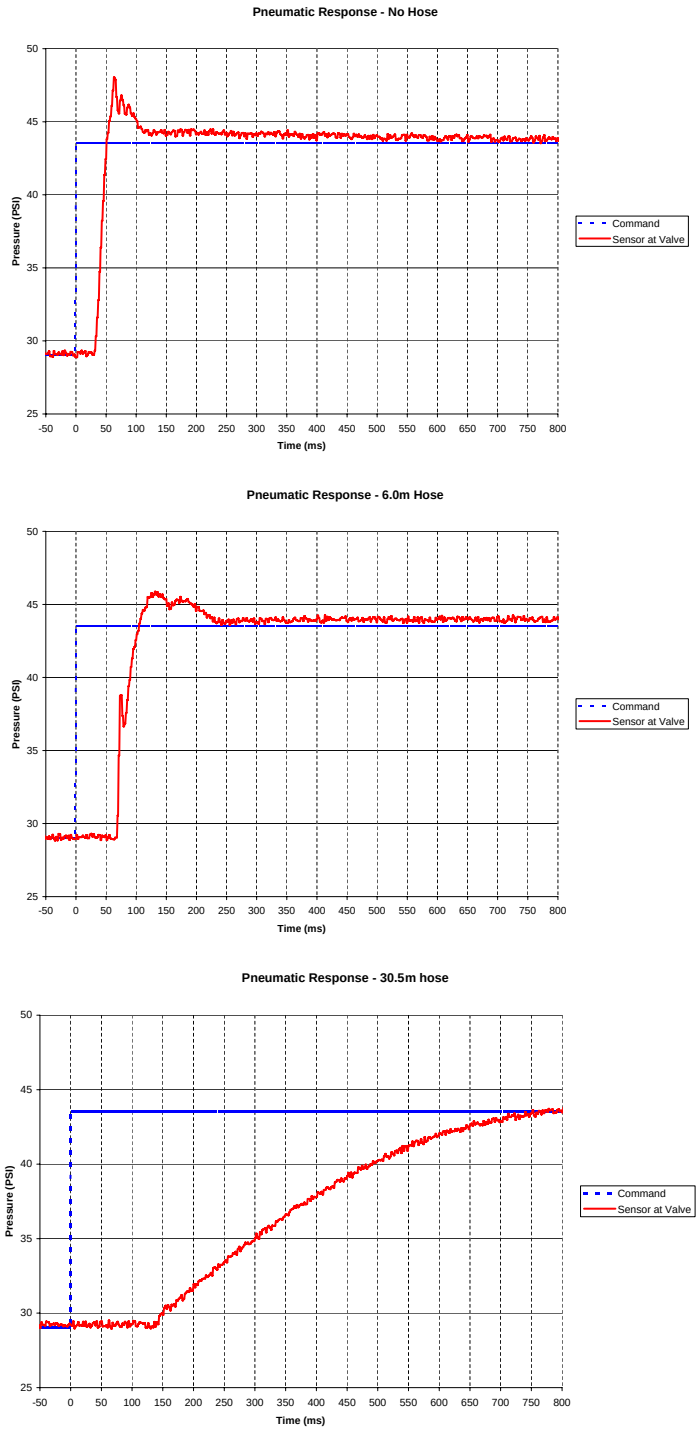

Figure 3.16: Air pressure step responses for $\varnothing 4mm$ air supply hose with lengths of: $0ft/0m$ (top), $20ft/6.0m$ (center), and $100ft/30.5m$ (bottom).

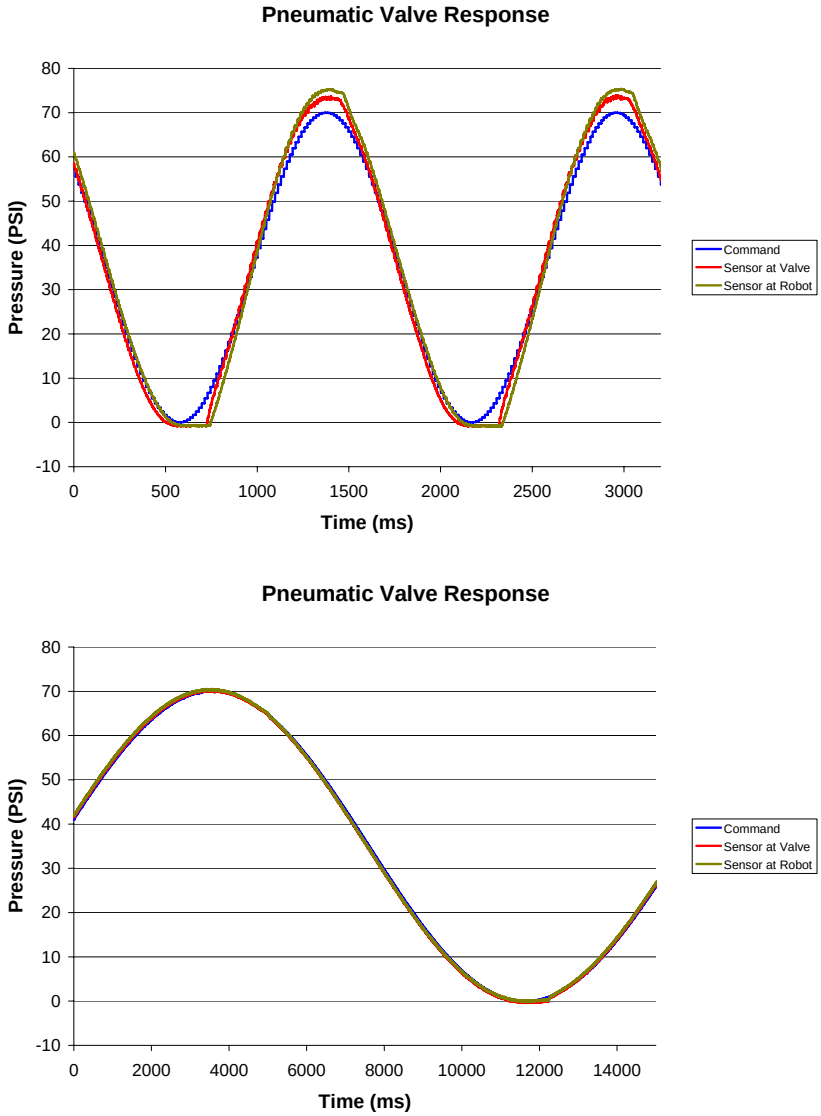

Figure 3.17: Dynamic response of valve pressure at both ends of $15ft/4.6m$ long, $\varnothing 4mm$ air supply hose. Shown for sinusoidal inputs with of periods: $T_1 = 1.5sec$ (top) and $T_2 = 10.0sec$ (bottom).

3.4.4 Position Sensing

Traditional position sensing techniques that are generally applicable to pneumatic cylinders include: linear potentiometers, linear variable differential transformers (LVDT), capacitive sensors, ultrasonic sensors, magnetic sensors, laser sensors, optical encoders, and cameras (machine vision). Most of these sensing modalities are not practical for use in an MR environment. However, there are two methods that do appear to have potential:

- Linear optical encoders
- Direct MR image guidance

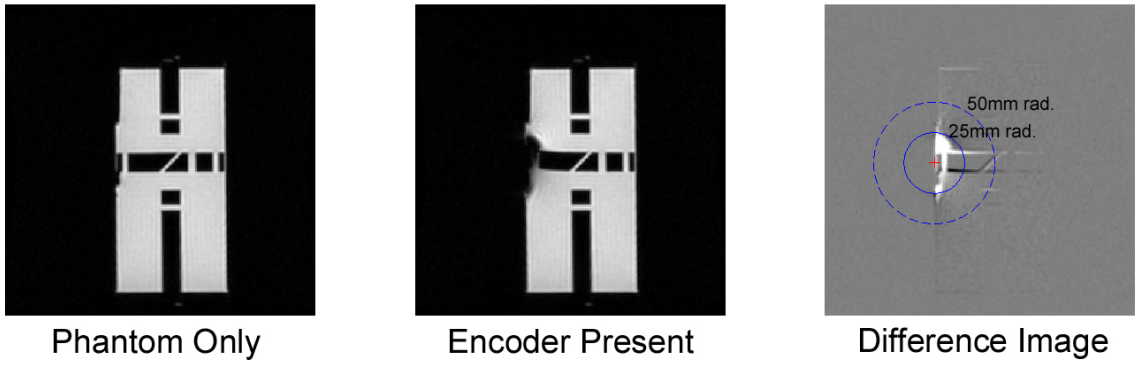

Figure 3.18: MR compatibility evaluation of optical encoder in a 1.5T scanner. A standard GE phantom (left), the phantom with the encoder placed directly above at the isocenter (center), and the difference image (right).

Standard optical encoders (EM1-1250 linear and E5D-1250 rotary encoder modules with PC5 differential line drivers - US Digital, Vancouver, Washington) are used in this robotic system. The encoders interface with the system as described in Section 3.5.1.1. The encoders are placed directly on the joints of the robot and reside in the scanner bore.

The differential signal driver sits on the encoder module, and the signals are transmitted through shielded, twisted pairs cables to the encoder interface. The encoder interface is a shielded circuit board that is fixed near the robot base and takes the individual encoder inputs and routes them through a 68-conductor shielded twisted pair cable that connects to the front face of the robot control enclosure. Inside of the shielded controller enclosure are differential line receiver modules that translate the signals back to standard TTL levels and feeds them into an FPGA module. The FPGA provides for counting and interfacing with the controller computer as described later in Section 3.5.1.1. The encoders have been incorporated into the robotic device and perform without any evidence of stray or missed counts.

The encoders have been have been thoroughly tested in a 3T MRI scanner for functionality and induced effects in the form of imaging artifacts as described in [93] and later in Section 3.7.1. The imaging artifact of the encoder when placed at the isocenter is confined locally to within 2 - $5cm$ as shown in Fig. 3.18. This is sufficient because the robot is designed to distance the sensors from the prostate imaging volume. In the robot, the encoders are placed at a distance from the isocenter that avoid these susceptibility artifacts.

Direct MR image guidance is described in Section 3.6. It may be used for high-level visual servo control and image-based verification of the procedure, but the sample rate is not fast enough to allow for closed-loop servo control of the joints.

3.4.5 Kinematics

3.4.5.1 Vertical Motion Mechanism

The schematic figure describing the kinematics for motion in the vertical plane is shown in Fig. 3.19. The vertical motion is provided by actuation of the scissor mechanism. A linear motion in the Superior-Inferior (SI) direction produces a motion in the Anterior-Posterior (AP) direction. The equation of motion for this axis is:

$$y = 2\left(\sqrt{2d_1 l - d_1^2}\right). \tag{3.1}$$

Where:

y is the end effector position in the vertical direction,

d_1 is the cylinder displacement, and

l is the link length as shown in Fig. 3.19.

If the front and rear scissor mechanisms are moved independently, a variable elevation angle, θ, is produced. This rotation can be calculated as:

$$\theta = atan\left(\frac{y_f - y_r}{D}\right) \tag{3.2}$$

$$= atan\left(\frac{2\left(\sqrt{2d_{1f}l - d_{1f}^2} - \sqrt{2d_{1r}l - d_{1r}^2}\right)}{D}\right) \tag{3.3}$$

Where:

y_f and y_r are the heights of the front and rear mechanisms, respectively,

d_{1f} and d_{1r} are the cylinder displacements for the front and rear mechanisms, respectively, and

D is distance between the front and rear mechanisms as shown in Fig. 3.19.

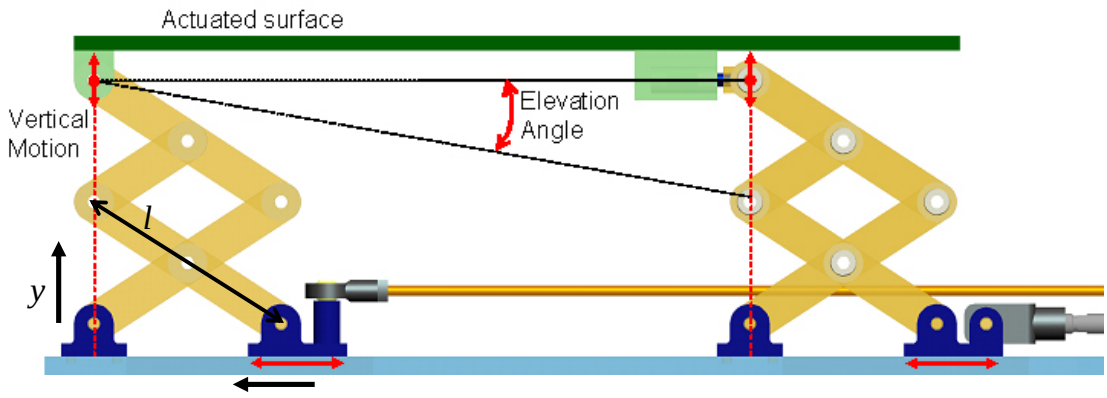

Figure 3.19: Schematic of robot kinematics for the vertical motion.

Due to the nonlinearity of the mechanism structure, the system behavior is very different for varying regions of operation. Thus, it is critical to optimize the link lengths to achieve the desired behavior in the required operating range. Fig. 3.20 shows the sensitivity of the end effector motion to actuator displacement. The requirements are $60-100mm$ of vertical motion while maintaining a minimal offset from the table at the lowest position. The solid line represents a link length of $l = 68mm$ which was determined to be the optimal tradeoff between range of motion and offset. Increasing the link length increases the region with minimal $\frac{dy(d_1)}{d_1}$, thus requiring lower and more consistent control effort, but also pushes the operating range out of the usable limits without incorporating a custom scanner table carriage.

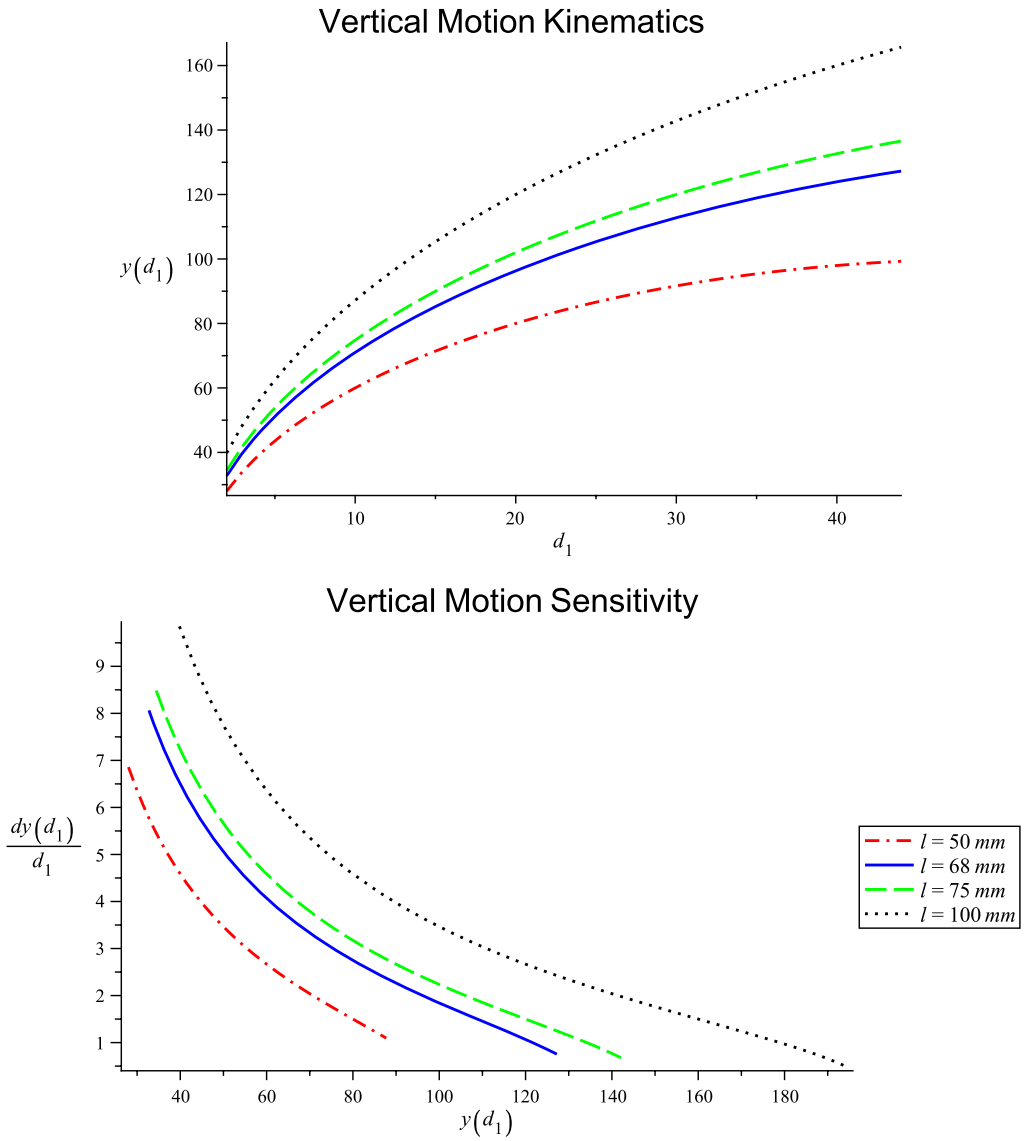

Figure 3.20: Vertical motion sensitivity to actuator displacement as a function of end effector position for various link lengths (l). d_1 represents actuator displacement, $y(d_1)$ is the end effector position, and $\frac{dy(d_1)}{d_1}$ is the relative change in end effector motion plotted with respect to absolute end effector position.

3.4.5.2 Horizontal Motion Mechanism

The schematic describing the kinematics for motion in the horizontal plan is in Fig. 3.21. The equation of motion with respect to the rotation angle is described in Equation 3.4. Equation 3.5 shows the relationship between actuator displacement and end effector position.

$$x = 2l \sin\theta. \tag{3.4}$$

$$x = \frac{\left(2\,a^2L + 2\,L^2d_2 - L{d_2}^2 - \sqrt{a^2\left(4\,a^2L^2 - 4\,{d_2}^2L^2 + 4\,a^2{d_2}^2 - 8\,a^2dd\,L - {d_2}^4 + 4\,{d_2}^3L\right)}\right)l}{2a\left(L^2 + a^2\right)} \tag{3.5}$$

Where:

x is the end effector position in the horizontal direction,

d_2 is the cylinder displacement, and

L is the distance between the cylinder's base and rod end at the zero position,

l is the link length as shown in Fig. 3.21, and

a is the distance from the pivot that the cylinder acts on the mechanism.

If the front and rear mechanisms are moved independently, a variable azimuth angle, α, is produced. This rotation can be calculated as:

$$\alpha = atan\left(\frac{x_f - x_r}{D}\right) \tag{3.6}$$

$$= atan\left(\frac{2l\left[sin(\theta_f) - sin(\theta_r)\right]}{D}\right) \tag{3.7}$$

Where:

x_f and x_r are the heights of the front and rear mechanisms, respectively,

θ_f and θ_r are the rotation angles of the front and rear mechanisms, respectively, and

D is distance between the front and rear mechanisms as shown in Fig. 3.21.

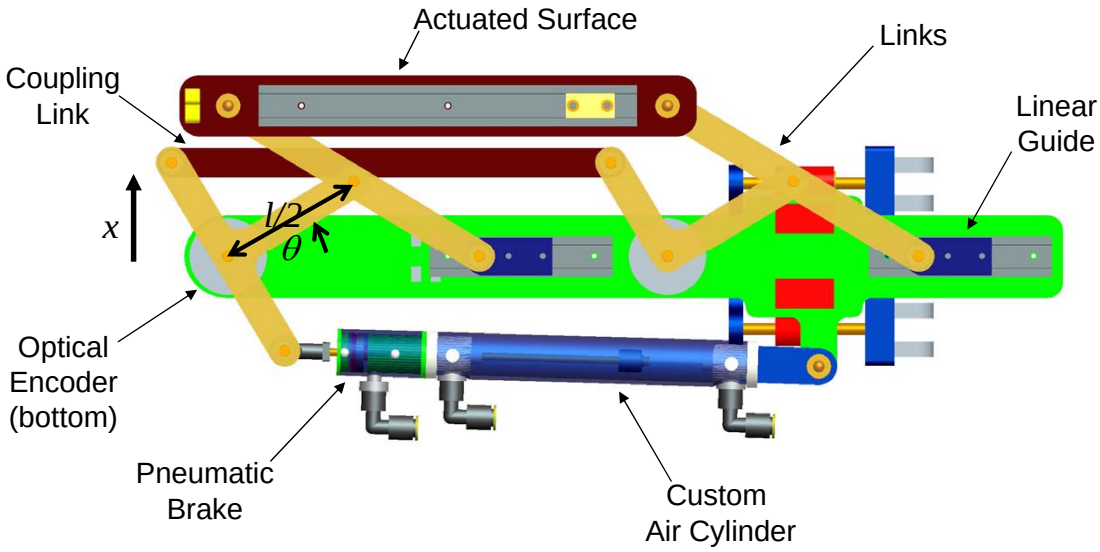

Figure 3.21: Schematic of robot kinematics for the horizontal motion.

As with the vertical motion mechanism, the horizontal motion is not linearly related to the actuator displacement. However, as seen in Fig 3.22, the response is much more linear is the required range of motion. Therefore, the optimal link length is the one that allows $\pm 50mm$ of motion in the linear range. The solid line represents a link length of $l = 100mm$ which provide an almost constant $2:1$ input to output relationship, $\frac{dx(d_2)}{d_2}$.

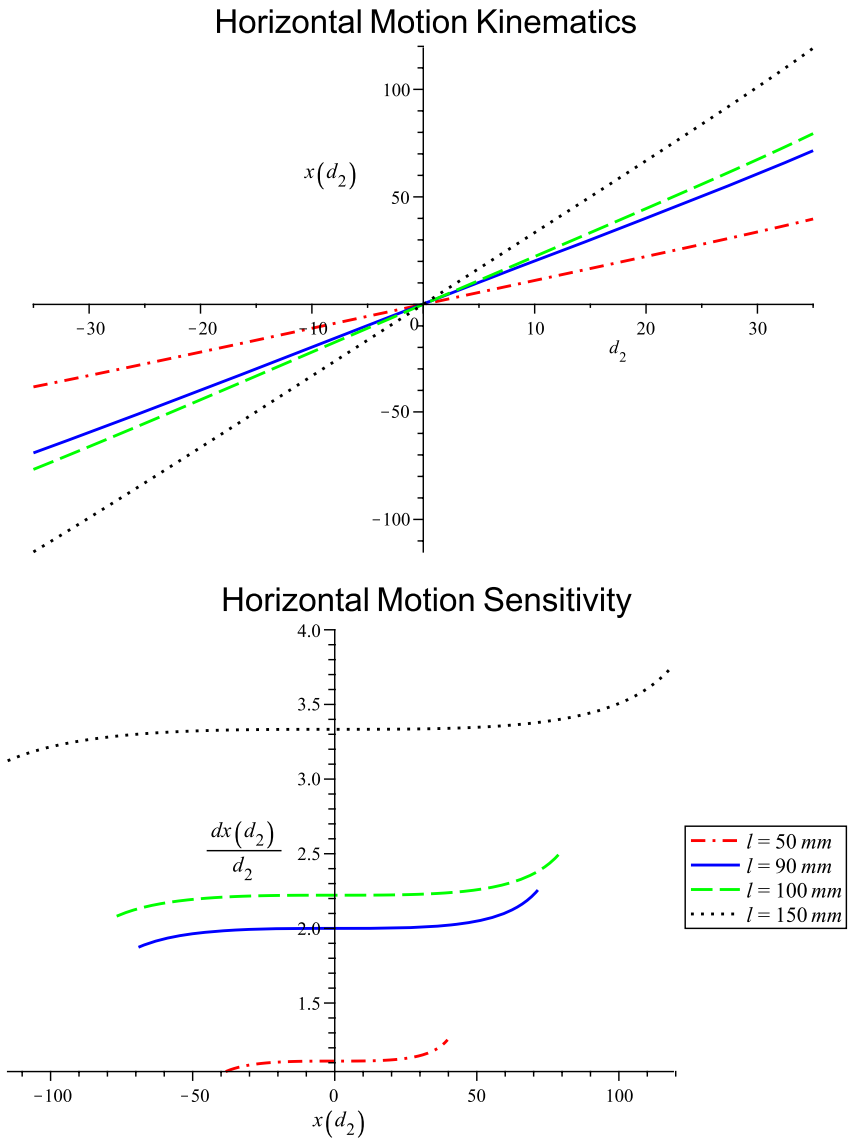

Figure 3.22: Horizontal motion sensitivity to actuator displacement as a function of end effector position for various link lengths (l). d_2 represents actuator displacement, $x(d_2)$ is the end effector position, and $\frac{dx(d_2)}{d_2}$ is the relative change in end effector motion plotted with respect to absolute end effector position.

3.4.6 Modeling

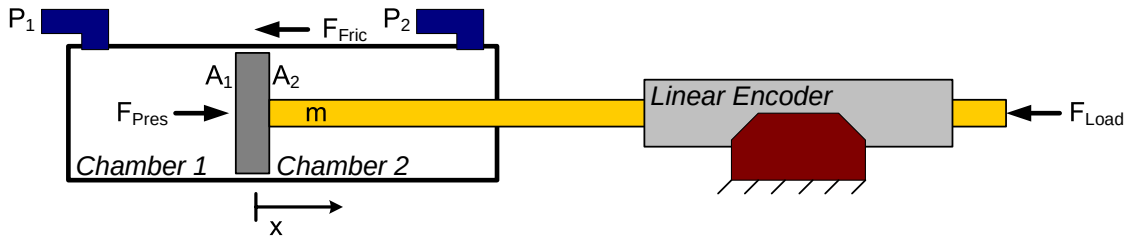

Figure 3.23: Schematic of the pneumatic cylinder.

The dynamics of the pneumatic cylinder shown in Fig. 3.23 are shown below. This represents the cylinder itself, as used in the test fixture.

$$F_{Pres} - F_{Ext} = m\ddot{x} \tag{3.8}$$

Where:

$$\begin{aligned} F_{Pres} &= P_1 A_1 - P_2 A_2 \\ F_{Ext} &= F_{Fric} + F_{Load} \\ F_{Fric} &= \mu_v \dot{x} + \mu_c sign(\dot{x}) \end{aligned}$$

And, μ_v is the coefficient of viscous friction, μ_c is the coefficient of static friction, and m is the moving mass.

The dynamics can be described as:

$$\ddot{x} = \frac{1}{m}\left[P_1 A_1 - P_2 A_2 - \mu_v \dot{x} - \mu_c sign(\dot{x}) - F_{Load}\right] \tag{3.9}$$

This can be rewritten as:

$$\ddot{x} + \frac{1}{m}\mu_v\dot{x} + \frac{1}{m}\mu_c sign(\dot{x}) + \frac{1}{m}F_{Load} - \frac{1}{m}F_{Pres} = 0 \tag{3.10}$$

By neglecting friction and external load, the equation can be written as:

$$\ddot{x} + \frac{1}{m}\mu_v\dot{x} - \frac{1}{m}u = 0 \tag{3.11}$$

Where u is the control input, F_{Pres}. By modeling the control input as a simple proportional controller, $u = kx$. k is the effective spring constant of the system holding it at the set point $x = 0$.

The equation can then be written as a standard second order system:

$$\ddot{x} + b\dot{x} + cx = 0 \tag{3.12}$$

Where:

$$\begin{aligned} b &= 2\zeta\omega_n \\ &= \frac{1}{m}\mu_v \\ c &= \omega_n^2 \\ &= -\frac{1}{m}kx \end{aligned}$$

The natural frequency of the system is then: $\omega_n = \sqrt{\frac{k}{m}}$. And, the damping coefficient is: $\zeta = \frac{\mu_v}{2\sqrt{mk}}$. Therefore, the damped natural frequency of the system is:

$$\omega_d = \sqrt{\frac{k}{m} - \frac{\mu_v^2}{4m^2}} \tag{3.13}$$

The significance of this point is that the damping of the system has a significant effect on the controllability. The pneumatic valves have an inherent delay as described in Section 3.4.3. There are three ways to increase the stability of the controlled system: decrease the control input delay, decrease the magnitude of the control input kx, or decrease the natural frequency ω_d. Increasing valve or air propagation delay is not feasible and the control input can not be significantly reduced to overcome static friction. Therefore, the goal is to decrease ω_d.

Both the viscous friction coefficient, μ_v, and the moving mass, m, are inversely proportional to the frequency. As described later in when the control system is applied to the pneumatic cylinder in Section 3.5.2.2, the damping and mass have an enormous impact on controller stability. Thus, we can make the system easier to control by mechanically increasing the system damping and moving mass. This is evidenced by the results showing very high tracking accuracy when an external damper is applied to the system.

3.5 Controller Design

3.5.1 Physical Controller Design

3.5.1.1 Hardware Design

MRI is very sensitive to electrical signals passing in and out of the scanner room. Electrical signals passing through the patch panel or wave guide can act as antennas, bringing

stray RF noise into the scanner room. As determined from the experiments described in Section 3.3.4, and to minimize the distance between the valves and the robot, the robot controller is placed inside of the scanner room with no external electrical connections.

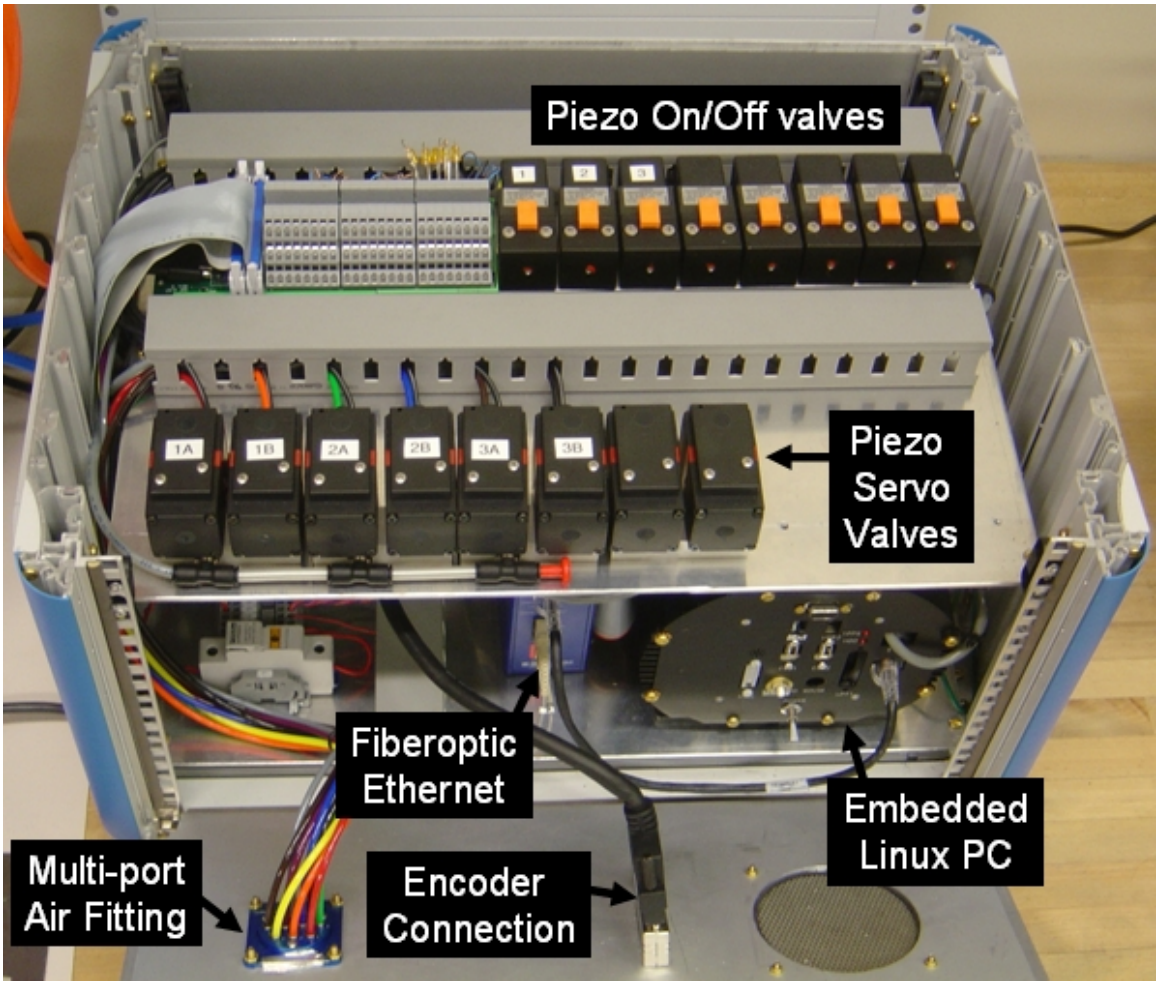

Figure 3.24: The controller contains the embedded Linux PC on a PC-104 stack providing low-level servo control, the piezoelectric valves and the fiber optic ethernet converter. The EMI shielded enclosure is placed inside the scanner room near the foot of the bed. Connections to the robot include the multi-tube air hose and the encoder cable; connection to the planning workstation is via fiber optic ethernet.

The controller comprises an electro-magnetic interference (EMI) shielded enclosure that sits at the foot of the scanner bed as shown in Fig. 3.43; the controller has proved to be

able to operate $3m$ from the edge of 1.5T and 3T scanner bores. A view of the controller enclosure with the cover removed is shown in Fig. 3.24.

Inside of the enclosure is an embedded computer as shown in Fg. 3.25. The controller computer system is a 4"x4" PC-104 form factor and includes: Pentium Mobile 1.6MHz CPU, 1GB RAM, 4GB compact flash system drive (Cheetah EPM-32c, Versalogic Corp., Eugene, OR), power regulation and field programmable gate array (FPGA) with custom daughtercard for digital inputs and outputs for encoder inputs, brake valve control, and general I/O (HE104+DX and FPGA-104 respectively, Tri-M Systems, Port Coquitlam, BC, Canada), and analog outputs for valve control and analog inputs for pressure and force sensor input (RMM-1612 and DMM-16-AT respectively, Diamond Systems, Mountain View, CA). The controller configuration, and in particular the FPGA interface and low level PC software, relates to that described by Kapoor, *et al.* [128].

Also in the enclosure are the piezoelectric servo valves, piezoelectric brake valves and pressure sensors. The distance between the servo valves and the robot is minimized to less than $5m$, thus maximizing the bandwidth of the pneumatic actuators as described in Section 3.4.3.

Control software on the embedded PC, provides for low-level joint control and an interface to interactive scripting and higher level trajectory planning. Communication between the low-level control PC and the planning and control workstation sitting in the MR console room is through a 100-FX ($100Mbps$) fiber optic Ethernet connection (B&B Electronics, EIR-M-ST Industrial Media Converter, Ottawa, IL). In the prototype system, power is sup-

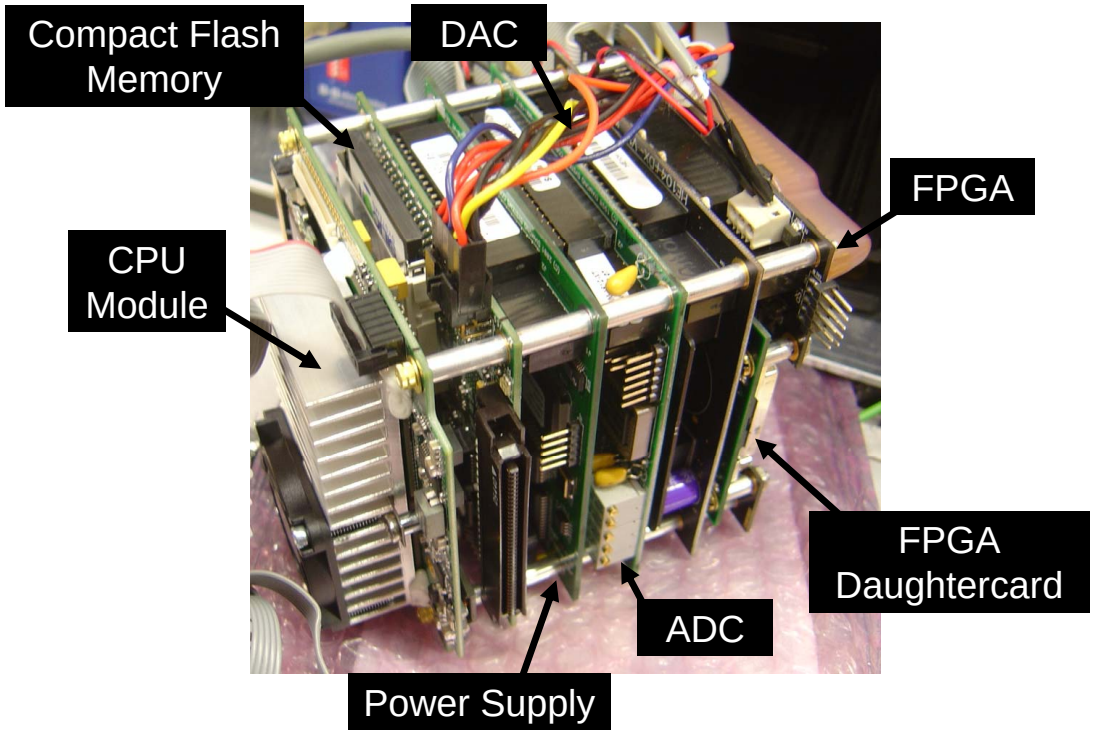

Figure 3.25: PC-104 form factor (4"x4") embedded computer configuration. Included modules: Pentium Mobile 1.6MHz CPU, 1GB RAM, 4GB compact flash system drive, power regulation, analog outputs, analog inputs, and an FPGA with custom daughtercard for digital inputs and outputs.

plied to the controller from a filtered (L-Com DGFC9MF Capacitive EMC Filter, North Andover, MA) DC power supply that passes through the patch panel. No other electrical connections pass out of the scanner room, thus significantly limiting MR imaging interference. Future iterations will use a commercially available, MR-compatible linear DC power supply that resides inside the scanner room; this completely eliminates any electrical connection passing out of the scanner room (only fiber optic communications and air supply).

3.5.1.2 Software Design

The software implemented on the embedded Linux computer described in Section 3.5.1.1 is based upon the CISST open source software library (CISST Software Package, http://www.cisst.org/resources/software). The implemented software platform includes: Python interactive scripting environment, graphical user interface, network interface, and controller implementation.

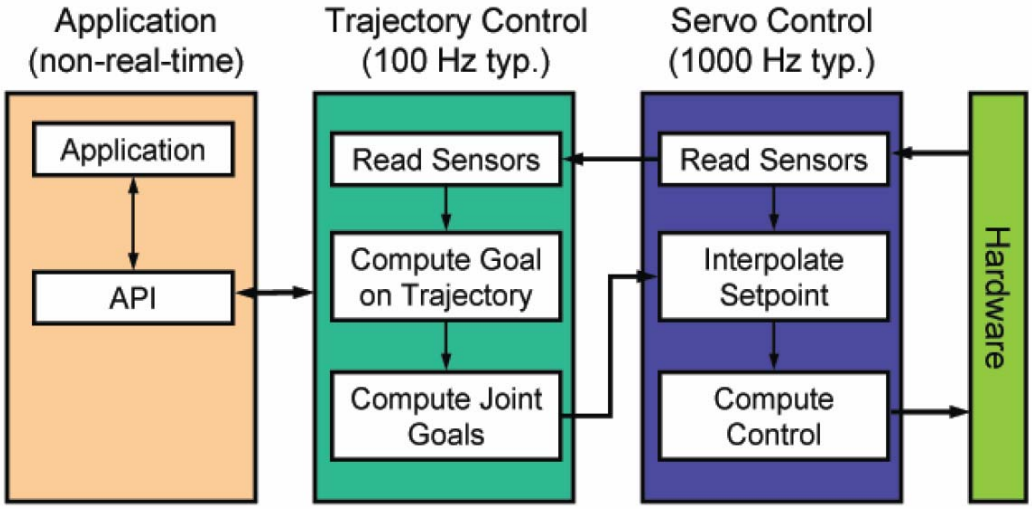

Figure 3.26: CISST software library robot control architecture from [129].

The description of the software components and framework of the robot control elements of the CISST library are described by Kapoor, Deguet and Kazanzides [129]. Fig. 3.26 shows the architecture adopted for this system. The block shown in the figure correspond to our system as follows:

- The *Application* block contains the user interface including a traditional GUI and

Python scripting.

- The *Trajectory Control* block contains the communications interface with the planning software and the forward and inverse kinematics modules.

- The *Servo Control* block contains the implementation of the servo controller described in Section 3.5.2.

- The *Hardware* block contains an application programming interface (API) that enables use of the physical hardware.

3.5.2 Control System

Pneumatic cylinders have long been used for automation in the traditional bi-stable configuration. But, precise servo control is a challenge because of the difficulty in system modeling due in part to the inherent nonlinearities of pneumatic systems. The modeling uncertainty necessitates robust control methodologies. A model of a reduced order sliding mode controller (SMC) for pneumatic actuators is published by Paul, *et al.* in 1994 [130]. This paper presented a simulation of the SMC based upon on-off solenoid valves and neglected stiction in the plant model. Acarman, *et al.* present a sliding mode controller with an observer for estimating position and chamber pressures [131]. Korondi and Gyeviki present an SMC that switches between two sliding modes; a steep sliding line ensures a rapid approach, and a shallow sliding line as the trajectory approaches the origin ensures precise positioning [132]. Koshkouei, *et al.* present a higher order dynamic sliding mode

controller (DSMC) that helps to improve system stability [133]. A recent paper by Nguyen, *et al.* an SMC based upon pulse width modulation (PWM) of low-cost solenoid valves, but the response has relatively large overshoot, poor time response, and accuracy not sufficient for the propose system [134]. Ning and Bone have recently published a thorough comparison of pneumatic system control techniques and development of a SMC [127, 135]. The authors claim a steady state error (SSE) equal to the encoder resolution of $0.01mm$ using a flow-control servo valve, pressure sensors on both chambers, and a large rodless cylinder.

This section details how these methods are extended to our system. Unlike many of the previously published systems, this robot uses relatively small air cylinders and long air supply lines making the control problem more challenging. The previously described system also all use either on-off of flow regulating valves; as described in section 3.5.1.1; this controller is based upon fast-acting piezoelectric pressure regulator valves. Further, the cylinder is not in a simple, well-defined test fixture as in the previously described works; the attached variable structure mechanism requires the controller to be adapted to the current state of the robot.

3.5.2.1 Sliding Mode Control Fundamentals

The general form of an n^{th} order dynamic system with a single control input is described as:

$$x^{(n)} = f(\vec{x}) + b(\vec{x})u \tag{3.14}$$

Where:

$\vec{x} = (x, \dot{x}, \ddot{x}, \cdots, x^{(n-1)})^T \in \mathbb{R}^n$ is the state vector, and

$u \in \mathbb{R}^1$ is the control input.

The specific equation of motion for this system can be found in equation 3.28.

The tracking goal is to make the state $\vec{x}$ follow the desired state $\vec{x}_d = (x_d, \dot{x}_d, \ddot{x}_d, \cdots, x_d^{(n-1)})^T \in \mathbb{R}^n$, where the desired command position is defined as x_d. The error vector, $\vec{e}$ is defined as:

$$\vec{e} = \vec{x}_d - \vec{x} = (e, \dot{e}, \ddot{e}, \cdots, e^{(n-1)})^T \in \mathbb{R}^n \tag{3.15}$$

The position tracking error is:

$$e = x_d - x \tag{3.16}$$

In general, a *sliding surface* in the phase plane of the error is defined as:

$$S(\vec{e}, t) = \left(\frac{d}{dt} + \lambda\right)^{(n-1)} e = 0 \tag{3.17}$$

For a second order system (n = 2), as that of the pneumatic cylinder described in Section 3.5.2.3, the sliding surface, S, is defined as:

$$S = \dot{e} + \lambda e = 0 \tag{3.18}$$

Where, λ is a parameter representing the slope of the line, $S = 0$, in the phase plane. This serves as a tuning parameter that relates to the time constant of the step response.

The solution to the differential equation 3.18 is:

$$\frac{d}{dt}e(t) = -\lambda e(t) \tag{3.19}$$

$$e(t) = e(0)exp\,(-\lambda t) \tag{3.20}$$

Therefore, for $\lambda > 0$:

$$\lim_{t \to \infty} e(t) = 0; \tag{3.21}$$

Thus, the error, $e(t)$, converges to zero. In the literature (*e.g.* [132, 127]), the control problem is often broken into two stages: (1) drive the system state to the sliding surface and (2) maintaining the state on the sliding surface as the error approaches the origin. Although the states may often follow a path resembling this trajectory, they may never reach the sliding surface, S. The controller works to asymptotically approach this surface as the error converges to zero.

If the states were to reach the sliding surface, maintaining that condition is equivalent to the statement: $\dot{S} = 0$. Assuming a fixed setpoint ($\dot{x_d} = 0$):

$$\begin{aligned} \dot{S} &= \ddot{e} + \lambda \dot{e} \\ &= -\ddot{x} - \lambda \dot{x} \end{aligned} \tag{3.22}$$

To ensure that the error always approaches the sliding manifold, S, the following condition must be satisfied:

$$S(\dot{e}, e)\dot{S}(\ddot{e}, \dot{e}) < 0 \tag{3.23}$$

3.5.2.2 Sliding Mode Control of the Pneumatic Cylinder

The sliding mode controller, u, is often implemented with two elements. One element is the primary controller that provides a continuous control signal that aims to drive the system state, $\vec{e}$, to the origin. The other element may be optionally added to improve response by

boosting the control signal when the system state is not in the vicinity of the sliding surface. The additional term is often discontinuous or closely resembling a discontinuous function. The controller is defined as:

$$u = u_{eq} + u_{sw} \tag{3.24}$$

Where:

u_{sw} is the *switching control* and is used to increase the control signal when the states are not in the immediate vicinity of the surface, $S = 0$. This is useful for overcoming unknown or unmodeled external disturbances such as static friction. This element of the controller is often described as a way to force the system to reach the sliding surface, $S = 0$. Although this element may take on any for, or not exist at all, three of the most commonly reported forms of the switching function are shown in Fig. 3.27.

u_{eq} is termed the *equivalent control* responsible for driving the error to the origin while asymptotically approaching the sliding surface, $S = 0$. This element of the controller is often described as a way to maintain $\dot{S} = 0$, i.e. keep the state on the sliding surface once it is reached.

The simplest form of the *switching control*, u_{sw} is the the switch function:

$$u_{sw} = k_{sw} sign(S) \tag{3.25}$$

Where, $k_{sw} > 0$ is a constant tuning parameter. u_{sw} can take on one of two values, $\{k_{sw}, -k_{sw}\}$, to push the system back towards the sliding manifold, $S = 0$. This type of controller can offer very high precision, but often results in a chattering effect as the

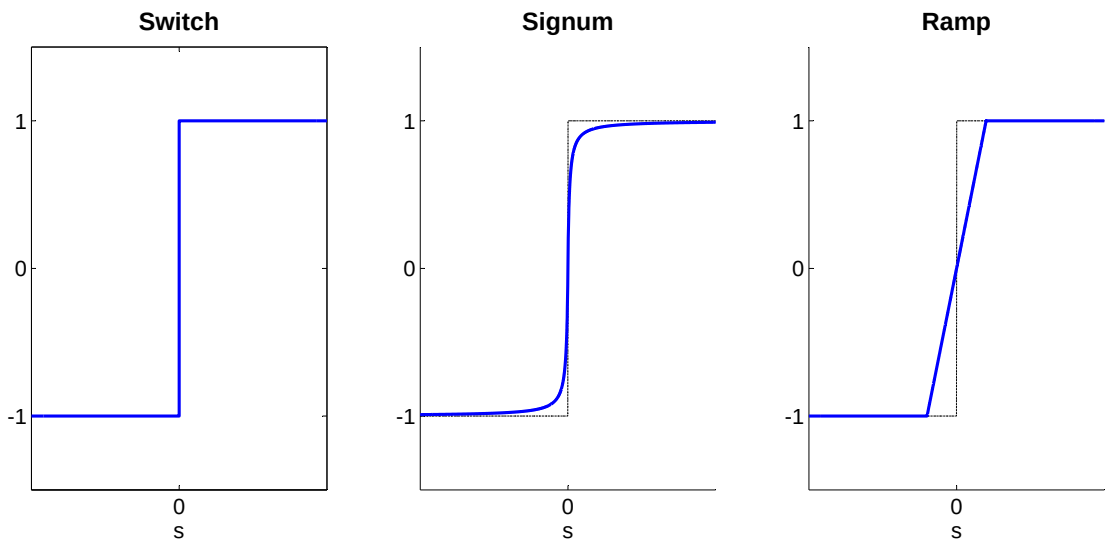

Figure 3.27: Examples of functions for the switching control input, u_{sw}. Simple switch function (left), signum function (center), and ramp function (right).

state oscillates around the sliding surface due to the discontinuity in the control input. In pneumatic control, this can actually act as a dithering controller and allow for very high accuracy by overcoming static friction; the comes at a cost of an oscillatory response.

This discontinuous controller can be approximated by the signum function:

$$u_{sw} = k_{sw}\frac{S}{|S| + d} \tag{3.26}$$

Where, again $k_{sw} > 0$ is a constant tuning parameter, and u_{sw} asymptotically approaches one of two values, $\{k_{sw}, -k_{sw}\}$, to push the system back towards the sliding surface, $S = 0$. The term, d, determines the width of the transition region near $S = 0$, and is identically $sign(S)$ when $d = 0$.

A common form of the *switching control* eliminates the discontinuity by linearly relating magnitude of the control input to the distance from the sliding surface in the neighbor-

hood of the surface, ($|S| < d$). $d > 0$ is therefore the boundary layer thickness. The form of this controller is:

$$u_{sw} = k_{sw} sat(S/d) \tag{3.27}$$

Where, for $|S| < d$, $u_{sw} = k_{sw}(S/d)$, and for $|S| \geq d$, u_{sw} reverts to Equation 3.25.

In addition, a deadband is sometimes utilized. In this case, $u_{sw} = 0$ when $|S| < d_{db}$, where d_{db} is the minimum distance from the sliding surface where the switching controller will be enabled. This implementation will help reduce chattering often inherent to this type of controller, but also results in higher SSE.

The second part of the controller is the *equivalent control*, u_{eq}, and is based upon the model of the plant. The second order system describing the dynamics pneumatic cylinder from Section 3.5.2.3 are described by:

$$\ddot{x} = \frac{1}{m}u(t) - \frac{1}{m}\mu_v \dot{x} - \frac{1}{m}F_{load} \tag{3.28}$$

Substituting the plant model into Equation 3.22 yields:

$$\dot{S} = -\left(\frac{1}{m}u(t) - \frac{1}{m}\mu_v \dot{x} - \frac{1}{m}F_{load}\right) - \lambda \dot{x} = 0 \tag{3.29}$$

Solving for $u(t)$ in this equation provides us with u_{eq} in Equation 3.24.

$$u_{eq} = (\mu_v - m\lambda)\,\dot{x} + F_{load} \tag{3.30}$$

3.5.2.3 Simulation Results

Matlab models of the system were implemented in Simulink. Fig. 3.28 shows the top level of the model. Each of the subsystems is modeled independently and shown in Fig. 3.30.

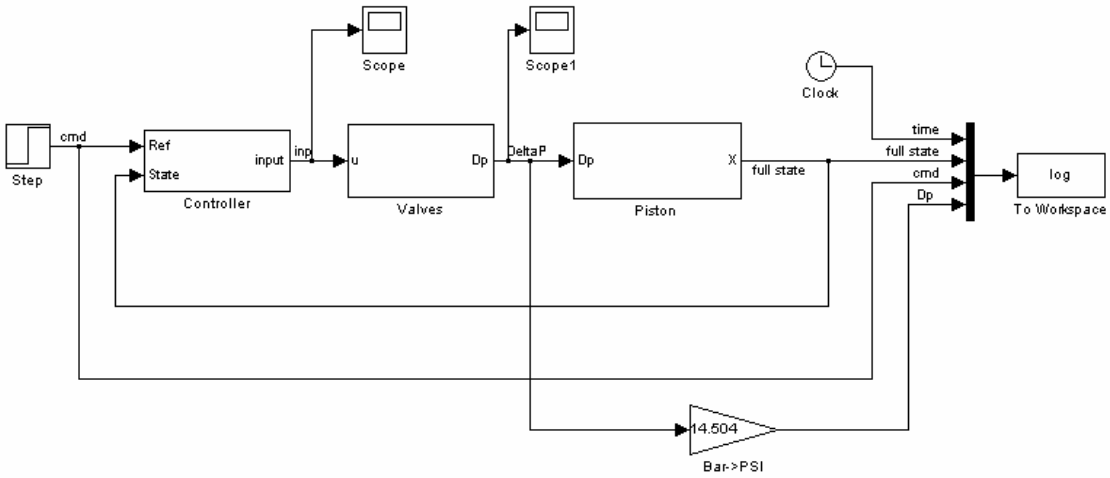

Figure 3.28: Matlab Simulink simulation of the system.

The first subsystem is the controller block. As shown in Fig. 3.30 (top), the controller takes in the command reference input and the current state. For the purposes of comparison of different control techniques, a switch allows two controllers to be evaluated. The first technique is the standard PID control. A simulation of PID control is shown in Fig. 3.29 (top). The PID controller is implemented with a high proportional gain, as required to overcome the static friction of the system. The performance of this controller is quite poor, as it produces an oscillatory response. The second technique evaluated is the sliding mode controller described in Section 3.5.2.2. In the simulation, this technique performed

as expected, producing a strong spike in control input to reach the sliding surface, and then a gradual decent along S to zero error and zero velocity as shown in the phase portrait in Fig. 3.29 (bottom).

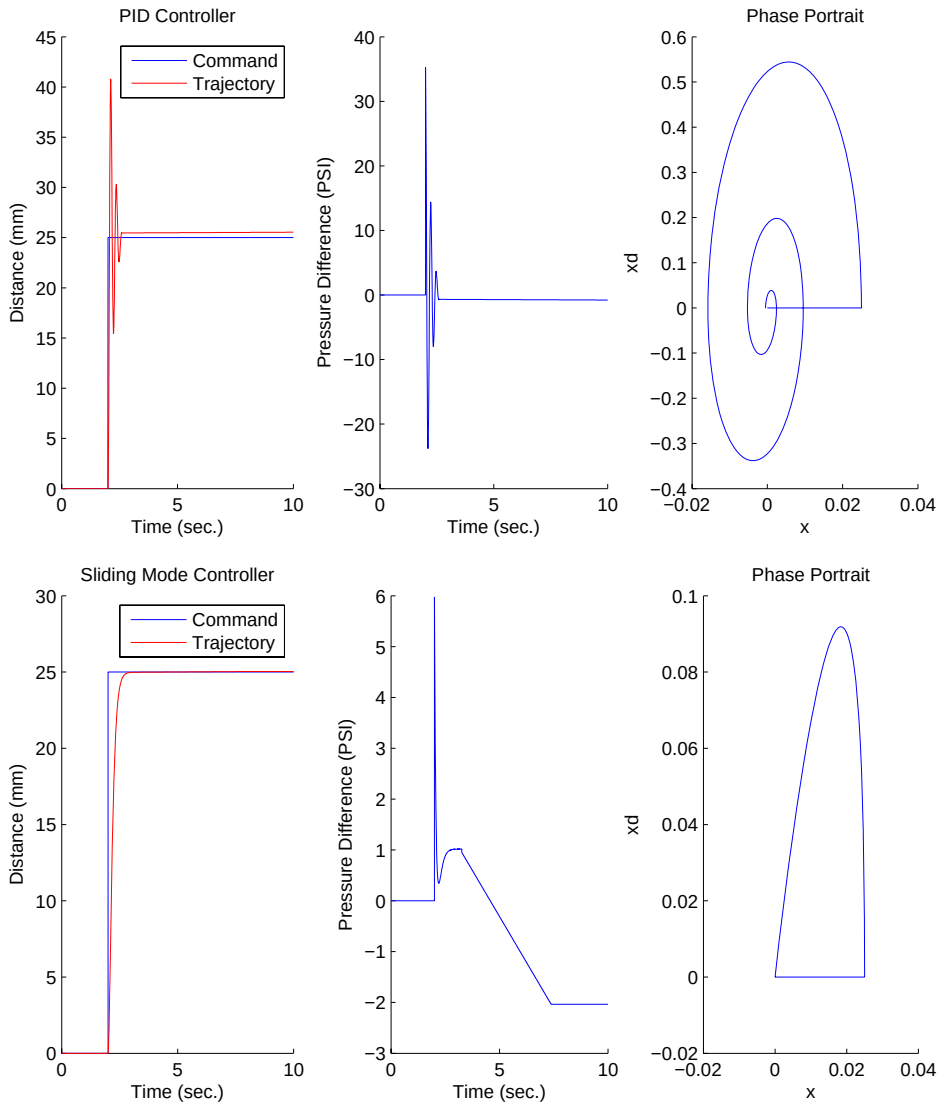

Figure 3.29: Simulated system responses using PID (top) and Sliding Mode (bottom) controllers.

The second subsystem is the valves as shown in Fig. 3.30 (middle). As described in Section 3.4.3, the pneumatic cylinder is controller by two opposing piezoelectric pressure regulator valves. The control input, u, from the controller block is the desired force on the cylinder piston. This block first splits the force between the cylinders. In the present embodiment of the controller, at any one time only one valve is pressurized and the other valve is set at zero pressure. It is possible to set the zero point at the midpoint of both cylinders and provide a force by a bilateral change in pressure. This potentially offers faster response times, but initial experiments proved difficult the synchronization and matching of the valve responses. The valve themselves are modeled by a second order system that matches the measured response closely.

The third subsystem is the mechanical system. The simulation shown in Fig. 3.30 (bottom) shows the model of the pneumatic cylinder itself. The cylinder is modeled as described in Section . All three subsystems are coupled together to evaluate and tune the controller designs.

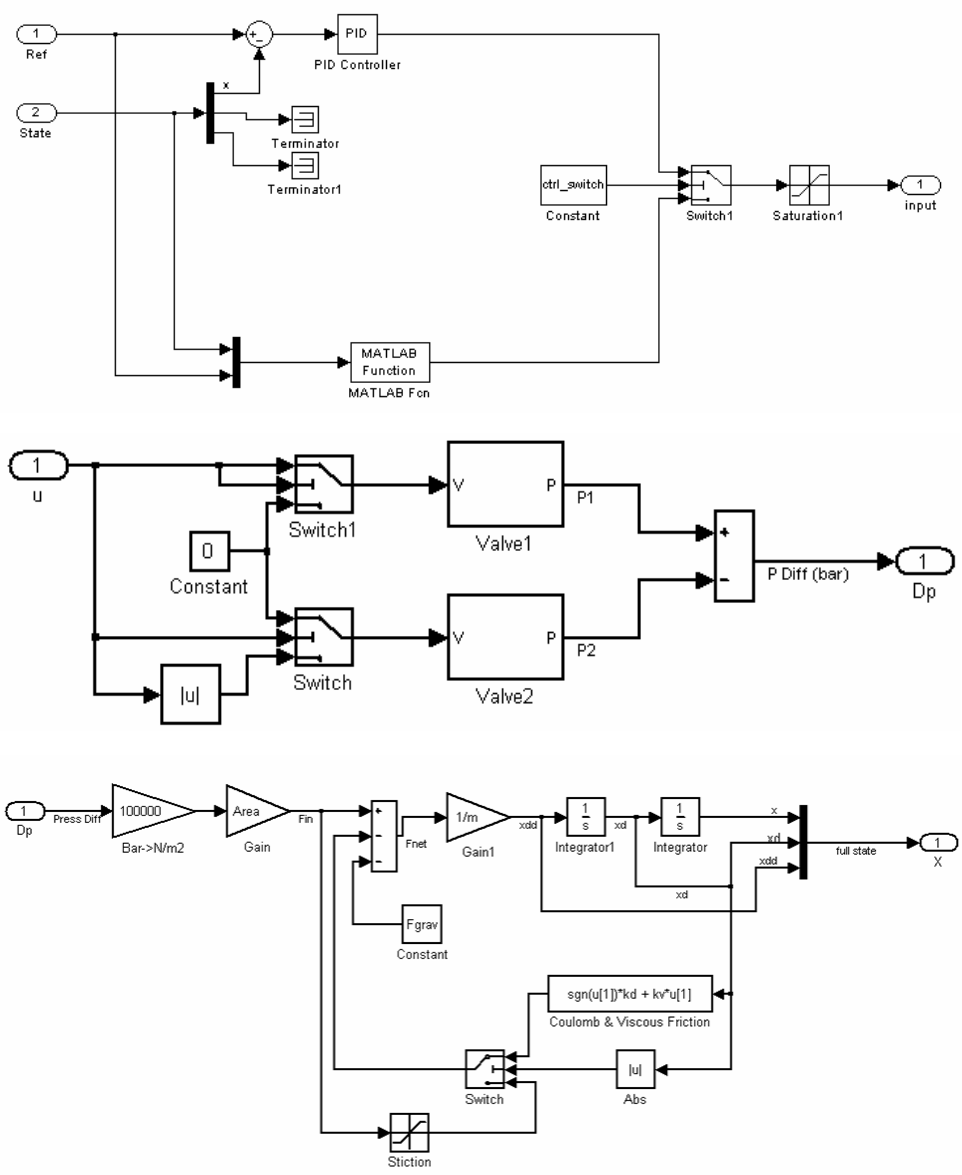

Figure 3.30: Matlab Simulink models of the controller (top), valves (middle), and mechanical system (bottom).

3.6 System Integration

3.6.1 Interface Software

The user interface for the robot is based on 3D Slicer open-source surgical navigation software (3D Slicer Software, http://www.slicer.org) [136] The navigation software runs on a Linux-based workstation in the scanner's console room. A customized graphical user interface (GUI) specially designed for the prostate intervention with the robot is described in [137]. The interface allows smooth operation of the system throughout the clinical workflow including registration, planning, targeting, monitoring and verification (Fig. 3.32). The workstation is connected to the robot and the scanner's console via Ethernet. NaviTrack and OpenIGT Link, open-source device connection and communication tools originally developed for virtual reality research [138], are used to exchange various types of data including control commands, position data, and images among the components. Fig. 3.31 shows the configuration used in the system as described in [139].

In the planning phase, pre-operative images are retrieved from a DICOM server and loaded into the navigation software. Registration is performed between the pre-operative planning images and intra-operative imaging using techniques such as those described by Haker, *et al.* [110]. Target points for the needle insertion are selected according to the pre-operative imaging, and the coordinates of the determined target points are selected in the planning GUI. Once the patient and the robot are placed in the MRI scanner, a 2D image of the fiducial frame is acquired and passed to the navigation software to calculate

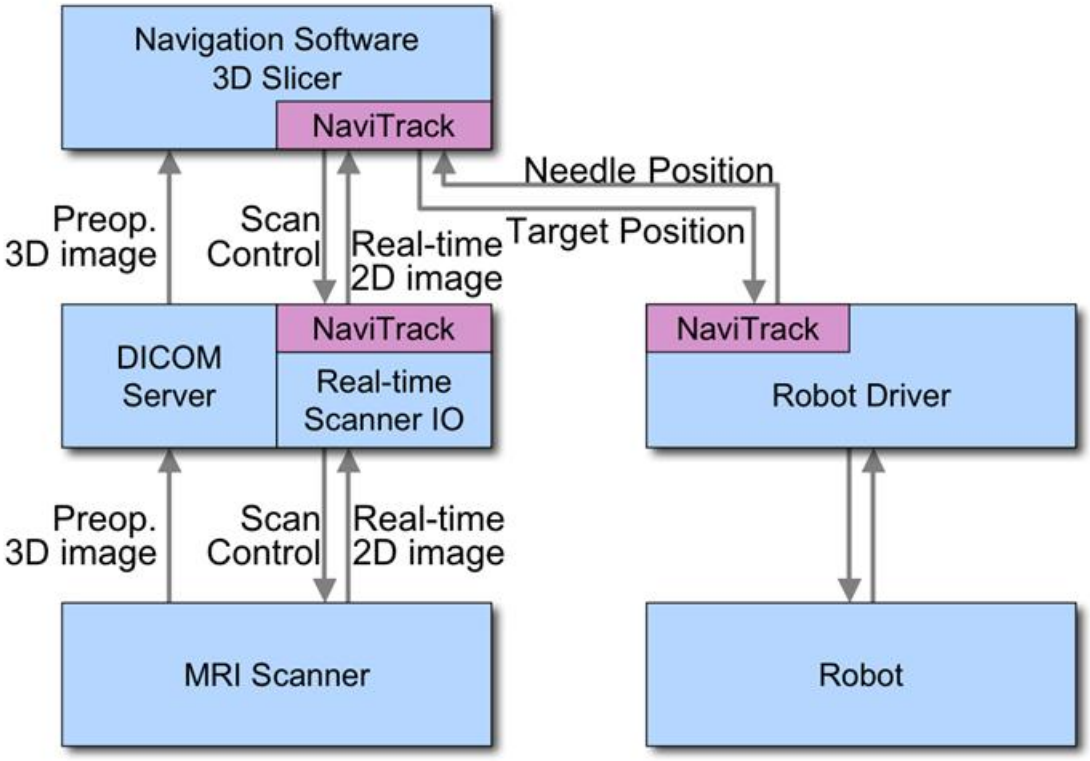

Figure 3.31: Diagram showing the connection and the data flow among the components from [139]. NaviTrack, an open-source device communication tool, is used to exchange control, position, and image data.

the 6-DOF pose of the robot base for the robot-image registration as described in Section 3.6.2.2. The position and orientation of the robot base is sent through the network from the navigation software to the robot controller. After the registration phase, the robot can accept target coordinates represented in the image (patient) coordinate system in standard Right-Anterior-Superior (RAS) coordinates.

During the procedure, a target and an entry point are chosen on the navigation software, and the robot is sent the coordinates and aligns the needle guide appropriately. In the cur-

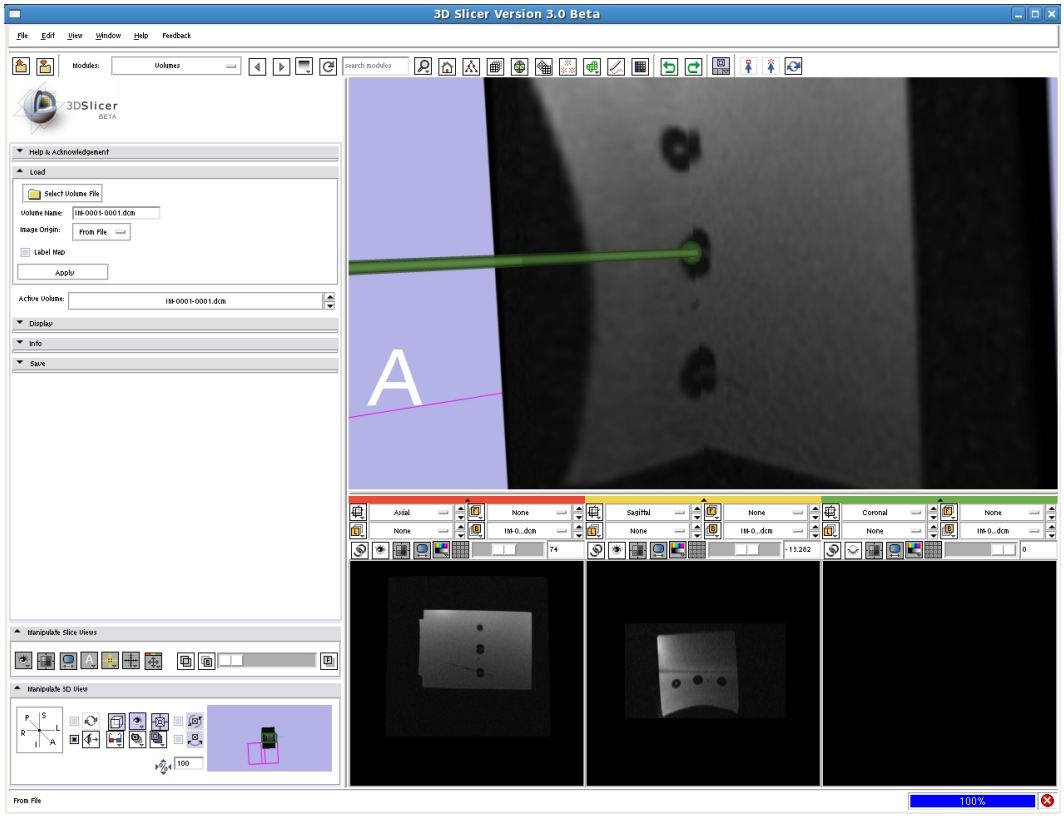

Figure 3.32: 3D Slicer planning workstation showing a selected target and the real-time readout of the robot's needle position. The line represents a projection along the needle axis and the sphere represents the location of the needle tip.

rent system, the needle is inserted manually while the needle position is monitored by an encoded needle guide and displayed in real-time on the display. Needle advancement in the tissue is visualized on the navigation software in two complementary ways: 1) a 3D view of needle model combined with pre-operative 3D image re-sliced in planes intersecting the needle axis, and 2) 2D real-time MR images acquired from the planes along or perpendicular to the needle path and continuously transferred from the scanner through the network. The former provides a high refresh rate (typically $/ge10Hz$), allowing a clinician to manipulate the needle interactively. The latter provides the changing shape or position of the

target lesion with relatively slower rate depending on the imaging speed (typically $0.5Hz$).

The interface software enables "closed-loop" needle guidance, where the action made by the robot is captured by the MR imaging, and immediately fed back to a physician to aid their decision for the next action. The reason for keeping a human in the loop is to increase the safety of the needle insertion, and to allow for the live MR images to monitor progress. The robot fully aligns the needle as planned before coming in contact with the patient. If necessary, the placement is adjusted responsive to the MR images. The physician performs the insertion under real-time imaging. Fig. 3.32 shows the planning software with an MR image of the phantom loaded and real-time feedback of the robot position is used to generate the overlaid needle axis model.

3.6.2 Coordinate Systems

3.6.2.1 Overview

Fig. 3.33 shows the pertinent coordinate systems for the robot. Equation 3.31 shows the corresponding serial chain of transformations.

$$T_{RAS}^{Tip} = T_{RAS}^{Z} \cdot T_{Z}^{Base} \cdot T_{Base}^{Rob} \cdot T_{Rob}^{Tip} \tag{3.31}$$

Where:

T_{RAS}^{Tip} is the needle tip in the patient coordinate system,

T_{RAS}^{Z} is the fiducial in patient coordinates as determined by the Z-frame calibration,

T_Z^{Base} is the mechanically fixed location of the fiducial on the robot,

T_{Base}^{Rob} is the robot end effector location with respect to the robot base as determined from the forward kinematics of the robot, and

T_{Rob}^{Tip} is the needle tip with respect to the end effector of the robot as determined by the encoded, passive needle guide.

In the planning software, a desired T_{RAS}^{Tip} is selected, representing the needle tip in patient coordinates. T_{RAS}^{Tip} and T_{RAS}^{Z} are sent to the robot controller from the planning workstation. The robot then calculates the required joint positions to achieve the goal.

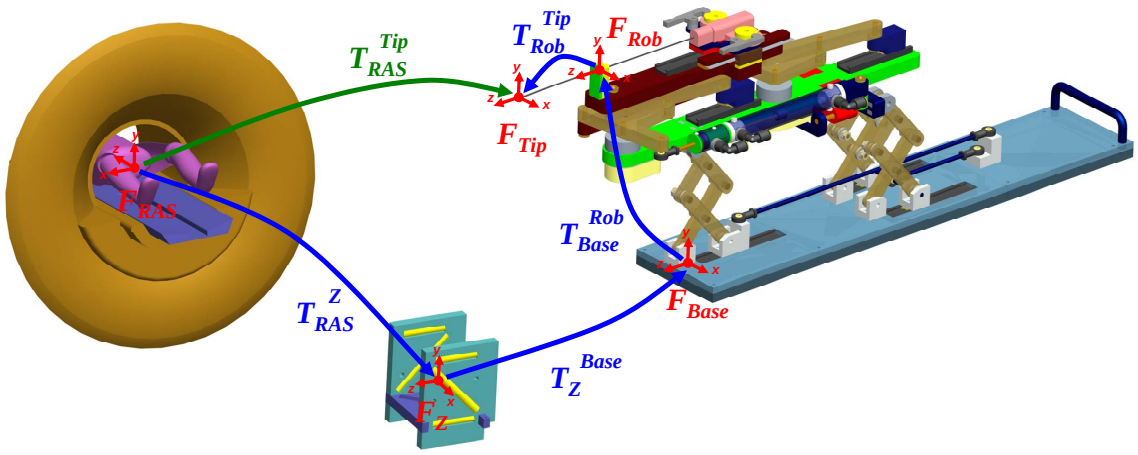

Figure 3.33: Coordinate frames of the complete system. T_{RAS}^{Tip} represents the needle tip in patient coordinates.

Breaking Equation 3.31 into two elements, registration error and robotic system error,

the corresponding chain can be represented as:

$$T_{RAS}^{Tip} = T_{RAS}^{Base} \cdot T_{Base}^{Tip} \tag{3.32}$$

Where:

$T_{RAS}^{Base} = T_{RAS}^{Z} \cdot T_{Z}^{Base}$ is the registration error, and

$T_{Base}^{Tip} = T_{Base}^{Rob} \cdot T_{Rob}^{Tip}$ is the robotic system error.

3.6.2.2 Registration to MR Imaging

Direct MRI-based image guidance shows great promise for high-level control, safety and verification. However, the refresh rate and resolution is not sufficient for use in low-level servo control of a robot joint. Practical methods of robot tracking are discussed by Krieger, *at al.* [43].

Inherently, the robot system has two different coordinate systems:

1. The image coordinate system (F_{RAS}) for the imaging, planning and verification.

2. The robot coordinate system (F_{Base}) based on the encoders for servo control of the robot joint described in Section 3.4.4.

The interpretation of positional information between these two coordinate systems is crucial for the targeting accuracy.

To achieve dynamic global registration between the robot and image coordinates, a Z-shape passive tracking fiducial, as described in [140], is attached on the robot base. The

tracking fiducial is similar to that described for registration of the Image Overlay stereotactic frame in Section 2.3.1 and the phantom registration to the validation system in Section 2.6.1.2. This registration step is concerned with finding T_{RAS}^{Z} as shown in Fig. 3.33.

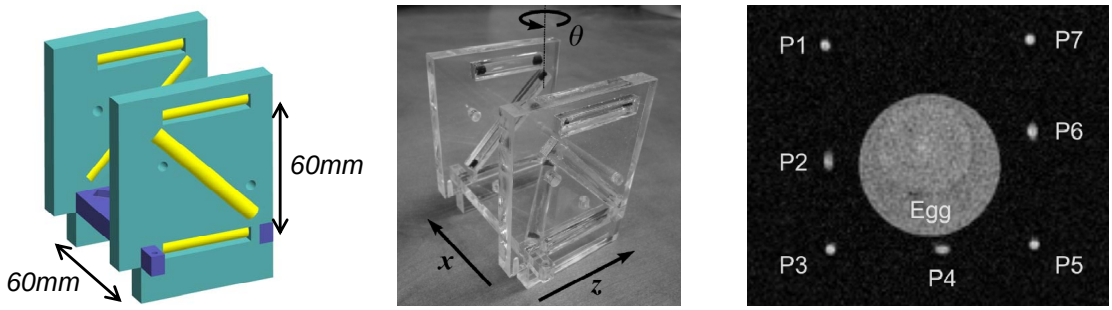

Figure 3.34: Z-frame tracking fiducial: dimensioned CAD model (left), photograph with labeled coordinate system (center) and a representative MR image slicing through the fiducial (right).

The rigid structure of the fiducial frame is made up of seven rigid glass tubes with $3mm$ inner diameters that are filled with contrast agent extracted from commercially available MRI fiducials (MR Spots, Beekley Corp., Bristol, CT). The rods are placed on three faces of a $60mm$ cube as shown in Fig. 3.34, and any arbitrary MR image slicing through rods provides the full 6-DOF pose of the frame using the techniques described by Susil, *et al.* [104] and Lee, *et al.* [105]. Hence, the robot's 6-DOF pose with respect to the scanner is resolved. Thus, by locating the fiducial attached to the robot, the transformation between image coordinates (where planning is performed) and robot coordinates is known. Once the transformation is known, the end effector location with respect to the fiducial frame is calculated from the kinematics and encoder positions and transformed to the representation in the image coordinate system.

3.6.2.3 Error Propagation

From Equation 3.31, it should be possible to exactly calculate the needle tip location and orientation in image coordinates, T_{RAS}^{Tip}. However, in reality T_{RAS}^{Base} and T_{Base}^{Tip} are not known precisely. [3] Using the *right* error representation, the measurement of each transformation is as follows:

$$\hat{T}_{RAS}^{Base} = T_{RAS}^{Base} \cdot \Delta_{RAS}^{Base} \tag{3.33}$$

$$\hat{T}_{Base}^{Tip} = T_{Base}^{Tip} \cdot \Delta_{Base}^{Tip} \tag{3.34}$$

Where:

T_{RAS}^{Base} and T_{Base}^{Tip} represent the nominal/true transformation, and

Δ_{RAS}^{Base} and Δ_{Base}^{Tip} represent the additive measurement error transformation.

The error could also be represented as a left error, where the error acts in the base frame and the actual transformation is applied to it. This is a less common representation:

$$\hat{T}_i = \Delta_i \cdot T_i \tag{3.35}$$

For this work, the right error representation is used. The error is represented as a homogeneous transformation that applies a rotation and translation after the nominal measurement. This error transformation is defined as follows:

$$\Delta_i = \begin{bmatrix} \Delta R_i & \vdots & \delta\vec{p}_i \\ \cdots & \cdots & \cdots \\ 0 & \vdots & 1 \end{bmatrix} \in SE(3) \tag{3.36}$$

[3] This section is based in part Gregory Fischer's Master's Thesis "Electromagnetic Tracker Characterization and Optimal Tool Design" [108], Johns Hopkins University, May 2005.

Where:

$\delta\vec{p}_i \in \mathbb{R}^3$ is the translation element of the error

$\Delta R_i = exp(\hat{\alpha}_i) \in SO(3)$ is the rotation element of the error

Where:

$\hat{\alpha}_i = skew(\vec{\alpha}_i) = skew(\delta\theta_i\vec{\omega}_i) \in so(3)$

$\omega_i \in \mathbb{R}^3$ is the unit vector along the axis of rotation

$\delta\Theta_i \in [0, 2\pi]$ is the non-negative angle about (radians)

Thus, the estimated transformation from F_{RAS} to F_{Tip} is:

$$\begin{aligned} \hat{T}^{Tip}_{RAS} &= \hat{T}^{Base}_{RAS} \cdot \hat{T}^{Tip}_{Base} \\ T^{Tip}_{RAS} \cdot \Delta^{Tip}_{RAS} &= [T^{Base}_{RAS} \cdot \Delta^{Base}_{RAS}] \cdot [T^{Tip}_{Base} \cdot \Delta^{Tip}_{Base}] \end{aligned} \tag{3.37}$$

Where:

T^{Tip}_{RAS} is the nominal / actual frame

Δ^{Tip}_{RAS} is the error in the estimated / calculated frame

To determine the error in the relative transformation T^{Tip}_{RAS}, we isolate the associated error:

$$\begin{aligned} \Delta^{Tip}_{RAS} &= (T^{Tip}_{RAS})^{-1} \cdot [T^{Base}_{RAS} \cdot \Delta^{Base}_{RAS}] \cdot [T^{Tip}_{Base} \cdot \Delta^{Tip}_{Base}] \\ &= (T^{Tip}_{Base})^{-1} \cdot \Delta^{Base}_{RAS} \cdot T^{Tip}_{Base} \cdot \Delta^{Tip}_{Base} \end{aligned} \tag{3.38}$$

Putting into homogeneous representation:

$$\begin{aligned} \begin{bmatrix} \Delta R^{Tip}_{RAS} & \delta\vec{p}_{\substack{Tip \\ RAS}} \\ 0 & 1 \end{bmatrix} = \begin{bmatrix} R^{Tip}_{Base} & \vec{p}_{\substack{Tip \\ Base}} \\ 0 & 1 \end{bmatrix}^{-1} \cdot \begin{bmatrix} \Delta R^{Base}_{RAS} & \delta\vec{p}_{\substack{Base \\ RAS}} \\ 0 & 1 \end{bmatrix} \cdot \\ \begin{bmatrix} R^{Tip}_{Base} & \vec{p}_{\substack{Tip \\ Base}} \\ 0 & 1 \end{bmatrix} \cdot \begin{bmatrix} \Delta R^{Tip}_{Base} & \delta\vec{p}_{\substack{Tip \\ Base}} \\ 0 & 1 \end{bmatrix} \end{aligned} \tag{3.39}$$

Passing the inverse through into the frames produces an expression for the error in the estimated frame:

$$\begin{bmatrix} \Delta R_{RAS}^{Tip} & \delta\vec{p}_{\substack{Tip \\ RAS}} \\ 0 & 1 \end{bmatrix} = \begin{bmatrix} (R_{Base}^{Tip})^{-1} & -(R_{Base}^{Tip})^{-1}\vec{p}_{\substack{Tip \\ Base}} \\ 0 & 1 \end{bmatrix} \cdot \begin{bmatrix} \Delta R_{RAS}^{Base} & \delta\vec{p}_{\substack{Base \\ RAS}} \\ 0 & 1 \end{bmatrix} \cdot \begin{bmatrix} R_{Base}^{Tip} & \vec{p}_{\substack{Tip \\ Base}} \\ 0 & 1 \end{bmatrix} \cdot \begin{bmatrix} \Delta R_{Base}^{Tip} & \delta\vec{p}_{\substack{Tip \\ Base}} \\ 0 & 1 \end{bmatrix} \tag{3.40}$$

In order to analyze the error, the next step is to break the error apart into rotational and translational components.

Position Error:

The position error, $\delta\vec{p}_{\substack{Tip \\ RAS}} \in \mathbb{R}^3$, can be described as:

$$\begin{aligned} \delta\vec{p}_{\substack{Tip \\ RAS}} =& (R_{Base}^{Tip})^{-1} \cdot \Delta R_{RAS}^{Base} \cdot R_{Base}^{Tip} \cdot \delta\vec{p}_{\substack{Tip \\ Base}} + (R_{Base}^{Tip})^{-1} \cdot \Delta R_{RAS}^{Base} \cdot \vec{p}_{\substack{Tip \\ Base}} \\ &+ (R_{Base}^{Tip})^{-1} \cdot \delta\vec{p}_{\substack{Base \\ RAS}} - (R_{Base}^{Tip})^{-1} \cdot \vec{p}_{\substack{Tip \\ Base}} \end{aligned} \tag{3.41}$$

Orientation Error:

The orientation error, $\Delta R_{RAS}^{Tip} \in SO(3)$, can be described as:

$$\Delta R_{RAS}^{Tip} = (R_{Base}^{Tip})^{-1} \cdot \Delta \cdot R_{RAS}^{Base} \cdot R_{Base}^{Tip} \cdot \Delta R_{Base}^{Tip} \tag{3.42}$$

Representation of Rotations:

For further analysis, we must define the representation of rotation errors and look for ways to simplify them. This is the same as the representation shown earlier, but now it is expand and linearized.

$$\Delta R = \Delta R(\vec{\alpha}) = exp(\hat{\alpha}) \in SO(3) \tag{3.43}$$

Where:

$\vec{\alpha} \in \mathbb{R}^3$ is a vector pointing along the axis of rotation

$\|\vec{\alpha}\|$ is the angle of rotation (radians)

$\hat{\alpha} = skew(\vec{\alpha}) \in so(3)$

Using the infinite series expansion of a matrix exponential to expand the rotation:

$$\begin{aligned} \Delta R &= e^{(\hat{\alpha})} \\ &= \sum_{j=0}^{\infty} \frac{1}{j!} \hat{\alpha}^j \\ &= I_3 + \hat{\alpha} + \frac{1}{2!}\hat{\alpha}^2 + \frac{1}{3!}\hat{\alpha}^3 + \cdots \end{aligned} \tag{3.44}$$

Since the magnitude of the rotation error is small, second order and higher terms will be negligible, and can be neglected. The result is the following linearization:

$$\begin{aligned} \Delta R &\approx I_3 + \hat{\alpha} \\ &\approx \begin{bmatrix} 1 & 0 & 0 \\ 0 & 1 & 0 \\ 0 & 0 & 1 \end{bmatrix} + \begin{bmatrix} 0 & -\alpha_3 & \alpha_2 \\ \alpha_3 & 0 & -\alpha_1 \\ -\alpha_2 & \alpha_1 & 0 \end{bmatrix} \end{aligned} \tag{3.45}$$

Now that the rotation error is approximated linearly, the next step is to plug this into the equations for position error and orientation error that were presented above. After plugging in and expanding the equations out, we get the following equations that are linear in terms of the errors

Linearizing the Position Error:

$$\begin{aligned}
\delta\vec{p}_{\substack{Tip\\RAS}} &= (R^{Tip}_{Base})^{-1}\Delta R^{Base}_{RAS}R^{Tip}_{Base}\delta\vec{p}_{\substack{Tip\\Base}} + (R^{Tip}_{Base})^{-1}\Delta R^{Base}_{RAS}\vec{p}_{\substack{Tip\\Base}} \\
&\quad + (R^{Tip}_{Base})^{-1}\delta\vec{p}_{\substack{Base\\RAS}} - (R^{Tip}_{Base})^{-1}\vec{p}_{\substack{Tip\\Base}} \\
&\approx (R^{Tip}_{Base})^{-1}(I_3 + \hat{\alpha}_{\substack{Base\\RAS}})R^{Tip}_{Base}\delta\vec{p}_{\substack{Tip\\Base}} + (R^{Tip}_{Base})^{-1}(I_3 + \hat{\alpha}_{\substack{Base\\RAS}})\vec{p}_{\substack{Tip\\Base}} \\
&\quad + (R^{Tip}_{Base})^{-1}\delta\vec{p}_{\substack{Base\\RAS}} - (R^{Tip}_{Base})^{-1}\vec{p}_{\substack{Tip\\Base}} \\
&\approx \delta\vec{p}_{\substack{Tip\\Base}} + (R^{Tip}_{Base})^{-1}\hat{\alpha}_{\substack{Base\\RAS}}R^{Tip}_{Base}\delta\vec{p}_{\substack{Tip\\Base}} + (R^{Tip}_{Base})^{-1}\hat{\alpha}_{\substack{Base\\RAS}}\vec{p}_{\substack{Tip\\Base}} \\
&\quad + (R^{Tip}_{Base})^{-1}\delta\vec{p}_{\substack{Base\\RAS}} \\
&\approx \delta\vec{p}_{\substack{Tip\\Base}} - skew(R^{Tip}_{Base}\vec{\alpha}_{\substack{Base\\RAS}}))\delta\vec{p}_{\substack{Tip\\Base}} + (R^{Tip}_{Base})^{-1}\hat{\alpha}_{\substack{Base\\RAS}}\vec{p}_{\substack{Tip\\Base}} \\
&\quad + (R^{Tip}_{Base})^{-1}\delta\vec{p}_{\substack{Base\\RAS}}
\end{aligned} \tag{3.46}$$

Linearizing the Orientation Error:

$$\begin{aligned}
\Delta R^{Tip}_{RAS} &= (R^{Tip}_{Base})^{-1}\Delta R^{Base}_{RAS}R^{Tip}_{Base}\Delta R^{Tip}_{Base} \\
&\approx (R^{Tip}_{Base})^{-1}(I_3 + \hat{\alpha}_{\substack{Base\\RAS}})R^{Tip}_{Base}(I_3 + \hat{\alpha}_{\substack{Tip\\Base}}) \\
&\approx [(R^{Tip}_{Base})^{-1} + (R^{Tip}_{Base})^{-1}\hat{\alpha}_{\substack{Base\\RAS}}]R^{Tip}_{Base}(I_3 + \hat{\alpha}_{\substack{Tip\\Base}}) \\
&\approx [I_3 + (R^{Tip}_{Base})^{-1}\hat{\alpha}_{\substack{Base\\RAS}}R^{Tip}_{Base}](I_3 + \hat{\alpha}_{\substack{Tip\\Base}}) \\
&\approx [I_3 - skew(R^{Tip}_{Base}\vec{\alpha}_{\substack{Base\\RAS}})](I_3 + \hat{\alpha}_{\substack{Tip\\Base}}) \\
&\approx I_3 - skew(R^{Tip}_{Base}\vec{\alpha}_{\substack{Base\\RAS}}) + \hat{\alpha}_{\substack{Tip\\Base}} - skew(R^{Tip}_{Base}\vec{\alpha}_{\substack{Base\\RAS}})\hat{\alpha}_{\substack{Tip\\Base}}
\end{aligned} \tag{3.47}$$

Now that we have equations for the error tool registration error that are linear in terms of the individual frame errors, the logical next step is to place bounds on the magnitudes of the position and orientation registration error.

Bounds Position Error:

From before we have:

$$\begin{aligned}\delta\vec{p}_{\substack{Tip\\RAS}} \approx & \delta\vec{p}_{\substack{Tip\\Base}} - skew\left(R^{Tip}_{Base}\vec{\alpha}_{\substack{Base\\RAS}}\right)\delta\vec{p}_{\substack{Tip\\Base}} + (R^{Tip}_{Base})^{-1}\hat{\alpha}_{\substack{Base\\RAS}}\vec{p}_{\substack{Tip\\Base}} \\ & + (R^{Tip}_{Base})^{-1}\delta\vec{p}_{\substack{Base\\RAS}}\end{aligned} \tag{3.48}$$

Taking the norm of both sides:

$$\begin{aligned}\|\delta\vec{p}_{\substack{Tip\\RAS}}\| \approx & \|\delta\vec{p}_{\substack{Tip\\Base}} - skew\left(R^{Tip}_{Base}\vec{\alpha}_{\substack{Base\\RAS}}\right)\delta\vec{p}_{\substack{Tip\\Base}} + (R^{Tip}_{Base})^{-1}\hat{\alpha}_{\substack{Base\\RAS}}\vec{p}_{\substack{Tip\\Base}} \\ & + (R^{Tip}_{Base})^{-1}\delta\vec{p}_{\substack{Base\\RAS}}\|\end{aligned} \tag{3.49}$$

Using the triangle inequality to put a bound on the error magnitude:

$$\begin{aligned}\|\delta\vec{p}_{\substack{Tip\\RAS}}\| \leq & \|\delta\vec{p}_{\substack{Tip\\Base}}\| + \|skew\left(R^{Tip}_{Base}\vec{\alpha}_{\substack{Base\\RAS}}\right)\delta\vec{p}_{\substack{Tip\\Base}}\| \\ & + \|(R^{Tip}_{Base})^{-1}\hat{\alpha}_{\substack{Base\\RAS}}\vec{p}_{\substack{Tip\\Base}}\| + \|(R^{Tip}_{Base})^{-1}\delta\vec{p}_{\substack{Base\\RAS}}\|\end{aligned} \tag{3.50}$$

Since rigid body rotations preserve length, the rotation matrix can be removed without affecting the magnitude:

$$\begin{aligned}\|\delta\vec{p}_{\substack{Tip\\RAS}}\| \leq & \|\delta\vec{p}_{\substack{Tip\\Base}}\| + \|skew\left(R^{Tip}_{Base}\vec{\alpha}_{\substack{Base\\RAS}}\right)\delta\vec{p}_{\substack{Tip\\Base}}\| \\ & + \|\hat{\alpha}_{\substack{Base\\RAS}}\vec{p}_{\substack{Tip\\Base}}\| + \|\delta\vec{p}_{\substack{Base\\RAS}}\|\end{aligned} \tag{3.51}$$

Since multiplying a small displacement by a skew matrix generated from the approximation of a small rotation produces almost negligible values, this component can be removed as well. Thus, we have the upper bound on the translational needle tip error:

$$\|\delta\vec{p}_{\substack{Tip\\RAS}}\| \leq \|\delta\vec{p}_{\substack{Tip\\Base}}\| + \|\hat{\alpha}_{\substack{Base\\RAS}}\vec{p}_{\substack{Tip\\Base}}\| + \|\delta\vec{p}_{\substack{Base\\RAS}}\| \tag{3.52}$$

$\|\delta\vec{p}_{\substack{Tip\\Base}}\|$ is the error localization of the robot tip based on the robot's forward kinematics; this, of course, adds directly to the tip error. The term $\|\delta\vec{p}_{\substack{Base\\RAS}}\|$ is the translational

error related to registration, and also directly translates into error in needle position. More significant can be the error in tip position due to rotational error in the Z-frame registration procedure. The term $\|\hat{\alpha}_{\substack{Base\\RAS}}\vec{p}_{\substack{Tip\\Base}}\|$ effectively multiplies the distance of the needle tip from the Z-frame fiducial by the angular registration error. Although the magnitude of the error may be mitigated by keeping the fiducial as close as possible to the needle tip, it is clear that resolving the orientation of the tracking fiducial is of the utmost importance.

Bounds Orientation Error:

From before we have:

$$\Delta R^{Tip}_{RAS} \approx I_3 + \hat{\alpha}_{\substack{Tip\\RAS}} \approx I_3 - skew(R^{Tip}_{Base}\vec{\alpha}_{\substack{Base\\RAS}}) + \hat{\alpha}_{\substack{Tip\\Base}} - skew\left(R^{Tip}_{Base}\vec{\alpha}_{\substack{Base\\RAS}}\right)\hat{\alpha}_{\substack{Tip\\Base}} \quad (3.53)$$

Isolating the error term:

$$\hat{\alpha}_{\substack{Tip\\RAS}} \approx -skew(R^{Tip}_{Base}\vec{\alpha}_{\substack{Base\\RAS}}) + \hat{\alpha}_{\substack{Tip\\Base}} - skew\left(R^{Tip}_{Base}\vec{\alpha}_{\substack{Base\\RAS}}\right)\hat{\alpha}_{\substack{Tip\\Base}} \quad (3.54)$$

Removing higher order error terms:

$$\hat{\alpha}_{\substack{Tip\\RAS}} \approx -skew\left(R^{Tip}_{Base}\vec{\alpha}_{\substack{Base\\RAS}}\right) + \hat{\alpha}_{\substack{Tip\\Base}} \quad (3.55)$$

Converting the skew symmetric matrices into the associated Rodriguez vectors:

$$vec\left(\hat{\alpha}_{\substack{Tip\\RAS}}\right) \approx vec\left(-skew\left(R^{Tip}_{Base}\vec{\alpha}_{\substack{Base\\RAS}}\right) + \hat{\alpha}_{\substack{Tip\\Base}}\right) \quad (3.56)$$

$$\vec{\alpha}_{\substack{Tip\\RAS}} \approx -R^{Tip}_{Base}\vec{\alpha}_{\substack{Base\\RAS}} + \vec{\alpha}_{\substack{Tip\\Base}} \quad (3.57)$$

Taking the norm of both sides:

$$\|\vec{\alpha}_{\substack{Tip\\RAS}}\| \approx \| - R^{Tip}_{Base}\vec{\alpha}_{\substack{Base\\RAS}} + \vec{\alpha}_{\substack{Tip\\Base}}\| \quad (3.58)$$

Using the triangle inequality to get a bound on the error:

$$\|\vec{\alpha}_{\substack{Tip \\ RAS}}\| \leq \|R^{Tip}_{Base}\vec{\alpha}_{\substack{Base \\ RAS}}\| + \|\vec{\alpha}_{\substack{Tip \\ Base}}\| \tag{3.59}$$

Since rigid body rotations preserve length, the rotation matrix can be removed without affecting the magnitude:

$$\|\vec{\alpha}_{\substack{Tip \\ RAS}}\| \leq \|\vec{\alpha}_{\substack{Base \\ RAS}}\| + \|\vec{\alpha}_{\substack{Tip \\ Base}}\| \tag{3.60}$$

Plugging in the rotation angles associated with the Rodriguez vectors, we get a bound on the angular error:

$$|\delta\theta_{\substack{Tip \\ RAS}}| \leq |\delta\theta_{\substack{Base \\ RAS}}| + |\delta\theta_{\substack{Tip \\ Base}}| \tag{3.61}$$

Therefore, for a given magnitude of angular error for the image-based registration and robot localization, we can calculate bounds on the relative transformation's rotational error. This is a worst-case scenario and may result in a severe overestimation of the error.

3.7 System Evaluation

The robotic system is evaluated in three distinct phases:

- Evaluation of the MR compatibility of the robot.
- Evaluation of the workspace and workflow.
- Evaluation of the localization and placement accuracies.

3.7.1 MRI Compatibility

As described in Section 3.3.3, MR compatibility includes three elements: (1) safety, (2) preserving image quality, and (3) maintaining functionality. Safety issues such as RF heating are minimized by isolating the robot from the patient, avoiding wire coils, and avoiding resonances in components of the robot; ferrous materials are completely avoided to prevent the chance of a projectile. Image quality is maintained by again avoiding ferromagnetic materials, limiting conductive materials near the imaging site, and avoiding RF sources that can interfere with the field homogeneity and sensed RF signals. Pneumatic actuation and optical sensing, as described in Section 3.4, preserve full functionality of the robot in the scanner during imaging. The MR compatibility of the system is thoroughly evaluated in [91].

Compatibility was evaluated on a 3T Philips Achieva scanner. A $\varnothing 110mm$, fluid-filled spherical MR phantom was placed in the isocenter and the robot placed such that the tip

Table 3.3: Scan Parameters for Robot MRI Compatibility Evaluation

Protocol	*Thickness*	*FOV*	*# Slices*	*TE*	*TR*	*Flip Angle*	*NEX*
T2 TSE	3 mm	280 mm	7	90 ms	5600 ms	90^o	1
T1 FFE	3 mm	280 mm	7	2.3 ms	264 ms	75^o	1
TFE/FGRE	3 mm	280 mm	7	10 ms	26 ms	70^o	1

was at a distance of $120mm$ from the center of the phantom (a representative depth from perineum to prostate) as shown in Fig. 3.35 (left). The phantom was imaged using three scan protocols typically used in prostate imaging at the Brigham and Women's Hospital: 1) T2 weighted turbo spin echo, 2) T1 weighted fast field gradient echo, and 3) "Real-time" turbo field gradient echo. The specific scan parameters for this trial are listed in Table 3.3.

A baseline scan with each sequence was taken of the phantom with no robot components using two channel medium size flex coil, similar to those often used in prostate imaging. The following imaging series were taken in each of the following configurations: 1) Phantom only, 2) Controller in room and powered, 3) Robot placed in scanner bore, 4) Robot electrically connected to controller and 5) Robot moving during imaging (only with T1W imaging). For each step, all three imaging sequences were performed and both magnitude and phase images were collected.

SNR degradation serves as the metric for impact on image quality, and thus compatibility of the system. From the recently accepted standard "Determination of SNR in Diagnostic Magnetic Resonance Imaging," published by the National Electrical Manufacturers

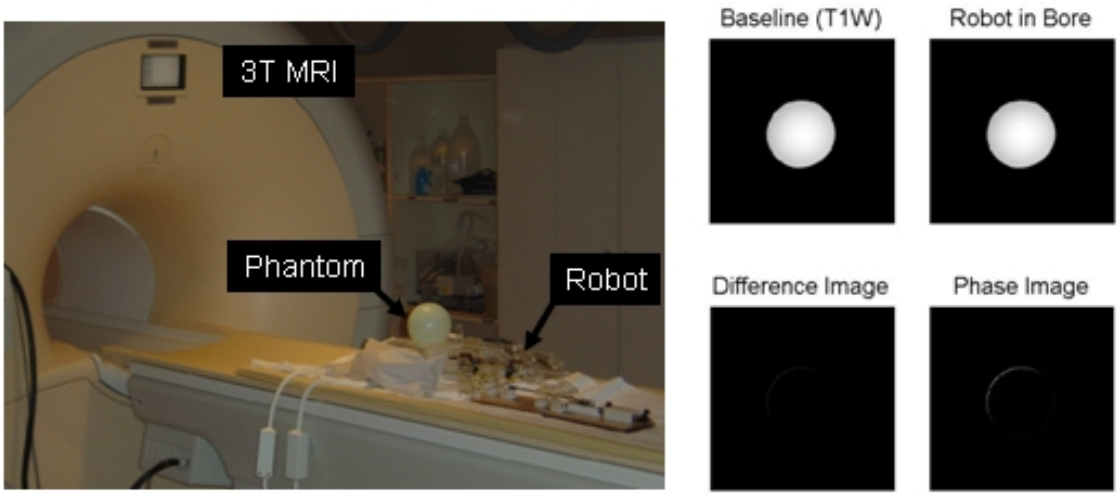

Figure 3.35: Configuration of the system for MRI compatibility trials. The robot is placed on the bed with the center of a spherical phantom (left) $120mm$ from the tip of the robot and the controller is placed in the scanner room near the foot of the bed. Images of the phantom taken with the T1W sequence are shown with and without the robot present (right).

Association (NEMA):

> Image SNR is a parameter that relates to clinical usefulness of magnetic resonance images and also is a sensitive measure of hardware performance. Experience has shown that variations in system calibration, gain, coil tuning, radiofrequency shielding, or other similar parameters are usually demonstrated by a corresponding change in image SNR. [141]

SNR of the MR images is defined as the mean signal in a $25mm$ square at the center of the homogeneous sphere divided by the standard deviation of the signal in that same region. The SNR was normalized by the value for the baseline image; thus limiting any bias in choice of calculation technique or location. The technique used for measuring SNR is equivalent to that described by the NEMA standard [141]. The SNR is calculated as described in *Method 4* of the cited standard:

$$SNR = \frac{S}{imagenoise} \tag{3.62}$$

Where, S is the mean pixel value within the Measurement Region of Interest (MROI) and $imagenoise$ is the standard deviation (SD) of the selected Noise Measurement Region of Interest (NMROI). The location of the NMROI has a significant impact on calculated SNR; the selected NMROI in the top-left corner minimizes variance between image slices and is outside of ghosting artifacts as described by Firbank, *et al.* [120].

SNR was evaluated at seven $3mm$ thick slices (representing a $25mm$ cube) at the center of the sphere for each of the three imaging sequences. The points in the graph in Fig. 3.36 show the SNR in the phantom for each of the seven $3mm$ thick slices for each sequence at each configuration. The lines represent the average SNR in the $25mm$ cube at the center of the spherical phantom for each sequence at each configuration. When the robot was operational, the reduction in SNR of the cube at the phantom's center for these pulse sequences is shown in Table 3.4.

Table 3.4: Robotic System MRI Compatibility Results

	Fast Field Echo *T1W FFE*	*Turbo Spin Echo* *T2W TSE*	*Turbo Field Echo* *TFE/FGRE*
Average SNR Degradation	5.5%	4.2%	1.1%

Further qualitative means of evaluating the effect of the robot on image quality are obtained by examining prostate images taken both with and without the presence of the robot. Fig. 3.40 (right) shows images of the prostate of a volunteer placed in the scanner bore on the leg rest. With the robot operational, there is no visually identifiable loss in

image quality of the prostate.

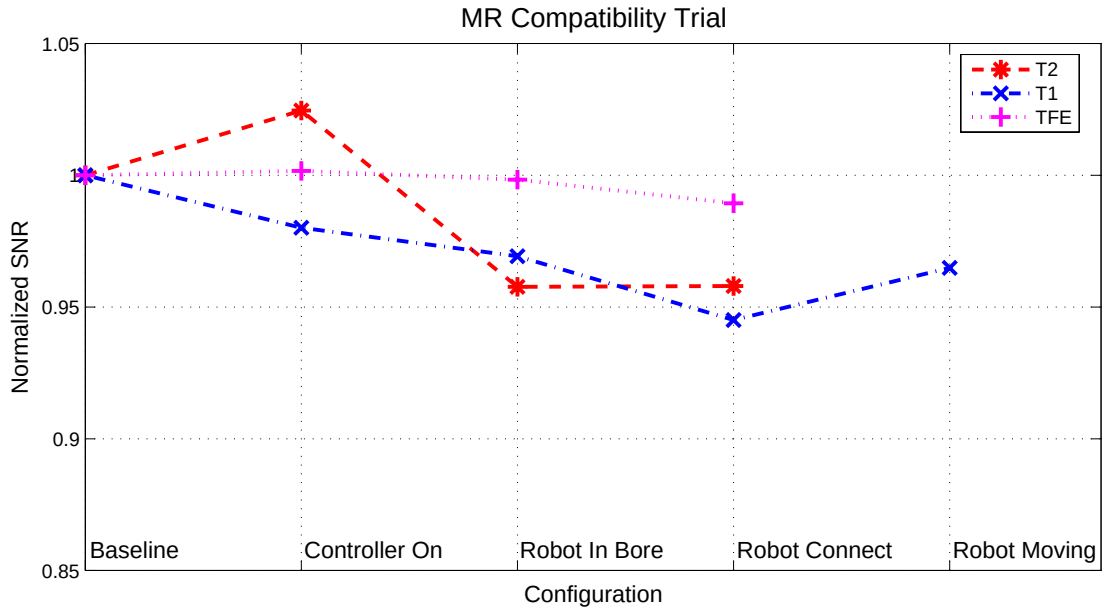

Figure 3.36: Quantitative measure of image quality for three standard prostate imaging protocols with the system in different configurations. Lines represent mean SNR within $25mm$ cube at center of homogeneous phantom normalized by the baseline.

3.7.2 Robot Accuracy

Accuracy assessment is broken into two parts: *localization* and *placement*. These two must be distinguished, especially in many medical applications. In prostate biopsy, it is essential to know exactly where a biopsy comes from in order to be able to form a treatment plan if cancer is located. In brachytherapy treatment, radioactive seed placement plans must be made to avoid cold spots where irradiation is insufficient; by knowing where seeds are placed, the dosimetry and treatment plan can be interactively updated. Based on encoder resolution, localization accuracy of the robot in free space is better than $0.1mm$ in all

directions.

3.7.2.1 Pneumatic Control Accuracy

Positioning accuracy is dependent on the servo pneumatic control system. The current control algorithm for pneumatic servo control is based upon sliding mode control (SMC) techniques as described in Section 3.5.2. The pneumatic cylinder was commanded to move back and forth between two points and the steady state error for each move was recorded. The average positioning accuracy was $0.26mm$ RMS error.

The SMC requires a tuning parameter for the boundary layer thickness around the sliding surface. This is effectively an intentional deadband used to minimize chatter. This accuracy was achieved using a step response with minimal overshoot and chatter. Positioning errors of the unloaded cylinder in free space can be limited to the encoder resolution of $0.01mm$ when chatter/osscilation are tolerable.

In addition to point-to-point moves, the positioning accuracy of the cylinder alone in free space has been evaluated for dynamic trajectory tracking. The cylinder was commanded to follow a $0.125Hz$, $20mm$ amplitude sine wave. Fig. 3.37 shows the tracking results for the cylinder. The RMS error for this task was $0.23mm$ which approximates the set deadband of $0.30mm$. This boundary layer thickness where u_{sw} is not sufficient to move the cylinder results in a staircase-like motion as shown in Fig. 3.38. The additional jitter at the peaks appears when there is a change in direction of the cylinder. As the cylinder changes direction, the pressure on one side of the cylinder is commanded to increase from

zero; as shown in Fig. 3.17, there is a lag in the valve response when pressure increases from zero. A differential pressure between the cylinder sides based about a nominal pressure greater than zero could eliminate this problem, but nonuniform valve responses made this impractical.

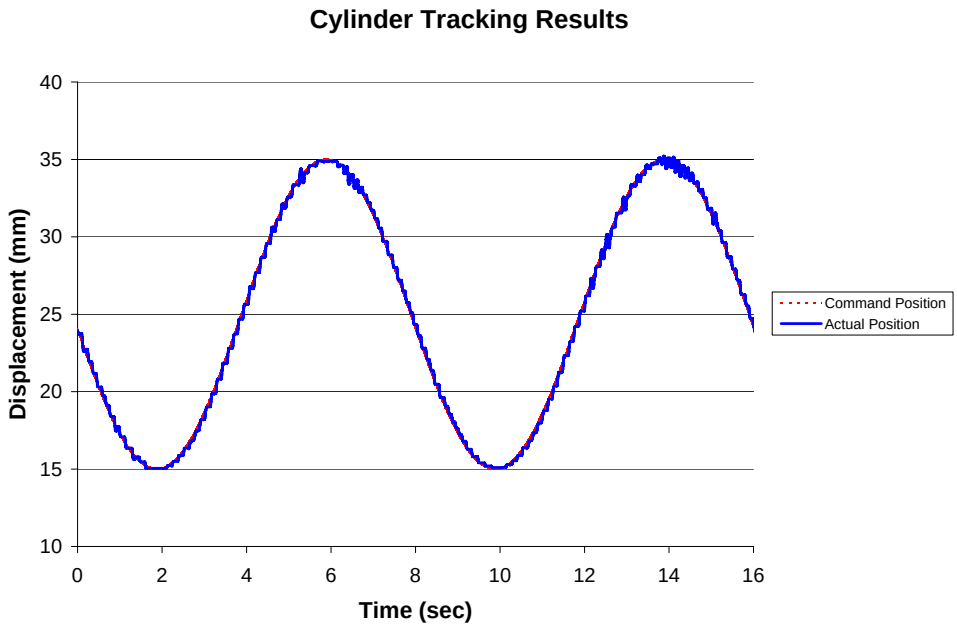

Figure 3.37: Dynamic tracking results for the pneumatic cylinder for an $8sec$ period, $20mm$ amplitude sine wave.

3.7.2.2 Robotic System Accuracy

As shown in Section 3.4.5, the kinematics for the robot are not linearly related to cylinder position. So, the accuracy results in the previous section do not directly translate into positioning accuracy of the robot. In particular, the robot is inherently more accurate at the upper limits of its travel due to both the encoder resolution corresponding to motions in

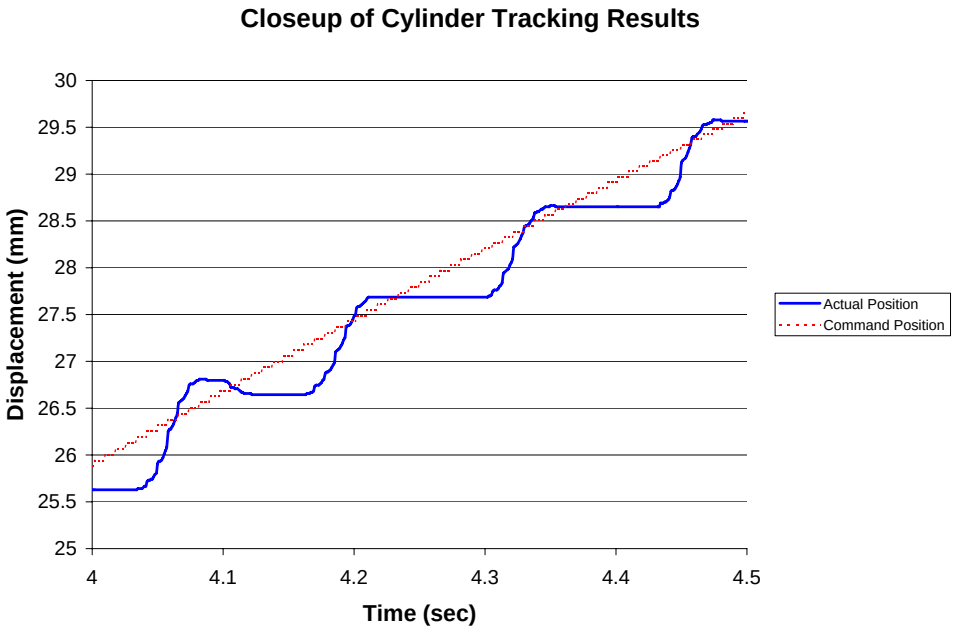

Figure 3.38: Close-up of tracking results for the pneumatic cylinder.

that range and the significant decrease in control effort as the position is elevated. Gravity compensation has also been applied to the vertical motion.

With the robot fully connected, positioning accuracy of the robot with no additional external loading was assessed. The robot was commanded to move back and forth between two configurations and the steady state error for each move was recorded. The average positioning accuracy was $0.94mm$ RMS error over 120 point-to-point moves. The corresponding step response for the motion is shown in Fig. 3.39. It is clear that, although there is a chatter in the motion profile, there is negligible overshoot and the steady state error is minimal. The time response is intentionally slowed so that the overshoot is minimized. For this application, high sped motion is not required; it is in fact undesirable. This accuracy

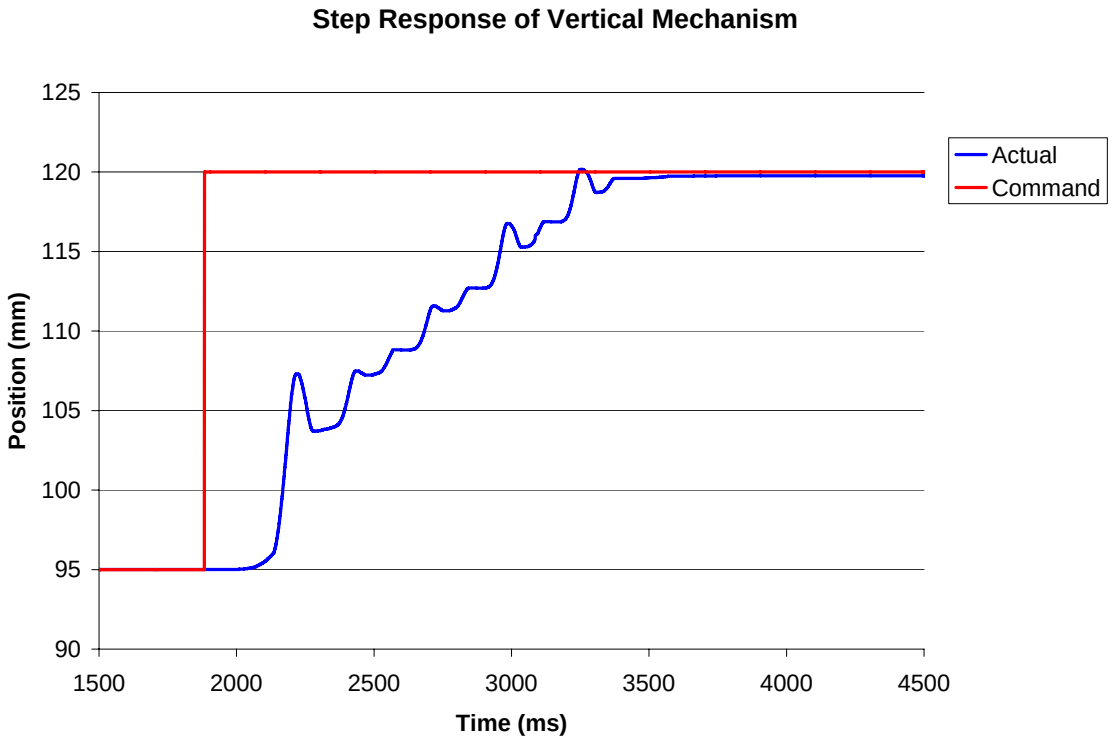

Figure 3.39: The step response for vertical motion of the robotic system.

is assessed based upon the encoder readings. Deflection of the mechanism may result in additional error, but it is expected to be insignificant. There will be no external load on the robot during motion, and minimal loading during insertion as the needle is inserted while the joint axes are braked.

Continued development and refinement of the pneumatic control architecture and mechanical design should allow for even high precision and smoother motions. The goal is for the target positioning accuracy per axis is $0.1mm$, which approaches the resolution of the encoders when scaled to the end effector motion.

3.7.3 Pre-Clinical Evaluation

To evaluate the overall clinical layout and workflow, the robot was placed in the bore of a 3T Philips Achieva scanner inside of the leg rest with a volunteer as shown in Fig. 3.40 (left). Two channel medium size flex coils were used for this trial; endorectal coils can be used for clinical case to obtain optimal image quality. There was adequate room for a patient and the robot was able to maintain its necessary workspace. Further studies of this are underway where volunteers are imaged on the leg rest in the appropriate semi-lithotomy position and the prostate and anatomical constraints are analyzed.

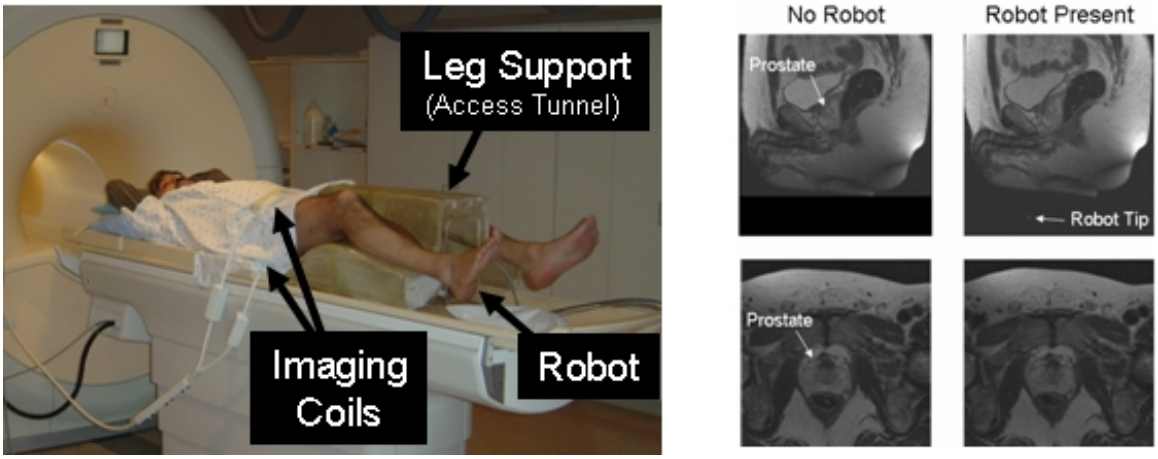

Figure 3.40: Qualitative analysis of prostate image quality. Patient is placed on the leg support and the robot sits inside of the support tunnel inside the scanner bore (left). T2 weighted sagittal and transverse images of the prostate taken when no robot components were present and when the robot was active in the scanner (right).

Co-registration of the robot to the scanner was performed in a 3T GE scanner using the tracking fiducial described in Section 3.6.2.2 that is shown in Fig. 3.12. Under idealized condition, images of the robot's tracking fiducial can provide the location of the robot base in the scanner's coordinate system with an RMS accuracy of $0.14mm$ and 0.37^o as

described in [140]. In practice, where image quality, field of view, and fiducial location are not optimal, the achieved localization accuracy of the robot base can be significantly worse. During one trial, registration accuracy was $3mm$ and 1.0^o as described in [142]. Therefore, imaging configuration and component placement are critical factors in ensuring adequate robot localization in the scanner.

The joint encoders on the robot allow the end effector position and orientation to be determined with respect to the robot. The end effector localization accuracy is nonlinear due to the mechanism design; based on encoder resolution, the worst case resolution for link localization for the horizontal and vertical motions is $0.01mm$ and $0.1mm$ respectively. The overall accuracy of needle tip localization with respect to the MR images is better than $0.25mm$ and 0.5^o.

3.7.3.1 System Workflow

The workflow for the system mimics that of traditional TRUS-guided prostate needle insertions, and are as follows:

1. Acquire pre-procedural MRI volume of the patient's prostate and surrounding anatomy.

2. Select specific needle tip targets as shown in Fig. 3.41.

3. Define corresponding needle trajectories.

4. Acquire an MR image of the robot's tracking fiducial.

5. Register the robotic system to patient/scanner coordinates.

6. Load the biopsy needle or pre-loaded brachytherapy needle into the robot's needle driver.

7. Send coordinates in patient coordinates to the robot.

8. Automatically align the needle guide and lock in place.

9. Manually insert the needle along prescribed axis as virtual needle guide is displayed on real-time MR images intersecting the needle axis.

10. Confirm correct placement.

11. Harvest tissue or deliver therapy.

12. Retract the needle guide and remove biopsy or brachytherapy needle from robot.

13. Update surgical plan as necessary based on volumetric imaging of the prostate and knowledge of the intervention performed.

14. Repeat for as many needles as necessary.

3.7.3.2 Full System Assessment

Evaluation of the complete system is a collaborative effort with colleagues at the Brigham and Women's Hospital (BWH). BWH was primarily responsible for implementing the 3D slicer planning software, real-time scanner control, and integration of the Z-frame

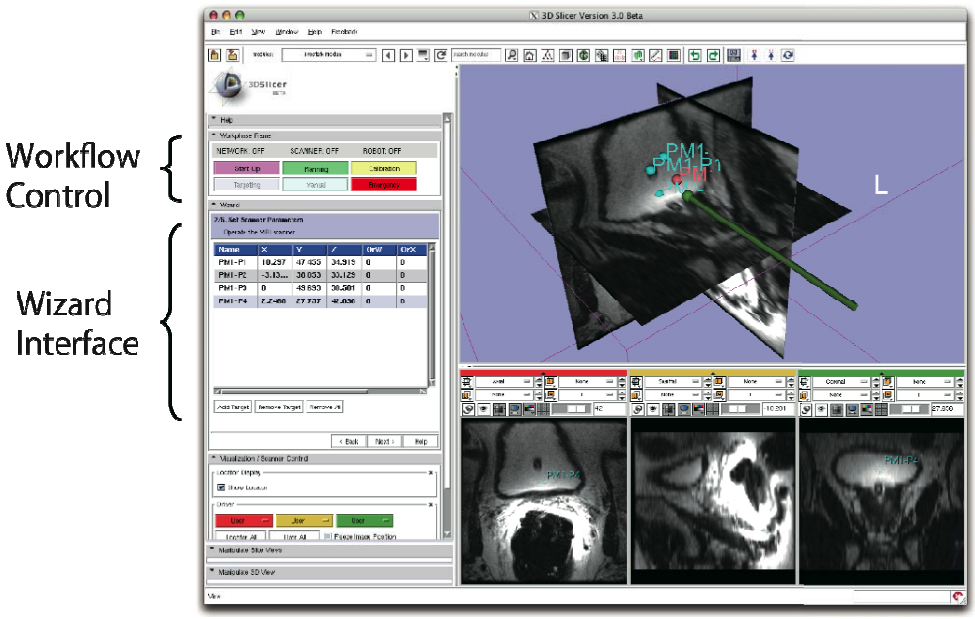

Figure 3.41: 3D Slicer prostate module planning an intervention. The target points are selected, coordinates are transferred to the robot, and the robot moves as the virtual needle guide updates in real time.

registration algorithms. Evaluation experiments were performed in a 3T GE MRI scanner at BWH.

To validate the workflow, five needle insertions were performed in a gel phantom according to the configuration shown in Fig. 3.44. The robot was registered to the scanner using the Z-frame fiducial as described in Section 3.6.2.2. Planning images were acquired of the phantom and targets selected as shown in Fig. 3.41. Target location and Z-frame fiducial location were sent to the robot in the scanner's RAS coordinates (i.e patient coordinate system). The robot then calculated the required joint positions. When commanded to do so, the robot aligned the needle with real-time feedback of the needle position overlaid on the planning software as shown in Fig. 3.42 (left). The needle is inserted along the

given axis while the encoded needle guide provide real-time feedback of tip position in the 3D slicer interface. Fig. 3.42 (center) shows the view as the needle hits the target; the line represents the reported needle axis and the sphere represents the reported tip location based on the inverse kinematics of the robot. The image in Fig. 3.42 (right) shows a confirmation as an MR volume is acquired after the insertion and the needle is overlaid.

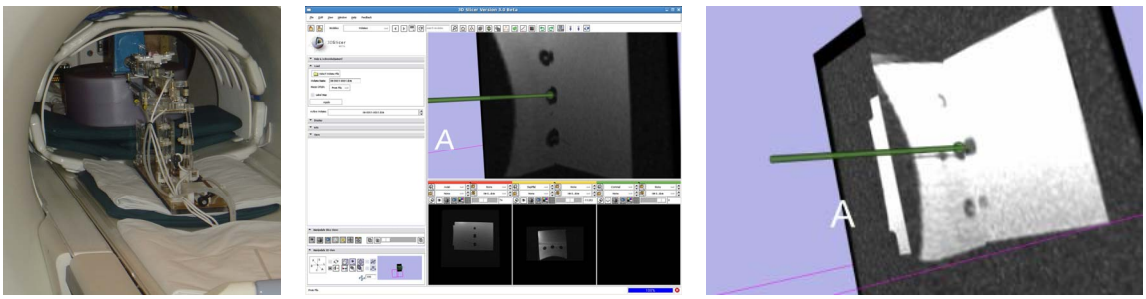

Figure 3.42: Confirmation of needle insertion in phantom study. Robot performing needle insertion in phantom (left), display showing reported needle position on planning images (center), and reported needle position overlaid on confirmation image volume (right).

Initial validation of the system involved performing five needle insertions into phantoms. $10mm$ beads were implanted into a gel phantom and used as targets. All of the five attempts successfully resulted in the needle contacting the target. The image artifact in the confirmation image of Fig. 3.42 (right) aligned with the needle represents the actual axis (less any MR image related distortion) of one of these attempts. Errors in registration manifest themselves as offsets between the reported needle axis and the imaged location. The needle tip shown in the figure clearly approaches the target as seen in cross-sectional images. As described in Section 3.7.2, the robot alone in free space has shown to be capable of accuracies of $1mm$. Needle deflection and external loads on robot were not significant

sources of error in these trials; the limiting factor was registration accuracy of the Z-frame fiducial relating the robot's base position and orientation to the scanner's coordinate system.

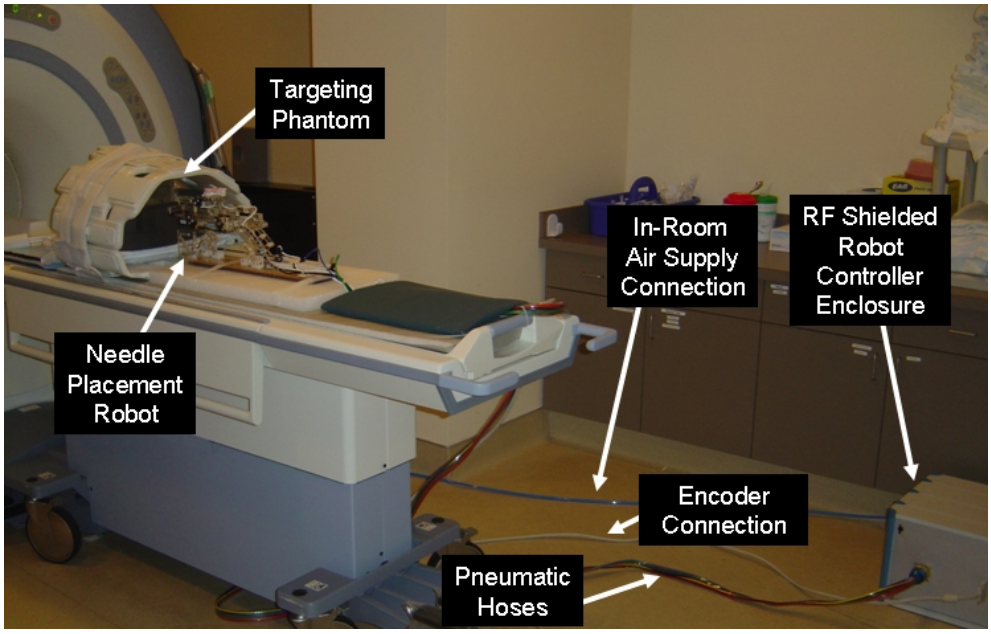

Figure 3.43: Configuration of robot for system evaluation trials. The robot resides on the table at a realistic relative position to the phantom. The controller operates in the room at a distance of $3m$ from the 3T MRI scanner without functional difficulties or significant image quality degradation.

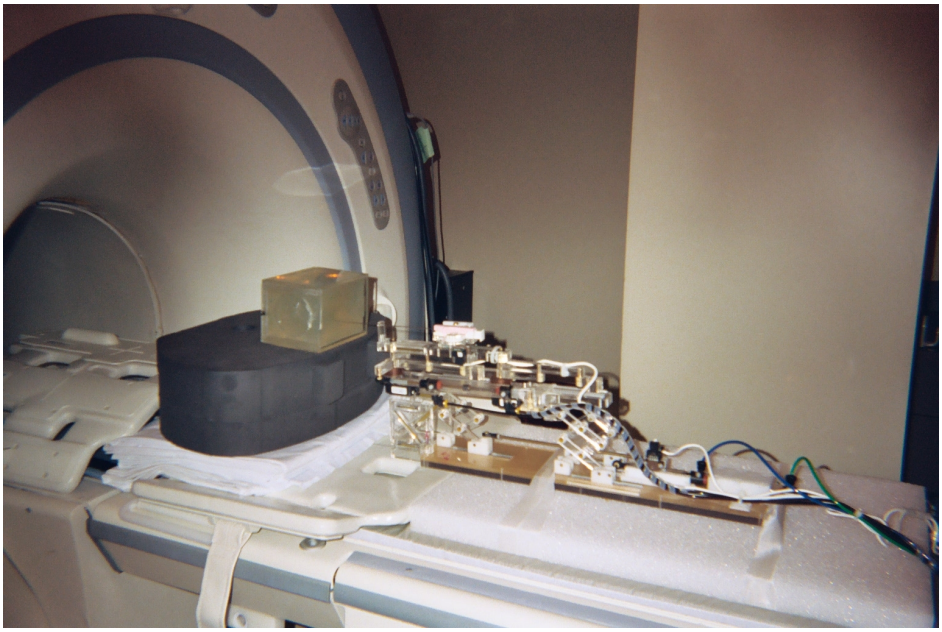

Figure 3.44: Robotic system performing a needle insertion into a phantom in preliminary workflow evaluation experiments. Five out of five $1cm$ targets were successfully targeted.

3.8 Discussion

A prototype MRI-compatible manipulator and the support system architecture that can be used for needle placement in the prostate for biopsy and brachytherapy procedures has been developed. The robot has been designed such that it operates in the confined space between the patient's legs inside the leg rest in a high-field, closed bore MRI scanner.

Unlike any other attempts at transperineal robotic prostate interventions, the patient is in the semi-lithotomy position. This affords several benefits:

1. Pre-operative imaging corresponds directly to the intra-procedural images.

2. Patient and organ motions are limited.

3. The workflow of the conventional TRUS-guided procedure can be preserved.

The configuration allows the use of diagnostic MRI scanners in interventional procedures; there is no need for open or large bore scanners that often are difficult to come by and sacrifice image quality.

Attaining an acceptable level of MR compatibility required significant experimental evaluation. Several types of actuators including were evaluated including piezoelectric motors and pneumatic cylinder/valve pairs as elaborated upon in Section 3.3.4 and published by Fischer, Krieger, *et al.* [119]. The experiences with piezoelectric motors were not as positive as reported elsewhere in the literature. Although high quality images could be obtained with the system in the room, noticeable noise was present when the motors were running during imaging. This prompted the investigation of pneumatic actuators.

Pneumatic actuators have great potential for MRI-compatible mechatronic systems. Since no electronics are required, they are fundamentally compatible with the MR environment. However, there are several obstacles to overcome. These include: 1) material compatibility which was overcome with custom air cylinders made of glass with graphite pistons, 2) lack of stiffness or instability which was overcome with the development of a pneumatic brake that locks the cylinder's rod during needle insertion, and 3) difficult control which was ameliorated by using high-speed valves and shortening pneumatic hose lengths by designing an MRI-compatible controller. Pneumatic actuation seems to be an ideal solution for this robotic system, and it allows the robot to meet all of the design requirements set forth in Section 3.3.2. Further, MR compatibility of the system including the robot and controller is excellent with no more that a 5% loss in average SNR with the robot operational.

The pneumatic cylinders are controlled using a pair of opposing piezoelectrically actuated pressure regulator valves. Servo control is achieved using sliding mode control algorithms. Positioning accuracy of $0.26mm$ RMS error has been achieved with the cylinder alone over 120 point-to-point moves and $0.23mm$ RMS error for tracking a $20mm$ amplitude, $0.125Hz$ sine wave. With the robot fully connected, positioning accuracy of the robot was measured to be $0.94mm$ RMS error over 120 point-to-point moves. When developing mechatronic systems, it is important to consider both the mechanical and electrical aspects of the system. In this case, a simple mechanical damper applied to the system compensated for the pneumatic valve's lag by slowing down the mechanical system. Since high speed

motion and tracking are not required, and in fact frowned upon in medical applications, this is a reasonable solution to the problem.

The system has been evaluated in a variety of tests. The physical configuration of the robot and controller seems ideal for this procedure. The MR compatibility has shown to be sufficient for anatomical imaging using traditional prostate imaging sequences. Communications between all of the elements including the robot, the low level controller, the planning workstation and the MR scanner real-time imaging interface are in place. Initial phantom studies validated the workflow and the ability to accurately localize the robot and target a lesion.

The primary elements of the system are now in place. the current work focusses on refinement of the control system and interface software. The next phase of this work focuses on generating a clinical-grade system and preparing for Phase-1 clinical trials. The initial application will be prostate biopsy, followed later by brachytherapy seed placement. With the addition of the two rotational DOFs, the design of the manipulator will allow for treatment of patients that may have otherwise been denied such treatment because of contraindications such as significant pubic arch interference. The robot, controller and/or system architecture are generally applicable to other MR-guided robotic applications.

3.8.1 Future Work

All elements of the prototype proof-of-concept system have been developed. The robotic system has been constructed, the controller provides sufficient accuracy, the sys-

tem operates with minimal effect on MR image quality, the robot can be manipulated from the external navigation software, and the workflow appears adequate.

The immediate goal of the system is to further evaluate and optimize the accuracy. The limiting factor at this point is the registration of the robot to the scanner through the use of the Z-frame fiducial. Enhancements to this technique are being investigated, and I intend to pursue other MR-compatible registration techniques - both active an passive.

With regards to the robotic system, the primary limitation of the current prototype as constructed is rigidity. The mechanism is to be reconstructed using stronger materials and joints. While performing the redesign, link lengths will be further optimized to enhance accuracy, stability, and controllability. A more robust version of the design is to be constructed in preparation for pre-clinical trials.

To enhance the capabilities of the system, I intend to develop a mechanism with additional degrees of freedom, a tele-operatively controlled needle driver with a haptic master, and application specific modules for biopsy and brachytherapy.

In the near term, the system will be ready for preliminary animal trials. Clinical trials are anticipated within the coming years.

3.9 Conclusion

The MRI Robot system provides a method for performing image-guided interventions using real-time MRI images from traditional diagnostic, long-bore, high-field magnets to

guide and needle insertion procedures. To date, there has been no system that maintains the workflow of traditional procedures in a compact, reliable and convenient platform while enabling the use of intra-operative MRI. The presented work is the first system to apply a remotely actuated robotic needle placement system in standard closed high-field magnets, optimized for transperineal prostate biopsy and brachytherapy seed placement while maintaining the patient in the traditional semi-lithotomy position.

The system's principal function is accurate needle placement in the prostate for diagnosis and treatment, primarily in the form of biopsy and brachytherapy seed placement respectively. The standard $60mm \times 60mm$ perineal window of TRUS-guided brachytherapy was increased to $100mm \times 100mm$, in order to accommodate patient variability and lateral asymmetries in patient setup. In depth, the workspace extends to $150mm$ superior of the perineal surface. Needle angulation in the sagittal and coronal planes will enable procedure to be performed on many of these patients where brachytherapy is typically contraindicated due to pubic arch interference. The robot is situated upon a manual linear slide that repeatably positions the robot in the access tunnel and allows fast removal for reloading brachytherapy needles or collecting harvested biopsy tissue.

Actuators were evaluated to determine the optimal technology for this system. The MR compatibility of Shinsei, Nanomotion and pneumatic actuators under 1.5T and 3T imaging with controllers placed both inside and outside of the scanner room was evaluated. All techniques demonstrate compatibility in the "off" configuration allowing the use of interleaved imaging and motion. The Shinsei motor did not allow for use during imaging;

the Nanomotion performed with moderate SNR loss. Only the pneumatic actuation induced no significant degradation of image quality in any configuration. Thus, this is the actuator of choice for the robot.

The pneumatic cylinders are controlled using a pair of opposing piezoelectrically actuated pressure regulator valves. Servo control is achieved using sliding mode control algorithms. Positioning accuracy of $0.26mm$ RMS error has been achieved with the cylinder alone over 120 point-to-point moves and $0.23mm$ RMS error for tracking a $20mm$ amplitude, $0.125Hz$ sine wave. With the robot fully connected, positioning accuracy of the robot was measured to be $0.94mm$ RMS error over 120 point-to-point moves. When developing mechatronic systems, it is important to consider both the mechanical and electrical aspects of the system. In this case, a simple mechanical damper applied to the system compensated for the pneumatic valve's lag by slowing down the mechanical system. Since high speed motion and tracking are not required, and in fact frowned upon in medical applications, this is a reasonable solution to the problem.

To evaluate the overall clinical layout, the robot was placed in the bore of a 3T long bore scanner inside of the leg rest with a volunteer. There was adequate room for a patient, the robot was able to maintain its necessary workspace, and image quality showed not significant effect. To validate the workflow, five needle insertions were performed in a gel phantom. The robot was registered to the scanner, planning images were acquired of the phantom and targets selected, target location and Z-frame fiducial location were sent to the robot, the robot calculated the required joint positions and aligned the needle with

real-time feedback of the needle position overlaid on the planning software. The needle is inserted along the given axis while the encoded needle guide provide real-time feedback of tip position in the 3D slicer interface. The needle hit the $10mm$ targets in all five out of five attempts.

Chapter 4

Conclusions

This dissertation discussed topics related to developing interventional assistant devices for MRI. The development of two systems that represent different approaches to the same surgical problem of coupling information and action to perform percutaneous needle placement with MR imaging is described. An overview of this work is presented below with a summary of contributions and lessons learned along the way.

4.1 Summary of Work

4.1.1 MRI Visualization Technologies

The MR Image Overlay presented here proves to be the the first reported clinally feasible system for providing *in-situ* imaging to help guide needle insertion procedures in the MRI scanner room. As part of development of the system, we have: optimized the overlay

system design to generate optically stable images in clinically usable configurations, analyzed sources of error, implemented and evaluated registration techniques, developed and refined a workflow to take advantage of *in-situ* imaging, and evaluated the system. We have performed system accuracy evaluation and cadaver trials for joint arthrography, spine pain management, and pelvic interventions. The MRI Image Overlay system is now awaiting commencement of clinical trials.

4.1.2 Percutaneous Therapy Technique Evaluation

Paramagnetic needle artifact and lack of distinct small targets limits the ability to perform needle placement assessment under MR imaging. Presented is a stand-alone system that has been developed in order to evaluate the efficacy of different needle insertion techniques and surgeon performance. Using electromagnetically tracked needles registered to a specially designed interventional phantom, the system can record and compare needle tip placement accuracies and insertion trajectories to a surgical plan. We have performed a preliminary study with several interventional radiologists evaluating needle insertion accuracy, learning curve, and other factors for different insertion technique. A new user-friendly, compact version of the system is in development to widen the appeal of the training environment.

4.1.3 MRI Mechatronic System

The presented robotic system was designed from the ground up for a specific application, and is thus the the first MRI-compatible robot that maintains the workflow of traditional procedures in a compact, reliable and convenient platform while enabling the use of intra-operative MRI. Presented here is the development of an entire surgical robotic system for prostate needle insertion under MR imaging including: thorough evaluation of the workflow, development and evaluation of MR-compatible sensors and actuators, design, modeling, and analysis of the robotic device, construction of the mechanism, and confirmation of the MR compatibility of the robot and individual components.

The primary contribution is greater than the specific design presented; it is the thorough evaluation and development of techniques for developing application-specific robotic systems for operation in MRI. The sensors, actuators, controller, and software developed and evaluated are all generally applicable to MRI-guided robotic interventions.

4.1.4 MRI Robot Controller

The controller developed here is the first available for controlling a robotic system from entirely within an MRI scanner room. The MRI-compatible controller was designed, manufactured, and thoroughly evaluated for utility and compatibility. The development included: construction of the controller hardware, development of low level interface software, implementation of a high precision pneumatic servo controller, and evaluation of controller

accuracy.

The controller developed here is not only suited for the current application, but is generally applicable to MR-guided robotic system including interventional systems, haptic devices, and precisely controlled phantoms.

4.1.5 MRI Robot System Architecture

This is the first fully integrated system that makes conventional diagnostic closed high-field MRI scanners available for guiding prostatic needle placement interventions. The primary components of the presented work are: analysis of the requirements, development of the mechatronic device, development of the low level controller hardware and software, implementation of communication and visualization software, assessment and optimization of the system workflow, confirmation of MR compatibility, and evaluation of accuracy and clinical usability.

The ability to accurately biopsy or implant seeds exactly as planned is a direct benefit to patients receiving the over 1 million prostate biopsies and over 40,000 brachytherapies performed in the US annually. By enabling dexterous, high precision needle placement with online dosimetry will allow larger patient population to be treated and ultimately be treated with better outcomes. Due to the placement accuracy and real-time MR visualization, the system enables for the first time the ability to truly evaluate diagnosis and treatment paradigms. The integrated system proposed here is directly extensible to other imaging configurations in MRI, other imaging modalities and other organ systems.

4.2 Impact and Future Work

The field of MRI-compatible robots and interventional systems is just beginning to blossom as the broader field of medical robotics did two decades ago. When prostatic and other interventions are performed directly in an MRI scanner, accuracy can be increased by avoiding multi-modality image fusion, needle deflection and prostate deformation can be compensated for based on real-time volumetric imaging, and dosimetry can be performed in real time. Further, for the first time, biopsy and brachytherapy procedures can be performed exactly as planned, thus enabling previously infeasible studies on the efficacy of treatment plans.

With the interventional system in 'biopsy mode", we can enable validation of an endless spectrum of prostate MR imaging hypotheses by precise sampling of tissue at selected image points. MR image findings can be directly correlated with pathology. This will enable previously impossible scientific studies into new MR image-based techniques for diagnosis or prostate cancer.

Performing needle insertion under MR imaging opens up the doors to many possibilities. MRI's broad spectrum of imaging options including spectroscopy, oxygenation, thermometry, diffusion, and flow can be incorporated into the Intraoperative plan. As more evidence is presented that MR based detection of suspicious lesions comes forward [143, 144, 145, 146, 147], the ability to directly and definitively target these locations for diagnosis (i.e. biopsy) or therapy (i.e. brachytherapy seed placement, thermal or ultrasonic ablation, cryogenic ablation, chemical therapy, or others) will become invaluable.

The integrated system proposed here is directly extensible to other imaging configurations in MRI, other imaging modalities and other organ systems.

The potential societal benefit of this research is, as MRI is becoming gradually more affordable, simple and robust needle placement mechanisms may facilitate a wide array of diagnostic and therapeutic interventions in the management of prostate cancer and beyond. New ablative therapies (radiofrequency, focused ultrasound, microwave), cryotherapy, and targeted tissue characterization probes (optical spectroscopy, optical tomography, molecular imaging probes, etc.) will become available in the near future and could be enhanced by the accurate image guidance and flexibility of the proposed system. Upon straightforward modifications, the system can be directly translatable to percutaneous needle placement procedures in other soft tissue targets.

Effective, simple, and affordable guidance systems could provide greater access for patients in average care facilities where complicated minimally invasive image-guided procedures are not often performed today. This technique may also reduce variability among practitioners and speed up their learning curve. These devices may also serve as a validation tools for researchers whose work requires minimally invasive percutaneous conduit to anatomical targets identified by MR imaging. By developing systems for MRI, the devices developed are identically usable with any tomographic imaging modality: MRI, CT, PET, SPECT, and any combination thereof.

4.3 Dissertation Contributions

The major contributions of this dissertation are as follows.

- We have developed several techniques for approaching MRI-guided percutaneous interventions. The Image Overlay and the MRI Robot were constructed and evaluated. The evaluation yields insight into the suitability of the technologies for specific applications.

- We have shown the feasibility of an MR-compatible, pneumatically actuated robotic system. The evaluation and selection of sensors, actuators, and display technologies serves as a guide for future related work.

- We have fully developed a modular MRI-compatible controller that is generally applicable to controlling and interfacing with mechatronic devices in the MRI scanner.

4.4 Lessons Learned

Probably the most important lesson to come out of this work is *...know your application*! There is a clear need for robotic systems, but in many cases there may be simpler solutions that provide significantly greater clinical benefit. The systems described here present an excellent contrast of the spectrum of computer assisted interventions as shown in Fig. 4.1. When real-time imaging is not strictly necessary, a simple needle virtual guide such as the image overlay or laser guide is sufficient to have a significant benefit without

requiring an engineering entourage. In fact, this system has received such positive feedback that it will be entering clinical trials shortly. On the other end of the spectrum are the "point-and-click" robotic surgery systems. In the case of prostate biopsy or brachytherapy, there is no way to accurately perform the intervention without real-time imaging. And, due to the quality of the images, high-field MRI is an ideal modality. Because of the strong spatial constraints of a long bore magnet, this is therefore an ideal application for an in-bore robotic system. The first step of developing any interventional system, and one that is all to often not given enough consideration, is through analysis of the requirements. The work here describes everything from a simple handheld protractor up through a fully integrated robotic system, and the hardest question is determining where on that spectrum the optimal system design lies.

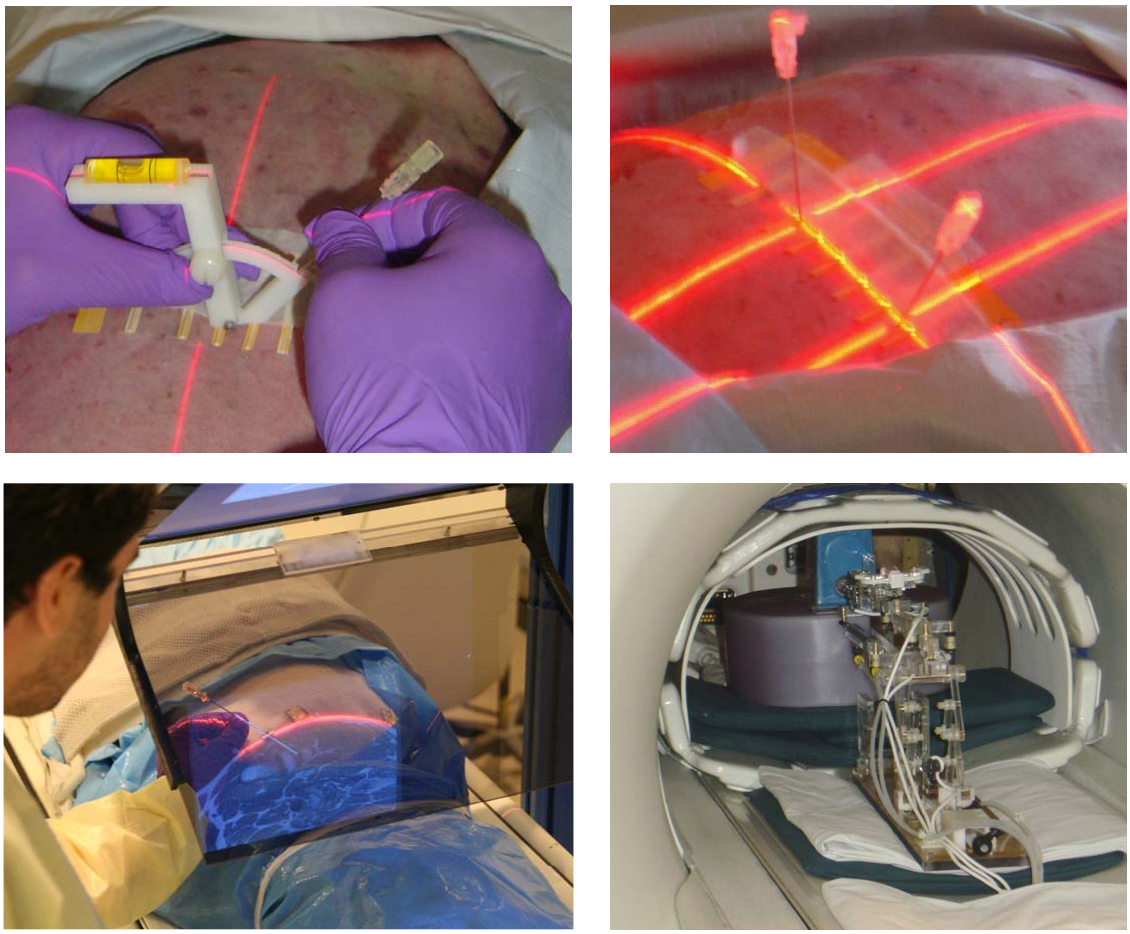

Figure 4.1: The spectrum of needle insertion techniques developed during the course of this research. Handheld protractor (top-left), bi-plane laser guide (top-right), image overlay (bottom-left), and "point-and-click" robotic (bottom-right).

Bibliography

[1] T. Peters and K. Cleary, Eds., *Image-Guided Interventions: Technology and Applications*. Springer, 2008.

[2] V. Horsley and R. Clarke, "The structure and functions of the cerebellum examined by a new method," *Brain*, vol. 31, pp. 45–124, 1908.

[3] P. J. Kelly, B. A. Kall, S. Goerss, and F. Earnest, "Computer-assisted stereotaxic laser resection of intra-axial brain neoplasms." *J Neurosurg*, vol. 64, no. 3, pp. 427–439, Mar 1986.

[4] A. L. Benabid, P. Cinquin, S. Lavalle, J. F. L. Bas, J. Demongeot, and J. de Rougemont, "Computer-driven robot for stereotactic surgery connected to ct scan and magnetic resonance imaging. technological design and preliminary results." *Appl Neurophysiol*, vol. 50, no. 1-6, pp. 153–154, 1987.

[5] Y. Kwoh, J. Hou, E. Jonckheere, and S. Hayati, "A robot with improved absolute positioning accuracy for ct guided stereotactic brain surgery," *IEEE J BME*, vol. 35, no. 2, pp. 153–160, 1988.

[6] R. Taylor, H. Paul, B. Mittelstadt, E. Glassman, B. Musits, and W. Bargar, "Robotic total hip replacement surgery in dogs," in *Proc. Annual International Conference of the IEEE Engineering in Engineering in Medicine and Biology Society*, H. Paul, Ed., 1989, pp. 887–889 vol.3.

[7] P. Kazanzides, B. Mittelstadt, B. Musits, W. Bargar, J. Zuhars, B. Williamson, P. Cain, and E. Carbone, "An integrated system for cementless hip replacement," *IEEE Engineering in Medicine and Biology*, vol. 14, no. 3, pp. 307–313, 1995.

[8] B. L. Davies, R. D. Hibberd, M. J. Coptcoat, and J. E. Wickham, "A surgeon robot prostatectomy–a laboratory evaluation." *J Med Eng Technol*, vol. 13, no. 6, pp. 273–277, 1989.

[9] S. J. Harris, F. Arambula-Cosio, Q. Mei, R. D. Hibberd, B. L. Davies, J. E. Wickham, M. S. Nathan, and B. Kundu, "The probot–an active robot for prostate resection." *Proc Inst Mech Eng [H]*, vol. 211, no. 4, pp. 317–325, 1997.

[10] R. Taylor, J. Funda, B. Eldridge, S. Gomory, K. Gruben, D. LaRose, M. Talamini, L. Kavoussi, and J. Anderson, "A telerobotic assistant for laparoscopic surgery," *IEEE Engineering in Medicine and Biology*, vol. 14, no. 3, pp. 279–288, 1995.

[11] S. Schreiner, J. H. Anderson, R. H. Taylor, J. Funda, A. Bzostek, and A. C. Barnes, "A system for percutaneous delivery of treatment with a fluoroscopically-guided robot," in *CVRMed-MRCAS '97: Proceedings of the First Joint Conference on Com-*

puter Vision, Virtual Reality and Robotics in Medicine and Medial Robotics and Computer-Assisted Surgery. London, UK: Springer-Verlag, 1997, pp. 747–756.

[12] R. H. Taylor, P. Jensen, L. L. Whitcomb, A. Barnes, R. Kumar, D. Stoianovici, P. Gupta, Z. Wang, E. Dejuan, and L. Kavoussi, "A steady-hand robotic system for microsurgical augmentation," *The International Journal of Robotics Research*, vol. 18, no. 12, pp. 1201–1210, 1999.

[13] K. Masamune, G. Fichtinger, A. Patriciu, R. C. Susil, R. H. Taylor, L. R. Kavoussi, J. H. Anderson, I. Sakuma, T. Dohi, and D. Stoianovici, "System for robotically assisted percutaneous procedures with computed tomography guidance." *Comput Aided Surg*, vol. 6, no. 6, pp. 370–383, 2001. [Online]. Available: http://dx.doi.org/10.1002/igs.10024

[14] R. H. Taylor and D. Stoianovici, "Medical robotics in computer-integrated surgery," *IEEE Trans RA*, vol. 19, no. 5, pp. 765–781, Oct. 2003.

[15] K. Cleary, A. Melzer, V. Watson, G. Kronreif, and D. Stoianovici, "Interventional robotic systems: applications and technology state-of-the-art." *Minim Invasive Ther Allied Technol*, vol. 15, no. 2, pp. 101–113, 2006. [Online]. Available: http://dx.doi.org/10.1080/13645700600674179

[16] B. Davies, "A review of robotics in surgery." *Proc Inst Mech Eng [H]*, vol. 214, no. 1, pp. 129–140, 2000.

[17] R. D. Howe and Y. Matsuoka, "Robotics for surgery." *Annu Rev Biomed Eng*, vol. 1, pp. 211–240, 1999. [Online]. Available: http://dx.doi.org/10.1146/annurev.bioeng.1.1.211

[18] P. Dario, E. Guglielmelli, B. Allotta, and M. Carrozza, "Robotics for medical applications," *IEEE Robotics & Automation Magazine*, vol. 3, no. 3, pp. 44–56, 1996.

[19] F. A. Jolesz, "Interventional and intraoperative mri: a general overview of the field." *J Magn Reson Imaging*, vol. 8, no. 1, pp. 3–7, 1998.

[20] F. A. Jolesz, I. F. Talos, R. B. Schwartz, H. Mamata, D. F. Kacher, K. Hynynen, N. McDannold, P. Saivironporn, and L. Zao, "Intraoperative magnetic resonance imaging and magnetic resonance imaging-guided therapy for brain tumors." *Neuroimaging Clin N Am*, vol. 12, no. 4, pp. 665–683, Nov 2002.

[21] L. Lenchik, D. J. Dovgan, and R. Kier, "Ct of the iliopsoas compartment: value in differentiating tumor, abscess, and hematoma." *AJR Am J Roentgenol*, vol. 162, no. 1, pp. 83–86, Jan 1994.

[22] E. Salomonowitz, "Mr imaging-guided biopsy and therapeutic intervention in a closed-configuration magnet: single-center series of 361 punctures." *AJR Am J Roentgenol*, vol. 177, no. 1, pp. 159–163, Jul 2001.

[23] M. Moche, R. Trampel, T. Kahn, and H. Busse, "Navigation concepts for mr

image-guided interventions." *J Magn Reson Imaging*, vol. 27, no. 2, pp. 276–291, Feb 2008. [Online]. Available: http://dx.doi.org/10.1002/jmri.21262

[24] S. G. Nour and J. S. Lewin, "Percutaneous biopsy from blinded to mr guided: an update on current techniques and applications." *Magn Reson Imaging Clin N Am*, vol. 13, no. 3, pp. 441–464, Aug 2005. [Online]. Available: http://dx.doi.org/10.1016/j.mric.2005.04.009

[25] J. S. Lewin, S. G. Nour, and J. L. Duerk, "Magnetic resonance image-guided biopsy and aspiration." *Top Magn Reson Imaging*, vol. 11, no. 3, pp. 173–183, Jun 2000.

[26] C. A. Petersilge, J. S. Lewin, J. L. Duerk, and S. F. Hatem, "Mr arthrography of the shoulder: rethinking traditional imaging procedures to meet the technical requirements of mr imaging guidance." *AJR Am J Roentgenol*, vol. 169, no. 5, pp. 1453–1457, Nov 1997.

[27] R. Fahrig, K. Butts, J. A. Rowlands, R. Saunders, J. Stanton, G. M. Stevens, B. L. Daniel, Z. Wen, D. L. Ergun, and N. J. Pelc, "A truly hybrid interventional mr/x-ray system: feasibility demonstration." *J Magn Reson Imaging*, vol. 13, no. 2, pp. 294–300, Feb 2001.

[28] K. F. Kreitner, R. Loew, M. Runkel, J. Zollner, and M. Thelen, "Low-field mr arthrography of the shoulder joint: technique, indications, and clinical results." *Eur Radiol*, vol. 13, no. 2, pp. 320–329, Feb 2003. [Online]. Available: http://dx.doi.org/10.1007/s00330-002-1665-y

[29] W. Birkfellner, M. Figl, K. Huber, F. Watzinger, F. Wanschitz, J. Hummel, R. Hanel, W. Greimel, P. Homolka, R. Ewers, and H. Bergmann, "A head-mounted operating binocular for augmented reality visualization in medicine–design and initial evaluation." *IEEE Trans Med Imaging*, vol. 21, no. 8, pp. 991–997, Aug 2002.

[30] F. K. Wacker, S. Vogt, A. Khamene, J. A. Jesberger, S. G. Nour, D. R. Elgort, F. Sauer, J. L. Duerk, and J. S. Lewin, "An augmented reality system for mr image-guided needle biopsy: initial results in a swine model." *Radiology*, vol. 238, no. 2, pp. 497–504, Feb 2006. [Online]. Available: http://dx.doi.org/10.1148/radiol.2382041441

[31] M. Blackwell, C. Nikou, A. M. DiGioia, and T. Kanade, "An image overlay system for medical data visualization." *Med Image Anal*, vol. 4, no. 1, pp. 67–72, Mar 2000.

[32] S. Nakajima, K. Nakamura, K. Masamune, I. Sakuma, and T. Dohi, "Three-dimensional medical imaging display with computer-generated integral photography." *Comput Med Imaging Graph*, vol. 25, no. 3, pp. 235–241, 2001.

[33] A. Khamene, F. Wacker, S. Vogt, F. Azar, M. Wendt, F. Sauer, and J. Lewin, "An augmented reality system for mri-guided needle biopsies." *Stud Health Technol Inform*, vol. 94, pp. 151–157, 2003.

[34] R. A. Kockro, L. Serra, Y. Tseng-Tsai, C. Chan, S. Yih-Yian, C. Gim-Guan, E. Lee, L. Y. Hoe, N. Hern, and W. L. Nowinski, "Planning and simulation of neurosurgery

in a virtual reality environment." *Neurosurgery*, vol. 46, no. 1, pp. 118–35; discussion 135–7, Jan 2000.

[35] W. L. Grimson, G. J. Ettinger, S. J. White, T. Lozano-Perez, W. M. Wells, and R. Kikinis, "An automatic registration method for frameless stereotaxy, image guided surgery, and enhanced reality visualization." *IEEE Trans Med Imaging*, vol. 15, no. 2, pp. 129–140, 1996. [Online]. Available: http://dx.doi.org/10.1109/42.491415

[36] H. Iseki, Y. Masutani, M. Iwahara, T. Tanikawa, Y. Muragaki, T. Taira, T. Dohi, and K. Takakura, "Volumegraph (overlaid three-dimensional image-guided navigation). clinical application of augmented reality in neurosurgery." *Stereotact Funct Neurosurg*, vol. 68, no. 1-4 Pt 1, pp. 18–24, 1997.

[37] N. V. Tsekos, A. Khanicheh, E. Christoforou, and C. Mavroidis, "Magnetic resonance-compatible robotic and mechatronics systems for image-guided interventions and rehabilitation: a review study." *Annu Rev Biomed Eng*, vol. 9, pp. 351–387, 2007. [Online]. Available: http://dx.doi.org/10.1146/annurev.bioeng.9.121806.160642

[38] H. Elhawary, A. Zivanovic, B. Davies, and M. Lamprth, "A review of magnetic resonance imaging compatible manipulators in surgery." *Proc Inst Mech Eng [H]*, vol. 220, no. 3, pp. 413–424, Apr 2006.

[39] K. Masamune, E. Kobayashi, Y. Masutani, M. Suzuki, T. Dohi, H. Iseki, and

K. Takakura, "Development of an mri-compatible needle insertion manipulator for stereotactic neurosurgery." *J Image Guid Surg*, vol. 1, no. 4, pp. 242–248, 1995. [Online]. Available: http://dx.doi.org/3.0.CO;2-A

[40] A. Felden, J. Vagner, A. Hinz, H. Fischer, S. O. R. Pfleiderer, J. R. Reichenbach, and W. A. Kaiser, "Robitom-robot for biopsy and therapy of the mamma." *Biomed Tech (Berl)*, vol. 47 Suppl 1 Pt 1, pp. 2–5, 2002.

[41] K. Chinzei, N. Hata, F. A. Jolesz, and R. Kikinis, "Mri compatible surgical assist robot: System integration and preliminary feasibility study," in *MICCAI*, vol. 1935, October 2000, pp. 921–930.

[42] K. Chinzei and K. Miller, "Towards mri guided surgical manipulator." *Med Sci Monit*, vol. 7, no. 1, pp. 153–163, 2001.

[43] A. Krieger, R. C. Susil, C. Mnard, J. A. Coleman, G. Fichtinger, E. Atalar, and L. L. Whitcomb, "Design of a novel mri compatible manipulator for image guided prostate interventions." *IEEE Trans Biomed Eng*, vol. 52, no. 2, pp. 306–313, Feb 2005. [Online]. Available: http://dx.doi.org/10.1109/TBME.2004.840497

[44] N. V. Tsekos, A. Ozcan, and E. Christoforou, "A prototype manipulator for magnetic resonance-guided interventions inside standard cylindrical magnetic resonance imaging scanners." *J Biomech Eng*, vol. 127, no. 6, pp. 972–980, Nov 2005.

[45] G. R. Sutherland, I. Latour, A. D. Greer, T. Fielding, G. Feil, and P. Newhook,

"An image-guided magnetic resonance-compatible surgical robot." *Neurosurgery*, vol. 62, no. 2, pp. 286–92; discussion 292–3, Feb 2008. [Online]. Available: http://dx.doi.org/10.1227/01.neu.0000315996.73269.18

[46] D. Stoianovici, "Multi-imager compatible actuation principles in surgical robotics." *Int J Med Robot*, vol. 1, no. 2, pp. 86–100, Jan 2005. [Online]. Available: http://dx.doi.org/10.1002/rcs.19

[47] H. Elhawary, A. Zivanovic, M. Rea, Z. T. H. Tse, D. McRobbie, I. Young, M. Paley, B. Davies, and M. Lamprth, "A mr compatible mechatronic system to facilitate magic angle experiments in vivo." *Med Image Comput Comput Assist Interv Int Conf Med Image Comput Comput Assist Interv*, vol. 10, no. Pt 2, pp. 604–611, 2007.

[48] E. Taillant, J. Avila-Vilchis, C. Allegrini, I. Bricault, and P. Cinquin, "Ct and mr compatible light puncture robot: Architectural design and first experiments," in *Med Image Comput Comput Assist Interv Int Conf Med Image Comput Comput Assist Interv*, vol. 3217, Sept. 2004, pp. 145–152.

[49] S. Zangos, C. Herzog, K. Eichler, R. Hammerstingl, A. Lukoschek, S. Guthmann, B. Gutmann, U. J. Schoepf, P. Costello, and T. J. Vogl, "Mr-compatible assistance system for punction in a high-field system: device and feasibility of transgluteal biopsies of the prostate gland." *Eur Radiol*, vol. 17, no. 4, pp. 1118–1124, Apr 2007. [Online]. Available: http://dx.doi.org/10.1007/s00330-006-0421-0

[50] R. Gassert, R. Moser, E. Burdet, and H. Bleuler, "Mri/fmri-compatible robotic sys-

tem with force feedback for interaction with human motion," *IEEE Trans Mech*, vol. 11, no. 2, pp. 216–224, April 2006.

[51] J. Virtanen, "Developing mr-compatible robots sensor technology," *Symposium on Machine Design*, vol. 120, pp. 107–120, June 2003.

[52] M. Tada and T. Kanade, "Design of an mr-compatible three-axis force sensor," in *Proc. IEEE/RSJ International Conference on Intelligent Robots and Systems (IROS 2005)*, 2–6 Aug. 2005, pp. 3505–3510.

[53] T. Suzuki, H. Liao, E. Kobayashi, and I. Sakuma, "Ultrasonic motor driving method for emi-free image in mr image-guided surgical robotic system," in *Proc. IEEE/RSJ International Conference on Intelligent Robots and Systems IROS 2007*, Oct. 29 2007–Nov. 2 2007, pp. 522–527.

[54] H. Elhawary, A. Zivanovic, M. Rea, B. Davies, C. Besant, D. McRobbie, N. de Souza, I. Young, and M. Lamprth, "The feasibility of mr-image guided prostate biopsy using piezoceramic motors inside or near to the magnet isocentre." *Med Image Comput Comput Assist Interv Int Conf Med Image Comput Comput Assist Interv*, vol. 9, no. Pt 1, pp. 519–526, 2006.

[55] J. Vogan, A. Wingert, J.-S. Plante, S. Dubowsky, M. Hafez, D. Kacher, and F. Jolesz, "Manipulation in mri devices using electrostrictive polymer actuators: with an application to reconfigurable imaging coils," in *Proc. IEEE International Conference on Robotics and Automation ICRA '04*, vol. 3, Apr 26–May 1, 2004, pp. 2498–2504.

[56] K. Tadakuma, L. DeVita, S. Y., and S. Dubowsky, "The experimental study of a precision parallel manipulator with binary actuation: With application to mri cancer treatment," in *Proc. IEEE International Conference on Robotics and Automation ICRA '08*, May 21–May 23, 2008, pp. 2503–2508.

[57] J. Carrino, D. Smith, and M. Schweitzer, "Mr arthrography of the elbow and wrist." *Semin Musculoskelet Radiol*, vol. 2, no. 4, pp. 397–414, 1998.

[58] L. S. Steinbach, W. E. Palmer, and M. E. Schweitzer, "Special focus session. mr arthrography." *Radiographics*, vol. 22, no. 5, pp. 1223–1246, 2002.

[59] G. Schulte-Altedorneburg, M. Gebhard, W. A. Wohlgemuth, W. Fischer, J. Zentner, R. Wegener, T. Balzer, and K. Bohndorf, "Mr arthrography: pharmacology, efficacy and safety in clinical trials." *Skeletal Radiol*, vol. 32, no. 1, pp. 1–12, Jan 2003. [Online]. Available: http://dx.doi.org/10.1007/s00256-002-0595-8

[60] R. Schmitt, G. Christopoulos, R. Meier, G. Coblenz, S. Frhner, U. Lanz, and H. Krimmer, "Direct mr arthrography of the wrist in comparison with arthroscopy: a prospective study on 125 patients," *Rofo*, vol. 175, no. 7, pp. 911–919, Jul 2003. [Online]. Available: http://dx.doi.org/10.1055/s-2003-40434

[61] C. A. Binkert, F. R. Verdun, M. Zanetti, C. W. Pfirrmann, and J. Hodler, "Ct arthrography of the glenohumeral joint: Ct fluoroscopy versus conventional ct and fluoroscopy–comparison of image-guidance techniques." *Radiology*, vol. 229,

no. 1, pp. 153–158, Oct 2003. [Online]. Available: http://dx.doi.org/10.1148/radiol.2291020314

[62] P. R. Hilfiker, D. Weishaupt, M. Schmid, B. Dubno, J. Hodler, and J. F. Debatin, "Real-time mr-guided joint puncture and arthrography: preliminary results." *Eur Radiol*, vol. 9, no. 2, pp. 201–204, 1999.

[63] R. Ojala, R. Klemola, J. Karppinen, R. B. Sequeiros, and O. Tervonen, "Sacroiliac joint arthrography in low back pain: feasibility of mri guidance." *Eur J Radiol*, vol. 40, no. 3, pp. 236–239, Dec 2001.

[64] A. C. Zoga and M. E. Schweitzer, "Indirect magnetic resonance arthrography: applications in sports imaging." *Top Magn Reson Imaging*, vol. 14, no. 1, pp. 25–33, Feb 2003.

[65] D. Bergin and M. E. Schweitzer, "Indirect magnetic resonance arthrography." *Skeletal Radiol*, vol. 32, no. 10, pp. 551–558, Oct 2003. [Online]. Available: http://dx.doi.org/10.1007/s00256-003-0669-2

[66] S. Trattnig, M. Breitenseher, M. Pretterklieber, G. Kontaxis, T. Rand, T. Helbich, and H. Imhof, "Mr-guided joint puncture and real-time mr-assisted contrast media application." *Acta Radiol*, vol. 38, no. 6, pp. 1047–1049, Nov 1997.

[67] S. Trattnig, M. Breitenseher, T. Rand, A. Ba-ssalamah, S. Schick, H. Imhof, and C. A. Petersilge, "Mr imaging-guided mr arthrography of the shoulder: clinical ex-

perience on a conventional closed high-field system." *AJR Am J Roentgenol*, vol. 172, no. 6, pp. 1572–1574, Jun 1999.

[68] A. Jemal, R. Siegel, E. Ward, Y. Hao, J. Xu, T. Murray, and M. J. Thun, "Cancer statistics, 2008." *CA Cancer J Clin*, vol. 58, no. 2, pp. 71–96, 2008. [Online]. Available: http://dx.doi.org/10.3322/CA.2007.0010

[69] J. C. Blasko, T. Mate, J. E. Sylvester, P. D. Grimm, and W. Cavanagh, "Brachytherapy for carcinoma of the prostate: techniques, patient selection, and clinical outcomes." *Semin Radiat Oncol*, vol. 12, no. 1, pp. 81–94, Jan 2002. [Online]. Available: http://dx.doi.org/10.1053/srao.2002.28667

[70] M. R. Cooperberg, D. P. Lubeck, M. V. Meng, S. S. Mehta, and P. R. Carroll, "The changing face of low-risk prostate cancer: trends in clinical presentation and primary management." *J Clin Oncol*, vol. 22, no. 11, pp. 2141–2149, Jun 2004. [Online]. Available: http://dx.doi.org/10.1200/JCO.2004.10.062

[71] J. C. Presti, "Prostate cancer: assessment of risk using digital rectal examination, tumor grade, prostate-specific antigen, and systematic biopsy." *Radiol Clin North Am*, vol. 38, no. 1, pp. 49–58, Jan 2000.

[72] M. K. Terris, E. M. Wallen, and T. A. Stamey, "Comparison of mid-lobe versus lateral systematic sextant biopsies in the detection of prostate cancer." *Urol Int*, vol. 59, no. 4, pp. 239–242, 1997.

[73] P. Blumenfeld, N. Hata, S. DiMaio, K. Zou, S. Haker, G. Fichtinger, and C. M. C. Tempany, "Transperineal prostate biopsy under magnetic resonance image guidance: a needle placement accuracy study." *J Magn Reson Imaging*, vol. 26, no. 3, pp. 688–694, Sep 2007. [Online]. Available: http://dx.doi.org/10.1002/jmri.21067

[74] O. Goksel, S. E. Salcudean, S. P. DiMaio, R. Rohling, and J. Morris, "3d needle-tissue interaction simulation for prostate brachytherapy." *Med Image Comput Comput Assist Interv Int Conf Med Image Comput Comput Assist Interv*, vol. 8, no. Pt 1, pp. 827–834, 2005.

[75] G. Fichtinger, J. Fiene, C. W. Kennedy, G. Kronreif, I. I. Iordachita, D. Y. Song, E. C. Burdette, and P. Kazanzides, "Robotic assistance for ultrasound guided prostate brachytherapy." *Med Image Comput Comput Assist Interv Int Conf Med Image Comput Comput Assist Interv*, vol. 10, no. Pt 1, pp. 119–127, 2007.

[76] Z. Wei, M. Ding, D. Downey, and A. Fenster, "3d trus guided robot assisted prostate brachytherapy." *Med Image Comput Comput Assist Interv Int Conf Med Image Comput Comput Assist Interv*, vol. 8, no. Pt 2, pp. 17–24, 2005.

[77] Y. Yu, T. K. Podder, Y. D. Zhang, W. S. Ng, V. Misic, J. Sherman, D. Fuller, D. J. Rubens, J. G. Strang, R. A. Brasacchio, and E. M. Messing, "Robotic system for prostate brachytherapy." *Comput Aided Surg*, vol. 12, no. 6, pp. 366–370, Nov 2007. [Online]. Available: http://dx.doi.org/10.1080/10929080701746926

[78] S. Adusumilli and E. S. Pretorius, "Magnetic resonance imaging of prostate cancer." *Semin Urol Oncol*, vol. 20, no. 3, pp. 192–210, Aug 2002.

[79] A. V. D'Amico, R. Cormack, C. M. Tempany, S. Kumar, G. Topulos, H. M. Kooy, and C. N. Coleman, "Real-time magnetic resonance image-guided interstitial brachytherapy in the treatment of select patients with clinically localized prostate cancer." *Int J Radiat Oncol Biol Phys*, vol. 42, no. 3, pp. 507–515, Oct 1998.

[80] R. A. Cormack, H. Kooy, C. M. Tempany, and A. V. D'Amico, "A clinical method for real-time dosimetric guidance of transperineal 125i prostate implants using interventional magnetic resonance imaging." *Int J Radiat Oncol Biol Phys*, vol. 46, no. 1, pp. 207–214, Jan 2000.

[81] K. Engelhard, H. P. Hollenbach, B. Kiefer, A. Winkel, K. Goeb, and D. Engehausen, "Prostate biopsy in the supine position in a standard 1.5-t scanner under real time mr-imaging control using a mr-compatible endorectal biopsy device." *Eur Radiol*, vol. 16, no. 6, pp. 1237–1243, Jun 2006. [Online]. Available: http://dx.doi.org/10.1007/s00330-005-0100-6

[82] S. P. DiMaio, S. Pieper, K. Chinzei, N. Hata, S. J. Haker, D. F. Kacher, G. Fichtinger, C. M. Tempany, and R. Kikinis, "Robot-assisted needle placement in open mri: system architecture, integration and validation." *Comput Aided Surg*, vol. 12, no. 1, pp. 15–24, Jan 2007. [Online]. Available: http://dx.doi.org/10.1080/10929080601168254

[83] R. C. Susil, A. Krieger, J. A. Derbyshire, A. Tanacs, L. L. Whitcomb, G. Fichtinger, and E. Atalar, "System for mr image-guided prostate interventions: canine study." *Radiology*, vol. 228, no. 3, pp. 886–894, Sep 2003. [Online]. Available: http://dx.doi.org/283020911

[84] A. Krieger, C. Csoma, I. I. Iordachital, P. Guion, A. K. Singh, G. Fichtinger, and L. L. Whitcomb, "Design and preliminary accuracy studies of an mri-guided transrectal prostate intervention system." *Med Image Comput Comput Assist Interv Int Conf Med Image Comput Comput Assist Interv*, vol. 10, no. Pt 2, pp. 59–67, 2007.

[85] S. Zangos, K. Eichler, K. Engelmann, M. Ahmed, S. Dettmer, C. Herzog, W. Pegios, A. Wetter, T. Lehnert, M. G. Mack, and T. J. Vogl, "Mr-guided transgluteal biopsies with an open low-field system in patients with clinically suspected prostate cancer: technique and preliminary results." *Eur Radiol*, vol. 15, no. 1, pp. 174–182, Jan 2005. [Online]. Available: http://dx.doi.org/10.1007/s00330-004-2458-2

[86] D. Beyersdorff, A. Winkel, B. Hamm, S. Lenk, S. A. Loening, and M. Taupitz, "Mr imaging-guided prostate biopsy with a closed mr unit at 1.5 t: initial results." *Radiology*, vol. 234, no. 2, pp. 576–581, Feb 2005. [Online]. Available: http://dx.doi.org/10.1148/radiol.2342031887

[87] D. Stoianovici, D. Song, D. Petrisor, D. Ursu, D. Mazilu, M. Muntener, M. Mutener, M. Schar, and A. Patriciu, "Mri stealth robot for prostate interventions." *Minim*

Invasive Ther Allied Technol, vol. 16, no. 4, pp. 241–248, 2007. [Online]. Available: http://dx.doi.org/10.1080/13645700701520735

[88] G. S. Fischer, A. Deguet, C. Csoma, R. H. Taylor, L. Fayad, J. A. Carrino, S. J. Zinreich, and G. Fichtinger, "Mri image overlay: application to arthrography needle insertion." *Comput Aided Surg*, vol. 12, no. 1, pp. 2–14, Jan 2007. [Online]. Available: http://dx.doi.org/10.1080/10929080601169930

[89] G. S. Fischer, A. Deguet, D. Schlattman, R. H. Taylor, L. Fayad, S. J. Zinreich, and G. Fichtinger, "Mri image overlay: applications to arthrography needle insertion." *Stud Health Technol Inform*, vol. 119, pp. 150–155, 2006.

[90] G. S. Fischer, I. I. Iordachita, C. Csoma, J. Tokuda, S. P. DiMaio, C. M. Tempany, N. Hata, and G. Fichtinger, "Mri-compatible pneumatic robot for transperineal prostate needle placement," *IEEE/ASME Transactions on Mechatronics*, vol. 13, no. 3, June 2008.

[91] G. S. Fischer, S. P. DiMaio, I. I. Iordachita, and G. Fichtinger, "Robotic assistant for transperineal prostate interventions in 3t closed mri." *Int Conf Med Image Comput Comput Assist Interv*, vol. 10, no. Pt 1, pp. 425–433, 2007.

[92] G. S. Fischer, I. I. Iordachita, C. Csoma, J. Tokuda, P. W. Mewes, C. M. Tempany, N. Hata, and G. Fichtinger, "Pneumatically operated mri-compatible needle placement robot for prostate interventions," in *Proc. IEEE International Conference on Robotics and Automation ICRA 2008*, 2008, pp. 2489–2495.

[93] S. P. DiMaio, G. S. Fischer, S. J. Haker, N. Hata, I. I. Iordachita, C. M. Tempany, R. Kikinis, and G. Fichtinger, "A system for mri-guided prostate interventions," in *Proc. First IEEE/RAS-EMBS International Conference on Biomedical Robotics and Biomechatronics BioRob 2006*, February 20–22, 2006, pp. 68–73.

[94] G. Fichtinger, A. Deguet, G. S. Fischer, I. I. Iordachita, E. Balogh, K. Masamune, R. H. Taylor, L. M. Fayad, M. de Oliveira, and S. J. Zinreich, "Image overlay for ct-guided needle insertions." *Comput Aided Surg*, vol. 10, no. 4, pp. 241–255, Jul 2005. [Online]. Available: http://dx.doi.org/10.1080/10929080500230486

[95] G. Fichtinger, A. Deguet, K. Masamune, E. Balogh, G. S. Fischer, H. Mathieu, R. H. Taylor, S. J. Zinreich, and L. M. Fayad, "Image overlay guidance for needle insertion in ct scanner." *IEEE Trans Biomed Eng*, vol. 52, no. 8, pp. 1415–1424, Aug 2005. [Online]. Available: http://dx.doi.org/10.1109/TBME.2005.851493

[96] G. D. Stetten and V. S. Chib, "Overlaying ultrasonographic images on direct vision." *J Ultrasound Med*, vol. 20, no. 3, pp. 235–240, Mar 2001.

[97] L. Court, I. Rosen, R. Mohan, and L. Dong, "Evaluation of mechanical precision and alignment uncertainties for an integrated ct/linac system." *Med Phys*, vol. 30, no. 6, pp. 1198–1210, Jun 2003.

[98] G. S. Fischer, C. Wamsley, S. J. Zinreich, and G. Fichtinger, "Mri guided needle insertion - comparison of four techniques," *Society for Interventional Radiology 31st Annual Scientific Meeting - SIR 2006*, March 2006.

[99] G. S. Fischer, C. M. Wamsley, S. J. Zinreich, and G. Fichtinger, "Laser-assisted mri-guided needle insertion and comparison of techniques," *International Society for Computer Assisted Orthopaedic Surgery 6th Annual Conference - CAOS 2006*, pp. 161–163, June 2006.

[100] H. Liu, W. A. Hall, A. J. Martin, and C. L. Truwit, "Biopsy needle tip artifact in mr-guided neurosurgery." *J Magn Reson Imaging*, vol. 13, no. 1, pp. 16–22, Jan 2001.

[101] S. P. DiMaio, D. F. Kacher, R. E. Ellis, G. Fichtinger, N. Hata, G. P. Zientara, L. P. Panych, R. Kikinis, and F. A. Jolesz, "Needle artifact localization in 3t mr images." *Stud Health Technol Inform*, vol. 119, pp. 120–125, 2006.

[102] S. George and T. Kesavadas, "Low cost augmented reality for training of mri-guided needle biopsy of the spine." *Stud Health Technol Inform*, vol. 132, pp. 138–140, 2008.

[103] B. J. Wood, H. Zhang, A. Durrani, N. Glossop, S. Ranjan, D. Lindisch, E. Levy, F. Banovac, J. Borgert, S. Krueger, J. Kruecker, A. Viswanathan, and K. Cleary, "Navigation with electromagnetic tracking for interventional radiology procedures: a feasibility study." *J Vasc Interv Radiol*, vol. 16, no. 4, pp. 493–505, Apr 2005. [Online]. Available: http://dx.doi.org/10.1097/01.RVI.0000148827.62296.B4

[104] R. C. Susil, J. H. Anderson, and R. H. Taylor, "A single image registration method

for ct guided interventions," *Med Image Comput Comput Assist Interv Int Conf Med Image Comput Comput Assist Interv*, vol. 1679, pp. 798–808, September 1999.

[105] S. Lee, G. Fichtinger, and G. S. Chirikjian, "Numerical algorithms for spatial registration of line fiducials from cross-sectional images." *Med Phys*, vol. 29, no. 8, pp. 1881–1891, Aug 2002.

[106] M. P. Heilbrun, T. S. Roberts, M. L. Apuzzo, T. H. Wells, and J. K. Sabshin, "Preliminary experience with brown-roberts-wells (brw) computerized tomography stereotaxic guidance system." *J Neurosurg*, vol. 59, no. 2, pp. 217–222, Aug 1983.

[107] K. S. Arun, T. S. Huang, and S. D. Blostein, "Least-squares fitting of two 3-d point sets," *IEEE Transactions on Pattern Analysis and Machine Intelligence*, vol. 9, no. 5, pp. 698–700, September 1987.

[108] G. S. Fischer, "Electromagnetic tracker characterization and optimal tool design (with applications to ent surgery)," Master's thesis, Johns Hopkins University, 2005.

[109] H. C. Lin, I. Shafran, D. Yuh, and G. D. Hager, "Towards automatic skill evaluation: detection and segmentation of robot-assisted surgical motions." *Comput Aided Surg*, vol. 11, no. 5, pp. 220–230, Sep 2006. [Online]. Available: http://dx.doi.org/10.1080/10929080600989189

[110] S. J. Haker, R. V. Mulkern, J. R. Roebuck, A. S. Barnes, S. Dimaio, N. Hata, and

C. M. Tempany, "Magnetic resonance-guided prostate interventions." *Top Magn Reson Imaging*, vol. 16, no. 5, pp. 355–368, Oct 2005.

[111] A. S. Barnes, S. J. Haker, R. V. Mulkern, M. So, A. V. D'Amico, and C. M. Tempany, "Magnetic resonance spectroscopy-guided transperineal prostate biopsy and brachytherapy for recurrent prostate cancer." *Urology*, vol. 66, no. 6, p. 1319, Dec 2005. [Online]. Available: http://dx.doi.org/10.1016/j.urology.2005.06.105

[112] K. Wallner, J. Blasko, and M. Dattoli, *Prostate Brachytherapy Made Complicated, 2nd Ed.* SmartMedicine Press, 2001.

[113] J. Bellon, K. Wallner, W. Ellis, K. Russell, W. Cavanagh, and J. Blasko, "Use of pelvic ct scanning to evaluate pubic arch interference of transperineal prostate brachytherapy." *Int J Radiat Oncol Biol Phys*, vol. 43, no. 3, pp. 579–581, Feb 1999.

[114] J. G. Strang, D. J. Rubens, R. A. Brasacchio, Y. Yu, and E. M. Messing, "Real-time us versus ct determination of pubic arch interference for brachytherapy." *Radiology*, vol. 219, no. 2, pp. 387–393, May 2001.

[115] S. A. Tincher, R. Y. Kim, M. P. Ezekiel, T. Zinsli, J. B. Fiveash, D. A. Raben, A. J. Bueschen, and D. A. Urban, "Effects of pelvic rotation and needle angle on pubic arch interference during transperineal prostate implants." *Int J Radiat Oncol Biol Phys*, vol. 47, no. 2, pp. 361–363, May 2000.

[116] L. Fu, H. Liu, W. S. Ng, D. Rubens, J. Strang, E. Messing, and Y. Yu, "Hybrid

dosimetry: feasibility of mixing angulated and parallel needles in planning prostate brachytherapy." *Med Phys*, vol. 33, no. 5, pp. 1192–1198, May 2006.

[117] F. G. Shellock, "Magnetic resonance safety update 2002: implants and devices." *J Magn Reson Imaging*, vol. 16, no. 5, pp. 485–496, Nov 2002. [Online]. Available: http://dx.doi.org/10.1002/jmri.10196

[118] *Standard test method for measurement of magnetically induced displacement force on passive implants in the magnetic resonance environment, F2052*. American Society for Testing and Materials (ASTM), 2002, vol. 13.01.

[119] G. S. Fischer, A. Krieger, I. I. Iordachita, C. Csoma, L. L. Whitcomb, and G. Fichtinger, "Mri compatibility of robot actuation techniques – a comparative study," *Int Conf Med Image Comput Comput Assist Interv*, Sept. 2008.

[120] M. J. Firbank, A. Coulthard, R. M. Harrison, and E. D. Williams, "A comparison of two methods for measuring the signal to noise ratio on mr images." *Phys Med Biol*, vol. 44, no. 12, pp. N261–N264, Dec 1999.

[121] R. Gassert, N. Vanello, D. Chapuis, V. Hartwig, E. Scilingo, A. Bicchi, L. Landini, E. Burdet, and H. Bleuler, "Active mechatronic interface for haptic perception studies with functional magnetic resonance imaging: compatibility and design criteria," in *Proc. IEEE International Conference on Robotics and Automation ICRA 2006*, N. Vanello, Ed., 2006, pp. 3832–3837.

[122] L. Curiel, L. Curiel, R. Chopra, and K. Hynynen, "P2d-7 simultaneous us/mr imaging," in *Proc. IEEE Ultrasonics Symposium*, R. Chopra, Ed., 2006, pp. 1643–1646.

[123] G. Wan, Z. Wei, L. Gardi, D. B. Downey, and A. Fenster, "Brachytherapy needle deflection evaluation and correction." *Med Phys*, vol. 32, no. 4, pp. 902–909, Apr 2005.

[124] R. J. Webster III, J. Memisevic, and A. M. Okamura, "Design considerations for robotic needle steering," in *Proc. IEEE International Conference on Robotics and Automation ICRA 2005*, 2005, pp. 3588–3594.

[125] S. P. DiMaio and S. E. Salcudean, "Needle steering and motion planning in soft tissues," *IEEE J BME*, vol. 52, no. 6, pp. 965–974, June 2005.

[126] P. Schwamb and A. L. Merrill, *Elements of Mechanism*, 1905.

[127] S. Ning and G. Bone, "Experimental comparison of two pneumatic servo position control algorithms," in *Proc. IEEE International Conference Mechatronics and Automation*, G. Bone, Ed., vol. 1, 2005, pp. 37–42 Vol. 1.

[128] A. Kapoor, N. Simaan, and P. Kazanzides, "A system for speed and torque control of dc motors with application to small snake robots," in *Mechatronics and Robotics*, 2004.

[129] A. Kapoor, A. Deguet, and P. Kazanzides, "Software components and frameworks

for medical robot control," in *Proc. IEEE International Conference on Robotics and Automation ICRA 2006*, A. Deguet, Ed., 2006, pp. 3813–3818.

[130] A. Paul, J. Mishra, and M. Radke, "Reduced order sliding mode control for pneumatic actuator," vol. 2, no. 3, pp. 271–276, Sept. 1994.

[131] T. Acarman, C. Hatipoglu, and U. Ozguner, "A robust nonlinear controller design for a pneumatic actuator," in *Proc. American Control Conference the 2001*, vol. 6, 2001, pp. 4490–4495 vol.6.

[132] P. Korondi and J. Gyeviki, "Robust position control for a pneumatic cylinder," in *Proc. 12th International Power Electronics and Motion Control Conference EPE-PEMC 2006*, Aug. 2006, pp. 513–518.

[133] A. Koshkouei, K. Burnham, and A. Zinober, "Dynamic sliding mode control design," *IEE Proceedings -Control Theory and Applications*, vol. 152, no. 4, pp. 392–396, 8 July 2005.

[134] T. Nguyen, J. Leavitt, F. Jabbari, and J. Bobrow, "Accurate sliding-mode control of pneumatic systems using low-cost solenoid valves," vol. 12, no. 2, pp. 216–219, April 2007.

[135] G. Bone and S. Ning, "Experimental comparison of position tracking control algorithms for pneumatic cylinder actuators," vol. 12, no. 5, pp. 557–561, Oct. 2007.

[136] N. Hata, S. Piper, F. A. Jolesz, C. M. C. Tempany, P. M. Black, S. Morikawa,

H. Iseki, M. Hashizume, and R. Kikinis, "Application of open source image guided therapy software in mr-guided therapies." *Med Image Comput Comput Assist Interv Int Conf Med Image Comput Comput Assist Interv*, vol. 10, no. Pt 1, pp. 491–498, 2007.

[137] P. Mewes, J. Tokuda, S. P. DiMaio, G. S. Fischer, C. Csoma, D. G. Gobi, C. Tempany, G. Fichtinger, and N. Hata, "An integrated mri and robot control software system for an mr-compatible robot in prostate intervention," in *IEEE ICRA*, May 2008.

[138] J. V. Spiczak, E. Samset, S. Dimaio, G. Reitmayr, D. Schmalstieg, C. Burghart, and R. Kikinis, "Device connectivity for image-guided medical applications." *Stud Health Technol Inform*, vol. 125, pp. 482–484, 2007.

[139] J. Tokuda, G. S. Fischer, C. Csoma, S. P. DiMaio, D. G. Gobbi, G. Fichtinger, C. M. Tempany, and N. Hata, "Software strategy for robotic transperineal prostate therapy in closed-bore mri," *Int Conf Med Image Comput Comput Assist Interv*, Sept. 2008.

[140] S. P. DiMaio, E. Samset, G. S. Fischer, I. I. Iordachita, G. Fichtinger, F. Jolesz, and C. M. Tempany, "Dynamic mri scan plane control for passive tracking of instruments and devices." *Med Image Comput Comput Assist Interv Int Conf Med Image Comput Comput Assist Interv*, vol. 10, no. Pt 2, pp. 50–58, 2007.

[141] *Determination of Signal-to-Noise Ratio (SNR) in Diagnostic Magnetic Resonance*

Imaging, NEMA Standard Publication MS 1-2008. The Association of Electrical and Medical Imaging Equipment Manufacturers, 2008.

[142] J. Tokuda, S. P. DiMaio, G. S. Fischer, C. Csoma, D. Gobbi, G. Fichtinger, N. Hata, and C. M. Tempany, "Real-time mr imaging controlled by transperineal needle placement device for mri-guided prostate biopsy and brachytherapy," *Proc. of the 16th Meeting of the International Society for Magnetic Resonance in Medicine - ISMRM*, p. 3004, May 2008, http://www.ismrm.org/08/EP1.htm.

[143] A. K. Singh, A. Krieger, J. B. Lattouf, P. Guion, R. L. Grubb, P. S. Albert, G. Metzger, K. Ullman, S. Smith, G. Fichtinger, I. Ocak, P. Choyke, C. Menard, and J. Coleman, "Patient selection determines the prostate cancer yield of dynamic contrast-enhanced magnetic resonance imaging-guided transrectal biopsies in a closed 3-tesla scanner." *BJU Int*, vol. 101, no. 2, pp. 181–185, Jan 2008. [Online]. Available: http://dx.doi.org/10.1111/j.1464-410X.2007.07219.x

[144] S. Haker, A. Barnes, S. Maier, C. Tempany, and R. Mulkern, "Diffusion tensor imaging for prostate cancer detection: Preliminary results from a biopsy-based assessment," in *International Society for Magnetic Resonance in Medicine, 13th Scientific Meeting and Exhibition, Proceedings*, 2005.

[145] I. Chan, W. Wells, R. V. Mulkern, S. Haker, J. Zhang, K. H. Zou, S. E. Maier, and C. M. C. Tempany, "Detection of prostate cancer by integration of line-scan

diffusion, t2-mapping and t2-weighted magnetic resonance imaging; a multichannel statistical classifier." *Med Phys*, vol. 30, no. 9, pp. 2390–2398, Sep 2003.

[146] A. R. Padhani, C. J. Gapinski, D. A. Macvicar, C. J. Parker, J. Suckling, P. Revell, M. Leach, D. Dearnaley, and J. E. Husband, "Dynamic contrast enhanced mri of prostate cancer: correlation with morphology and tumour stage, histological grade and psa." in *Clin Radiol.*, vol. 55, 2000, pp. 99–109.

[147] K. K. Yu and H. Hricak, "Imaging prostate cancer." *Radiol Clin North Am*, vol. 38, no. 1, pp. 59–85, viii, Jan 2000.

Vita

Gregory S. Fischer was born on July 16, 1980 in New Brunswick, New Jersey, and raised in Warren, New Jersey. After graduating from Watchung Hills Regional High School (WHRHS) in 1998, Greg went on to earn B.S. degrees in electrical engineering and mechanical engineering from Rensselaer Polytechnic Institute (RPI), Troy, NY, in 2002. Since 2002, Greg has been a graduate research assistant with the The Johns Hopkins University Center for Computer Integrated Surgery (ERC CISST). In the pursuit of his Ph.D., Greg has earned M.S.E. degrees in electrical engineering and mechanical engineering from The Johns Hopkins University, Baltimore, MD, in 2004 and 2005, respectively. His research interests include development of interventional robotic systems, robot mechanism design, pneumatic control systems, surgical device instrumentation and MRI-compatible robotic systems.

Education

Johns Hopkins University - Baltimore, MD

Ph.D., Mechanical Engineering (June 2008)

Doctoral Thesis: Enabling Technologies for MRI Guided Interventional Procedures (With Applications to Prostate Cancer Diagnosis and Therapy)

Advisor : Gabor Fichtinger

Thesis Committee members : Allison M. Okamura and Russell H. Taylor

Johns Hopkins University - Baltimore, MD

M.S.E., Mechanical Engineering (May 2005)

Master's Thesis: Electromagnetic Tracker Calibration and Optimal Tool Design (With Applications to ENT Surgery)

Advisor : Russell H. Taylor

Industry Collaborator : Northern Digital, Inc.

Johns Hopkins University - Baltimore, MD

M.S.E., Electrical Engineering (May 2003)

Rensselaer Polytechnic Institute - Troy, NY

B.S., Mechanical Engineering (May 2002)

Rensselaer Polytechnic Institute - Troy, NY

B.S., Electrical Engineering (May 2002)

Publications

Refereed Journal Publications

1. Fischer GS, Iordachita I, Csoma C, Tokuda J, DiMaio SP, Tempany CM, Hata N, Fichtinger G, MRI-Compatible Pneumatic Robot for Transperineal Prostate Needle Placement, IEEE / ASME Transactions on Mechatronics - Focused section on MRI Compatible Mechatronic Systems, Vol 13, No 3, pp 295-305, June 2008

2. Fischer GS , Deguet A, Csoma C, Taylor RH, Fayad LM, Carrino JA, Zinreich SJ, Fichtinger G, MRI Image Overlay: Application to Arthrography Needle Insertion, Journal of Computer Assisted Surgery - JCAS, Vol 12, No 1, pp 2-14, January 2007

3. Fichtinger G, Deguet A, Masamune K, Fischer GS, Balogh E, Mathieu H, Taylor RH, Zinreich SJ, Fayad LM, Image Overlay Guidance for Needle Insertion in CT Scanner, IEEE Transactions on Biomedical Engineering, Vol 52, No 8, pp 1415-1424, August 2005

4. Fichtinger G, Deguet A, Fischer GS, Balogh E, Masamune K, Taylor RH, Fayad LM, Zinreich SJ, CT Image Overlay for Percutaneous Needle Insertions, Journal of Computer Assisted Surgery - JCAS, Vol 10, No 4, pp 241-255, July 2005

Refereed Conference Proceedings

1. Fischer GS, Krieger A, Iordachita I, Csoma C, Whitcomb L, Fichtinger G, MRI Compatibility of Robot Actuation Techniques A Comparative Study, 11th International Conference on Medical Image Computing and Computer-Assisted Intervention - MICCAI 2008, New York, NY, Lecture Notes on Computer Science, September 2008.

2. Tokuda J, Fischer GS, Csoma C, DiMaio SP, Gobbi DG, Fichtinger G, Tempany C, Hata N, Software Strategy for Robotic Transperineal Prostate Therapy in Closed-Bore MRI, 11th International Conference on Medical Image Computing and Computer-Assisted Intervention - MICCAI 2008, New York, NY, Lecture Notes on Computer Science, September 2008.

3. Fischer GS, Iordachita I, Csoma C, Tokuda J, Mewes PW, Tempany CM, Hata N, Fichtinger G, Pneumatically Operated MRI-Compatible Needle Placement Robot for Prostate Interventions, International Conference on Robotics and Automation - ICRA 2008, Pasadena, CA, pp 2489-2495, May 2008

4. Mewes PW, Tokuda J, DiMaio SP, Fischer GS, Csoma C, Gobbi DG, Tempany CM, Fichtinger G, Hata N, An Integrated MRI and Robot Control Software for an MRI-compatible Robot in Prostate Intervention, International Conference on Robotics and Automation - ICRA 2008, Pasadena, CA, pp 2950-2962, May 2008

5. Fischer GS, Iordachita I, DiMaio SP, Fichtinger G, Development of a Robotic As-

sistant for Needle-Based Transperineal Prostate Interventions in MRI, 10th International Conference on Medical Image Computing and Computer-Assisted Intervention - MICCAI 2007, Brisbane, Australia, Lecture Notes on Computer Science, Vol 4791, pp 425-433, Springer, November 2007

6. DiMaio S, Samset E, Fischer GS, Iordachita I, Fichtinger G, Jolesz F, Tempany C, Dynamic MRI Scan Plane Control for Passive Tracking of Instruments and Devices, 10th International Conference on Medical Image Computing and Computer-Assisted Intervention - MICCAI 2007, Brisbane, Australia, Lecture Notes on Computer Science, Vol 4792, pp 50-58, Springer, November 2007

7. Fischer GS, Iordachita I, DiMaio SP, Fichtinger G, Design of a Robot for Transperineal Prostate Needle Placement in an MRI Scanner, IEEE International Conference on Mechatronics - ICM 2006, Budapest, Hungary, July 2006

8. Fischer GS, Deguet A, Csoma C, Taylor RH, Fayad L, Zinreich SJ, and Fichtinger G, Musculoskeletal Needle Placement with MRI Image Overlay Guidance, International Society for Computer Assisted Orthopaedic Surgery 6th Annual Conference - CAOS 2006, Montreal, Canada, pp 158-160, June 2006

9. Fischer GS, Wamsley C, Zinreich SJ, and Fichtinger G, Laser-Assisted MRI-Guided Needle Insertion and Comparison of Techniques, International Society for Computer Assisted Orthopaedic Surgery 6th Annual Conference - CAOS 2006, Montreal, Canada, pp 161-163, June 2006

10. DiMaio SP, Fischer GS, Haker SJ, Hata N, Iordachita I, Tempany CM, Fichtinger G, System for MRI-guided Prostate Interventions, IEEE International Conference on Biomedical Robotics and Biomechatronics - BioRob 2006, Pisa, Italy, February 2006

11. Fischer GS, Akinbiyi T, Saha S, Zand J, Talamini M, Marohn M, Taylor RH, Ischemia and Force Sensing Surgical Instruments for Augmenting Available Surgeon Information, IEEE International Conference on Biomedical Robotics and Biomechatronics - BioRob 2006, Pisa, Italy, February 2006

12. Fischer GS, Taylor RH, Electromagnetic Tracker Measurement Error Simulation and Tool Design, Eighth International Conference on Medical Image Computing and Computer-Assisted Intervention - MICCAI 2005, Palm Springs, California, Lecture Notes on Computer Science, Vol 3750, pp 73-80, October 2005

13. Fischer GS, Zand JM, Talamini MA, Marohn M, Akinbiyi T, Kanev K, Kuo J, Kazanzides P, Taylor RH, Intra-operative Ischemia Sensing Surgical Instruments, International Conference on Complex Medical Engineering - CME 2005, Takamatsu, Japan, May 2005

14. Fichtinger G, Deguet A, Masamune K, Fischer GS, Balogh E, Mathieu H, Taylor RH, Fayad LM, SJ Zinreich, Needle Insertion in CT Scanner with Image Overlay - Cadaver Studies, Seventh International Conference on Medical Image Computing and Computer-Assisted Intervention - MICCAI 2004, St Malo, France, Lecture Notes on Computer Science, Vol 3217, pp 795-783, October 2004

15. Boctor E, Fischer GS, Choti M, Fichtinger G, Taylor RH, A Dual-Armed Robotic System for Intraoperative Ultrasound Guided Hepatic Ablative Therapy, International Conference on Robotics and Automation - ICRA 2004, New Orleans, LA, pp 2517-2522, April 2004

16. Prasad S, Kitagawa M, Fischer GS, Zand JM, Talamini MA, Taylor RH, Okamura A, A Modular 2-DOF Force-Sensing Instrument For Laparoscopic Surgery, Sixth International Conference on Medical Image Computing and Computer-Assisted Intervention - MICCAI 2003, Montreal, Canada, Lecture Notes on Computer Science, Vol 2878, pp 279-286, November 2003

Conference Abstracts and Non Peer-Reviewed Papers

1. Tokuda J, DiMaio SP, Fischer GS, Csoma C, Gobbi D, Fichtinger G, Hata N, Tempany CM, Real-time MR Imaging Controlled by Transperineal Needle Placement Device for MRI-guided Prostate Biopsy, International Society for Magnetic Resonance in Medicine 16th Scientific Meeting - ISMRM 2006, Berlin, Germany, May 2008

2. Fischer GS, Weiss CR, Dyer E, Csoma C, Deguet A, Carrino JA, Fichtinger G, Evaluation of MR Image Overlay for Spinal Interventions, International Society for Magnetic Resonance in Medicine 15th Scientific Meeting - ISMRM 2006, Berlin, Germany, May 2007

3. Fischer GS, Dyer E, Csoma C, Deguet A, Fichtinger G, Validation System of MRI Image Overlay and Other Insertion Techniques, Studies in Health Technology and Informatics - Medicine Meets Virtual Reality 15: In vivo, In vitro, In silico: Designing the Next in Medicine, Vol 125, pp 130-135, February 2007

4. Fischer GS, DiMaio SP, Iordachita I, Fichtinger G, Robotic Assistant for MR-guided Prostate Biopsy, 6th Interventional MRI Symposium, Leipzig, Germany, September 2006

5. Fischer GS, Deguet A, Csoma C, Taylor RH, Fayad LM, Carrino JA, Zinreich SJ, Fichtinger G, Image Overlay for MR-Guided Joint Arthrography, 6th Interventional MRI Symposium, Leipzig, Germany, pp 240-242, September 2006

6. Fischer GS, Deguet A, Csoma C, Taylor RH, Fayad L, Zinreich SJ, and Fichtinger G, MRI Image Overlay: Joint Arthrography Porcine Trials, International Society for Magnetic Resonance in Medicine 14th Scientific Meeting - ISMRM 2006, Seattle, Washington, p 1735, May 2006

7. Fischer GS, Wamsley C, Zinreich SJ, and Fichtinger G, MRI Guided Needle Insertion - Comparison of Four Techniques, Society for Interventional Radiology 31st Annual Scientific Meeting - SIR 2006, Toronto, Canada, March 2006

8. Fischer GS, Deguet A, Schlattman D, Taylor RH, Fayad L, Zinreich SJ, Fichtinger G, MRI Image Overlay: Applications to Arthrography Needle Insertion, Studies in

health technology and informatics - Medicine Meets Virtual Reality 14: Accelerating Change in Healthcare: Next Medical Toolkit, Vol 119, pp 150-155, February 2006

9. Fischer GS, Saha S, Horwat J, Yu J, Zand J, Marohn M, Talamini MA, Taylor RH, An Intra-Operative System for Relating Ischemic Damage to Retraction Forces, Annual fall meeting of the Biomedical Engineering Society - BMES 2005, Baltimore, MD, September 2005

10. Zand JM, Fischer GS, Hanly E, Shih S, Marohn M, Taylor RH, Talamini MA, Ischemia Sensing Surgical Instruments, Annual congress of the Society of American Gastrointestinal Endoscopic Surgeons - SAGES 2005, Ft. Lauderdale, FL, April 2005

11. DeOliviera M, Deguet A, Fischer GS, Balogh E, Taylor RH, Fayad LM, Zinreich SJ, Fichtinger G, Image Overlay for CT-Guided Hepatic Needle Insertions - Cadaver Studies, Congress of the Society of American Gastrointestinal Endoscopic Surgeons - SAGES 2005, Ft. Lauderdale, FL, April 2005